

Semilocal momentum-space regularized chiral two-nucleon potentials up to fifth order

P. Reinert^a, H. Krebs^b, and E. Epelbaum^c

Institut für Theoretische Physik II, Ruhr-Universität Bochum, D-44780 Bochum, Germany

Received: 27 December 2017 / Revised: 30 March 2018

Published online: 28 May 2018

© Società Italiana di Fisica / Springer-Verlag GmbH Germany, part of Springer Nature, 2018

Communicated by T. Duguet

Abstract. We introduce new semilocal two-nucleon potentials up to fifth order in the chiral expansion. We employ a simple regularization approach for the pion exchange contributions which i) maintains the long-range part of the interaction, ii) is implemented in momentum space and iii) can be straightforwardly applied to regularize many-body forces and current operators. We discuss in detail the two-nucleon contact interactions at fourth order and demonstrate that three terms out of fifteen used in previous calculations can be eliminated via suitably chosen unitary transformations. The removal of the redundant contact terms results in a drastic simplification of the fits to scattering data and leads to interactions which are much softer (*i.e.*, more perturbative) than our recent semilocal coordinate-space regularized potentials. Using the pion-nucleon low-energy constants from matching pion-nucleon Roy-Steiner equations to chiral perturbation theory, we perform a comprehensive analysis of nucleon-nucleon scattering and the deuteron properties up to fifth chiral order and study the impact of the leading F-wave two-nucleon contact interactions which appear at sixth order. The resulting chiral potentials at fifth order lead to an outstanding description of the proton-proton and neutron-proton scattering data from the self-consistent Granada-2013 database below the pion production threshold, which is significantly better than for any other chiral potential. For the first time, the chiral potentials match in precision and even outperform the available high-precision phenomenological potentials, while the number of adjustable parameters is, at the same time, reduced by about $\sim 40\%$. Last but not least, we perform a detailed error analysis and, in particular, quantify for the first time the statistical uncertainties of the fourth- and the considered sixth-order contact interactions.

1 Introduction

In recent years, considerable progress has been made towards developing accurate and precise nuclear forces in the framework of chiral effective field theory (EFT), see refs. [1, 2] for review articles and ref. [3] for a pedagogical introduction. In particular, the chiral expansion of the two-nucleon force was pushed to fifth order (N^4LO) [4] using the heavy-baryon formulation with pions and nucleons as the only explicit degrees of freedom in the effective Lagrangian. Even the dominant sixth-order (N^5LO) contributions have been worked out in ref. [5]. In parallel with these developments, a new generation of chiral nucleon-nucleon (NN) potentials up to N^4LO was introduced by the Bochum-Bonn [6, 7] and Idaho-Salamanca [8] groups, see also refs. [9–12] for related recent studies along similar lines. One important difference between these potentials concerns the implementation of the regulator(s).

It was argued in ref. [6] that the usage of a local regularization for the pion exchange contributions allows one to significantly reduce the amount of finite-cutoff artefacts. In [6, 7], the one-pion exchange (OPEP) and two-pion exchange potentials (TPEP) were regularized in coordinate space via

$$V_\pi(\vec{r}) \longrightarrow V_{\pi,R}(\vec{r}) = V_\pi(\vec{r}) [1 - \exp(-r^2/R^2)]^n, \quad (1)$$

where the cutoff R was chosen in the range of $R = 0.8 \dots 1.2$ fm in line with the estimation of the breakdown distance of the chiral expansion of ref. [13]. For the earlier applications of a similar regularization scheme in the context of nuclear chiral EFT see refs. [14, 15]. The exponent n was set $n = 6$, but choosing $n = 5$ or $n = 7$ was shown in ref. [6] to lead to a comparable description of the phase shifts. For the contact interactions, a simple Gaussian momentum-space regulator $\exp(-(p^2 + p'^2)/\Lambda^2)$ with the cutoff $\Lambda = 2R^{-1}$ was used. Here and in what follows, \vec{p}' and \vec{p} denote the final and initial momenta of the nucleons in the center of mass system. On the other hand, Entem *et al.* employ in their recent study [8] the

^a e-mail: patrick.reinert@rub.de

^b e-mail: hermann.krebs@rub.de

^c e-mail: evgeny.epelbaum@rub.de

same nonlocal momentum-space regulator as used in the first-generation chiral fourth-order (N^3LO) potentials of refs. [16, 17], namely

$$\begin{aligned} V(\vec{p}', \vec{p}) &\longrightarrow V_\Lambda(\vec{p}', \vec{p}) = \\ &V(\vec{p}', \vec{p}) \exp [-(p'/\Lambda)^{2n} - (p/\Lambda)^{2n}], \end{aligned} \quad (2)$$

for both the long- and short-range contributions. The exponent n is chosen in such a way that the induced contributions to the potential resulting from the Taylor expansion of the regulator function appear beyond the considered chiral order (assuming that the cutoff Λ is chosen of the order of the breakdown scale Λ_b of the chiral expansion). Clearly, being angle-independent, the momentum-space regulator in eq. (2) acts in the same multiplicative way in all partial waves and, therefore, unavoidably leads to distortions of phase shifts in channels with arbitrarily high values of the angular momentum. This indicates that it affects the long-range part of the interaction. The induced artefacts are expected to be beyond the accuracy of the calculation as long as the cutoff Λ is chosen sufficiently large, but they may become an issue if it is lowered below the breakdown scale Λ_b . In contrast, the local regulator in eq. (1) does not affect the long-range interaction as long as $R \lesssim \Lambda_b^{-1}$, and the corresponding distortions in peripheral NN scattering decrease with increasing values of the angular momentum (for the case of non-singular potentials). It is also worth mentioning that the nonlocal regulator in eq. (2) does not completely remove unphysical short-distance components of the chiral TPEP so that an additional spectral function regularization had to be employed in ref. [8] along the lines of refs. [18, 19].

The semilocal coordinate-space regularized (SCS) chiral potentials by Epelbaum, Krebs, Meißner (EKM) developed in refs. [6, 7] are available for five cutoff values of $R = 0.8, 0.9, 1.0, 1.1$ and 1.2 fm and were found to provide a very good description of the phase shifts and mixing angles of the Nijmegen partial wave analysis (NPWA) [20] used to fix the low-energy constants (LECs) accompanying the NN contact interactions. In addition, the significant reduction in the χ^2 per datum for the description of the Nijmegen neutron-proton (np) and proton-proton (pp) phase shifts when going from the second chiral order (NLO) to the third one (N^2LO) [6] and from N^3LO to N^4LO [7] provides a clear evidence of the chiral TPEP, which is completely determined by the spontaneously broken chiral symmetry of QCD and the experimental/empirical information on the pion-nucleon (πN) system. In combination with the algorithm for quantification of truncation errors formulated in ref. [6], that exploits the available information on the chiral expansion for an observable of interest to estimate the size of neglected higher-order terms without relying on cutoff variation (see refs. [21–24] for examples of similar approaches to error estimation), the EKM NN potentials were found to yield promising results for nucleon-deuteron scattering and the properties of light nuclei [25, 26], selected electroweak processes involving two- and three-nucleon systems [27, 28] and nuclear matter properties [29], see also ref. [30] for a recent application to derive an optical potential for describing

elastic proton-nucleus scattering. These calculations are based solely on the two-nucleon potentials and do not provide a complete treatment of the current operators, so that the next step is clearly to include the corresponding three-nucleon forces [31–36] and exchange current operators [37–39]¹. This is, in fact, the main goal of the recently formed LENPIC Collaboration, see ref. [43] for an overview of the range of activities within LENPIC.

While the novel EKM NN potentials lead to very promising results in all applications considered so far, there is still room for improvement. First, the contact interactions of the EKM potentials were determined from fits to the NPWA rather than to the scattering data which may introduce some model dependence. This also prevents one from making a direct comparison with other chiral and phenomenological potentials fitted to the scattering data in terms of precision. Secondly, truncation errors estimated in refs. [6, 7] represent only one source of uncertainties in the calculations. While they can be assumed to dominate the theoretical error, see the discussion in ref. [6], it is important to quantify and propagate the statistical uncertainties of the LECs accompanying the NN contact interactions, see ref. [44] for a related study at N^2LO , and to address other sources of uncertainties including the ones associated with the pion-nucleon LECs and with the choice of energy range used in the determination of the NN contact interactions. However, the most pressing issue for the applications of the EKM potentials beyond the two-nucleon system is the implementation of a consistent local regularization for many-body forces and current operators. Here, the main technical obstacle is the need to perform the regularization in coordinate space. Given the rather complicated expressions for certain kinds of contributions to the three-nucleon force (3NF) at N^3LO and beyond and the dependence of the 3NF on two relative distances, a direct approach by (numerically) performing the Fourier transforms to coordinate space and, after regularization, back to momentum space appears to be challenging. Alternatively, regularization can also be carried out directly in terms of the momentum-space matrix elements in the partial wave basis, which can be obtained for arbitrary 3NF momentum-space expressions using the methods of refs. [45, 46], but this approach requires additional work to achieve numerically stable results [47]. Similar problems occur for the nuclear current operators, where, in addition, one needs to pay special attention to maintain the corresponding symmetries upon introducing the regulator.

The purpose of this paper is to address the issues mentioned above and, in particular, to remedy the situation with the (technically) complicated implementation of the regulator in coordinate space. To this aim, we introduce a simple local regularization scheme in momentum

¹ Notice that the vector and (some parts of the) axial current operators at fourth order in the chiral expansion have also been worked out by the JLab-Pisa group using time-ordered perturbation theory [40–42]. Their results disagree with ours for certain classes of contributions and correspond to a different choice of unitary transformations in the Fock space.

space by an appropriate modification of the propagators of pions exchanged between different nucleons. Our approach shares some similarities with the higher-derivative regularization scheme [48–51] carried out at the Lagrangian level and is well suited for applications to many-body forces and electroweak processes. Moreover, it does not require a recalculation of the TPEP NN potential as it can be formulated in terms of a particular form of the spectral function regularization. The important feature of the regulator is that it does, per construction, not affect the left-hand singularities in the potential due to single or multi-pion exchange *at any finite order in $1/\Lambda$ -expansion*, which is quite different from the regulator in eq. (2). As we will demonstrate, this feature has important phenomenological implications, especially for soft choices of Λ . Notice that while a residual Λ -dependence of observables calculated in chiral EFT is expected to go beyond the accuracy of the calculation provided $\Lambda \sim \Lambda_b$, one is usually restricted to rather soft values of Λ in order to avoid the appearance of spurious deeply bound states which would provide a severe complication for applications beyond the NN system. Under such circumstances, the reduction of finite- Λ artefacts does become an important issue. We also emphasize ongoing efforts towards developing completely regulator independent versions of chiral EFT with non-perturbative treatment of the one-pion exchange potential (at least) in low partial waves. These include formulations within the conventional non-relativistic framework based on the Schrödinger or Lippmann-Schwinger equations as suggested in *e.g.* [52–54], see, however, ref. [55] for a criticism of such approaches when applied to spin-triplet channels of NN scattering, and a formulation proposed in ref. [56] and leading to scattering equations such as *e.g.* the Kadyshevsky equation [57], which satisfy relativistic elastic unitarity and are renormalizable for the leading-order potential, see refs. [58–60] for recent applications.

Another important insight into the construction of nuclear forces from our analysis concerns the contact interactions at and beyond N³LO. When performing fits to NN scattering data, we found the convergence towards a minimum of the χ^2 in the parameter space to be very poor starting from N³LO. This unpleasant feature is found to be related to the appearance of three redundant contact operators in the set of fifteen N³LO contact terms used in [6–8, 16, 17], see ref. [61] for a similar conclusion². This redundancy was mentioned earlier, in particular in the context of pionless EFT [62, 63]. Here, we explicitly construct the corresponding short-range unitary transformations which can be used to eliminate the redundant terms from the potential, see also ref. [64] for similar considerations. We demonstrate upon performing explicit calculations that the redundancy of the contact interactions remains intact in the non-perturbative regime as relevant for the case at hand. The elimination of this redundancy turns out to be crucial for obtaining stable and physically meaningful results for the NN LECs when performing fits to scattering data.

² We are grateful to Dick Furnstahl for drawing our attention to a possible over-fitting issue in the NN S-waves.

Building upon these two approaches, we develop in this paper a new family of semilocal momentum-space regularized (SMS) chiral potentials up to fifth order in the chiral expansion and perform a comprehensive partial wave analysis of the neutron-proton and proton-proton scattering data including uncertainty quantification. Our paper is organized as follows. In sect. 2, we demonstrate the redundancy of three out of fifteen fourth-order contact interactions. The impact of their removal on the softness of the potentials is discussed in sect. 3. Section 4 is devoted to the description of our new regularization approach for pion exchange contributions. Our treatment of the long-range electromagnetic interactions is detailed in sect. 5, followed by the description of the fitting procedure in sect. 6. In sect. 7, we present the results for phase shifts, deuteron properties and the effective range parameters based on the new family of semilocal momentum-space regularized chiral potentials. This section also includes a comprehensive error analysis for all considered observables. Next, in sect. 8, we discuss an alternative choice of the order-four contact interactions. A comparison of our new potentials at the highest considered chiral order with the modern high-precision phenomenological and nonlocal chiral EFT potentials is presented in sect. 9, while the main results of our work are summarized in sect. 10. The appendices provide further details on the treatment of the short-range part of the interaction and calculation of scattering observables and show the neutron-proton and proton-proton phase shifts and mixing angles as obtained from our analysis.

2 Redundant contact interactions at fourth order

Up to and including fourth order in the chiral expansion, the short-range potential in the center-of-mass system (cms) in the limit of exact isospin symmetry takes the form

$$V_{\text{cont}} = V_{\text{cont}}^{(0)} + V_{\text{cont}}^{(2)} + V_{\text{cont}}^{(4)},$$

where the individual terms at orders Q^0 , Q^2 and Q^4 , with $Q \in \{p/\Lambda_b, M_\pi/\Lambda_b\}$ being the chiral expansion parameter, can be chosen as

$$\begin{aligned} V_{\text{cont}}^{(0)} &= C_S + C_T \vec{\sigma}_1 \cdot \vec{\sigma}_2, \\ V_{\text{cont}}^{(2)} &= C_1 q^2 + C_2 k^2 + (C_3 q^2 + C_4 k^2)(\vec{\sigma}_1 \cdot \vec{\sigma}_2) \\ &\quad + \frac{i}{2} C_5 (\vec{\sigma}_1 + \vec{\sigma}_2) \cdot (\vec{k} \times \vec{q}) + C_6 (\vec{q} \cdot \vec{\sigma}_1)(\vec{q} \cdot \vec{\sigma}_2) \\ &\quad + C_7 (\vec{k} \cdot \vec{\sigma}_1)(\vec{k} \cdot \vec{\sigma}_2), \\ V_{\text{cont}}^{(4)} &= D_1 q^4 + D_2 k^4 + D_3 q^2 k^2 + D_4 (\vec{q} \times \vec{k})^2 \\ &\quad + (D_5 q^4 + D_6 k^4 + D_7 q^2 k^2 + D_8 (\vec{q} \times \vec{k})^2)(\vec{\sigma}_1 \cdot \vec{\sigma}_2) \\ &\quad + \frac{i}{2} (D_9 q^2 + D_{10} k^2)(\vec{\sigma}_1 + \vec{\sigma}_2) \cdot (\vec{k} \times \vec{q}) \\ &\quad + (D_{11} q^2 + D_{12} k^2)(\vec{\sigma}_1 \cdot \vec{q})(\vec{\sigma}_2 \cdot \vec{q}) \\ &\quad + (D_{13} q^2 + D_{14} k^2)(\vec{\sigma}_1 \cdot \vec{k})(\vec{\sigma}_2 \cdot \vec{k}) \\ &\quad + D_{15} \vec{\sigma}_1 \cdot (\vec{q} \times \vec{k}) \vec{\sigma}_2 \cdot (\vec{q} \times \vec{k}), \end{aligned} \tag{3}$$

see *e.g.* ref. [16] and references therein. Here, \vec{q} denotes the momentum transfer of the nucleon $\vec{q} = \vec{p}' - \vec{p}$ with \vec{p} and \vec{p}' being the initial and final nucleon momenta in the cms, Further, $\vec{k} = (\vec{p}' + \vec{p})/2$ is the average nucleon momentum, $\vec{\sigma}_i$ are the Pauli spin matrices of the nucleon i while C_S , C_T , $C_{1,\dots,7}$ and $D_{1,\dots,15}$ refer to the corresponding LECs. Here and in what follows, we use the notation $q \equiv |\vec{q}|$, $k \equiv |\vec{k}|$. Our treatment of isospin-breaking (IB) effects is the same as in refs. [6, 7], and we refer the reader to these papers for the explicit form of included IB contact terms. Finally, all momentum-space expressions for the potentials throughout this paper are to be understood as matrix elements with respect to momenta.

The choice of the operator basis to represent V_{cont} given above is ambiguous. In particular, terms involving the isospin matrices are not listed as they do not provide additional information by virtue of the Pauli principle. Alternatively, quasi-local operator bases involving isospin matrices are employed in refs. [9, 11, 14, 15]. When expressed in the partial wave basis, the contact interactions have the form

$$\begin{aligned} \langle i_S, p' | V_{\text{cont}} | i_S, p \rangle &= \tilde{C}_{i_S} + C_{i_S}(p^2 + p'^2) + D_{i_S}^1 p^2 p'^2 \\ &\quad + D_{i_S}^2(p^4 + p'^4), \\ \langle i_P, p' | V_{\text{cont}} | i_P, p \rangle &= C_{i_P} p p' + D_{i_P} p p'(p^2 + p'^2), \\ \langle i_D, p' | V_{\text{cont}} | i_D, p \rangle &= D_{i_D} p^2 p'^2, \\ \langle {}^3S_1, p' | V_{\text{cont}} | {}^3D_1, p \rangle &= C_{\epsilon_1} p^2 + D_{\epsilon_1}^1 p^2 p'^2 + D_{\epsilon_1}^2 p^4, \\ \langle {}^3P_2, p' | V_{\text{cont}} | {}^3F_2, p \rangle &= D_{\epsilon_2} p^3 p', \end{aligned} \quad (4)$$

where $i_S = \{1S0, 3S1\}$, $i_P = \{1P1, 3P0, 3P1, 3P2\}$ and $i_D = \{1D2, 3D1, 3D2, 3D3\}$. The 24 LECs $\{\tilde{C}_{i_S}\}$, $\{C_{i_S}, C_{i_P}, C_{\epsilon_1}\}$ and $\{D_{i_S}^j, D_{i_P}, D_{i_D}, D_{\epsilon_1}^j, D_{\epsilon_2}\}$ with $j = 1, 2$ are given by linear combinations of the LECs C_S , C_T , $C_{1,\dots,7}$ and $D_{1,\dots,15}$ in eq. (3), whose explicit form can be found *e.g.* in ref. [16].

Obviously, the $D_{i_S}^1$ - and $D_{i_S}^2$ -terms as well as the $D_{\epsilon_1}^1$ - and $D_{\epsilon_1}^2$ -terms become indistinguishable on the energy shell, *i.e.* for $p' = p$, and the corresponding LECs cannot be disentangled from each other if treated perturbatively. The appearance of linear combinations formed out of the LECs in the 1S_0 , 3S_1 and ϵ_1 channels that vanish on the energy shell suggests that some of these terms are redundant. We now show that this is indeed the case and demonstrate explicitly that such redundant terms can be eliminated via suitably chosen unitary transformations.

Consider unitary transformations (UTs) acting on the purely nucleonic subspace of the pion-nucleon Fock space. When deriving the nuclear forces and current operators using the method of unitary transformation [65, 66] we, in fact, have to employ a broad class of such transformations constructed out of the vertices from the effective pion-nucleon Hamiltonian and the corresponding energy denominators in order to ensure renormalizability of the resulting nuclear potentials, see refs. [34, 36, 39, 67–69] for more details. We now consider all possible UTs whose generators are given by the order- Q^2 two-nucleon contact operators. Specifically, we have

$$U = e^{\gamma_1 T_1 + \gamma_2 T_2 + \gamma_3 T_3}, \quad (5)$$

where γ_i are transformation angles and the anti-Hermitian, Galilean-invariant generators T_i have the form

$$\begin{aligned} T_1 &= \frac{m_N}{8\Lambda_b^4}(p_1'^2 + p_2'^2 - p_1^2 - p_2^2) = \frac{m_N}{2\Lambda_b^4}\vec{k} \cdot \vec{q}, \\ T_2 &= \frac{m_N}{8\Lambda_b^4}(p_1'^2 + p_2'^2 - p_1^2 - p_2^2)\vec{\sigma}_1 \cdot \vec{\sigma}_2 = \frac{m_N}{2\Lambda_b^4}\vec{k} \cdot \vec{q}\vec{\sigma}_1 \cdot \vec{\sigma}_2, \\ T_3 &= \frac{m_N}{16\Lambda_b^4}\left(\vec{\sigma}_1 \cdot (\vec{p}_1 - \vec{p}_2 + \vec{p}_1' - \vec{p}_2')\vec{\sigma}_2\right. \\ &\quad \cdot (\vec{p}_1' - \vec{p}_2' - \vec{p}_1 + \vec{p}_2) + \vec{\sigma}_1 \cdot (\vec{p}_1' - \vec{p}_2' - \vec{p}_1 + \vec{p}_2)\vec{\sigma}_2 \\ &\quad \cdot (\vec{p}_1 - \vec{p}_2 + \vec{p}_1' - \vec{p}_2')\right) \\ &= \frac{m_N}{2\Lambda_b^4}\left(\vec{\sigma}_1 \cdot \vec{k}\vec{\sigma}_2 \cdot \vec{q} + \vec{\sigma}_1 \cdot \vec{q}\vec{\sigma}_2 \cdot \vec{k}\right), \end{aligned} \quad (6)$$

see also refs. [64, 70, 71] for a related discussion. The reason why such unitary transformations have escaped our consideration when deriving the nuclear forces and currents is that the generators T_i cannot be written in terms of the vertices entering the effective pion-nucleon Hamiltonian. Notice further that the first non-vanishing anti-Hermitian contact interactions appear at order Q^2 . Further, we do not consider the generators involving the isospin Pauli matrices for the reasons already mentioned. Finally, the factors of the nucleon mass m_N included in the definition of the generators ensure that the induced terms in the nuclear Hamiltonian appear at order Q^4 rather than Q^5 by virtue of the employed counting scheme for m_N [31], $m_N \sim \mathcal{O}(\Lambda_b^2/Q)$, while the factors of Λ_b^{-4} are required for dimensional reasons.

When applied to the LO nuclear Hamiltonian³, the UTs induce short-range interactions through

$$\begin{aligned} \delta \hat{H} &= \hat{U}^\dagger \hat{H}^{(0)} \hat{U} - \hat{H}^{(0)} = \sum_i \gamma_i [\hat{H}^{(0)}, \hat{T}_i] + \dots \\ &= \sum_i \gamma_i \left[(\hat{H}_{\text{kin}}^{(0)} + \hat{V}_{1\pi}^{(0)} + \hat{V}_{\text{cont}}^{(0)}), \hat{T}_i \right] + \dots, \end{aligned} \quad (7)$$

where ellipses refer to terms beyond the accuracy of our calculations and \hat{X} means that the quantity X is to be regarded as an operator rather than matrix element with respect to momenta of the nucleons. The commutator on the right-hand side gives rise to two- and three-nucleon operators. Consider first the induced two-nucleon terms. It is easy to see that the commutator $[(\hat{V}_{1\pi}^{(0)} + \hat{V}_{\text{cont}}^{(0)}), \hat{T}_i]$ generates, after evaluating the corresponding loop integrals, shifts to the order- Q^0 and Q^2 contact interactions and thus needs not to be considered explicitly. On the other hand, the commutator with the kinetic energy term generates the additional order- Q^4 contact interactions

$$\begin{aligned} \sum_i \gamma_i \langle \vec{p}_1' \vec{p}_2' | [\hat{H}_{\text{kin}}^{(0)}, \hat{T}_i] | \vec{p}_1 \vec{p}_2 \rangle &= \gamma_1 \frac{1}{\Lambda_b^4} (\vec{k} \cdot \vec{q})^2 \\ &\quad + \gamma_2 \frac{1}{\Lambda_b^4} (\vec{k} \cdot \vec{q})^2 \vec{\sigma}_1 \cdot \vec{\sigma}_2 + \gamma_3 \frac{1}{\Lambda_b^4} \vec{k} \cdot \vec{q} (\vec{\sigma}_1 \cdot \vec{k} \vec{\sigma}_2 \cdot \vec{q} \\ &\quad + \vec{\sigma}_1 \cdot \vec{q} \vec{\sigma}_2 \cdot \vec{k}). \end{aligned} \quad (8)$$

³ We do not need to consider here the contributions to the nuclear Hamiltonian at and beyond NLO since the resulting induced terms are beyond the accuracy of our calculations.

The γ_1 - and γ_2 -transformations induce the following shifts in the LECs D_i :

$$\delta D_3 = -\delta D_4 = \frac{\gamma_1}{\Lambda_b^4}, \quad \delta D_7 = -\delta D_8 = \frac{\gamma_2}{\Lambda_b^4}. \quad (9)$$

Using the identity

$$\vec{k} \cdot \vec{q} (\vec{\sigma}_1 \cdot \vec{k} \vec{\sigma}_2 \cdot \vec{q} + \vec{\sigma}_1 \cdot \vec{q} \vec{\sigma}_2 \cdot \vec{k}) = -(\vec{q} \times \vec{k})^2 \vec{\sigma}_1 \cdot \vec{\sigma}_2 + q^2 \vec{\sigma}_1 \cdot \vec{k} \vec{\sigma}_2 \cdot \vec{k} + k^2 \vec{\sigma}_1 \cdot \vec{q} \vec{\sigma}_2 \cdot \vec{q} + \vec{\sigma}_1 \cdot (\vec{q} \times \vec{k}) \vec{\sigma}_2 \cdot (\vec{q} \times \vec{k}), \quad (10)$$

one can read off the shifts in the LECs D_i induced by the γ_3 -transformation:

$$-\delta D_8 = \delta D_{12} = \delta D_{13} = \delta D_{15} = \frac{\gamma_3}{\Lambda_b^4}. \quad (11)$$

In the partial wave basis, the induced terms can obviously only affect off-the-energy-shell linear combinations of the order- Q^4 terms, *i.e.* the structures proportional to $p'^2 - p^2$. Introducing the corresponding linear combinations in the 1S_0 , 3S_1 and ϵ_1 channels *e.g.* via

$$\begin{aligned} D_{1S0}^1 p^2 p'^2 + D_{1S0}^2 (p^4 + p'^4) &=: D_{1S0} p^2 p'^2 \\ &\quad + D_{1S0}^{\text{off}} (p'^2 - p^2)^2, \\ D_{3S1}^1 p^2 p'^2 + D_{3S1}^2 (p^4 + p'^4) &=: D_{3S1} p^2 p'^2 \\ &\quad + D_{3S1}^{\text{off}} (p'^2 - p^2)^2, \\ D_{\epsilon 1}^1 p^2 p'^2 + D_{\epsilon 1}^2 p^4 &=: D_{\epsilon 1} p^2 p'^2 \\ &\quad + D_{\epsilon 1}^{\text{off}} p^2 (p'^2 - p^2), \end{aligned} \quad (12)$$

we adopt a *convention* by requiring the UTs to be chosen in such a way that

$$D_{1S0}^{\text{off}} = D_{3S1}^{\text{off}} = D_{\epsilon 1}^{\text{off}} = 0. \quad (13)$$

This corresponds to choosing the phases of the UTs as

$$\begin{aligned} \frac{\gamma_1}{\Lambda_b^4} &= -4D_1 - \frac{1}{4}D_2 - D_3, \\ \frac{\gamma_2}{\Lambda_b^4} &= -4D_5 - \frac{1}{4}D_6 - D_7, \\ \frac{\gamma_3}{\Lambda_b^4} &= -\frac{1}{8}(16D_{11} + 4D_{12} + 4D_{13} + D_{14}). \end{aligned} \quad (14)$$

For the sake of completeness, we give the form of the contact potential $V_{\text{cont}}^{(4)}$ after eliminating the redundant terms, subject to the adopted convention specified in

eqs. (12), (13), and after renaming the LECs,

$$\begin{aligned} V_{\text{cont}}^{(4)} &= D'_1 \left(q^4 - 4(\vec{k} \cdot \vec{q})^2 \right) + D'_2 \left(k^4 - \frac{1}{4}(\vec{k} \cdot \vec{q})^2 \right) \\ &\quad + D'_3 (\vec{q} \times \vec{k})^2 \\ &\quad + \left(D'_4 \left(q^4 - 4(\vec{k} \cdot \vec{q})^2 \right) + D'_5 \left(k^4 - \frac{1}{4}(\vec{k} \cdot \vec{q})^2 \right) \right. \\ &\quad \left. + D'_6 (\vec{q} \times \vec{k})^2 \right) \vec{\sigma}_1 \cdot \vec{\sigma}_2 + \frac{i}{2}(D'_7 q^2 + D'_8 k^2) \\ &\quad \times (\vec{\sigma}_1 + \vec{\sigma}_2) \cdot (\vec{k} \times \vec{q}) \\ &\quad + D'_9 \left(-\frac{1}{4}q^2 \vec{\sigma}_1 \cdot \vec{q} \vec{\sigma}_2 \cdot \vec{q} + 4k^2 \vec{\sigma}_1 \cdot \vec{k} \vec{\sigma}_2 \cdot \vec{k} \right) \\ &\quad + D'_{10} k^2 \left(\vec{\sigma}_1 \cdot \vec{q} \vec{\sigma}_2 \cdot \vec{q} - 4\vec{\sigma}_1 \cdot \vec{k} \vec{\sigma}_2 \cdot \vec{k} \right) \\ &\quad + D'_{11} (q^2 - 4k^2) \vec{\sigma}_1 \cdot \vec{k} \vec{\sigma}_2 \cdot \vec{k} \\ &\quad + D'_{12} \vec{\sigma}_1 \cdot (\vec{q} \times \vec{k}) \vec{\sigma}_2 \cdot (\vec{q} \times \vec{k}). \end{aligned} \quad (15)$$

The relations between 21 LECs $C_{S,T}$, $C_{1,\dots,7}$, $D'_{1,\dots,12}$ and the ones in the spectroscopic basis $\{\tilde{C}_{is}\}$, $\{C_{is}, C_{ip}, C_{\epsilon i}\}$ and $\{D_{is}, D_{ip}, D_{id}, D_{\epsilon 1}, D_{\epsilon 2}\}$ are provided in appendix A.

In addition to the two-nucleon potential, the commutator of $\hat{V}_{1\pi}^{(0)}$ and $\hat{V}_{\text{cont}}^{(0)}$ with the generators \hat{T}_i in eq. (7) gives rise to the induced three-nucleon forces. It is easy to see that the generated terms have the same form as the N⁴LO contributions to the one-pion exchange-contact and purely contact-type 3NFs, albeit with the numerical coefficients enhanced by one power of Q^{-1} due to the appearance of the factor of m_N/Λ_b . For example,

$$\langle \vec{p}'_1 \vec{p}'_2 \vec{p}'_3 | \left[(C_S + C_T \vec{\sigma}_1 \cdot \vec{\sigma}_2), \hat{T}_1 \right] | \vec{p}_1 \vec{p}_2 \vec{p}_3 \rangle = \frac{m_N}{4\Lambda_b^4} q_3^2 (C_S + C_T \vec{\sigma}_1 \cdot \vec{\sigma}_2), \quad (16)$$

where $q_3 \equiv |\vec{q}_3| = |\vec{p}_3' - \vec{p}_3|$. Given that the coupling constants of the corresponding short-range 3NFs are unknown and have to be determined from experimental data anyway, there is no need to explicitly keep track of the contributions induced by the considered UTs.

To summarize, the considered UTs affect the off-shell behavior of the two-nucleon force starting from N³LO at short distances and the strength of the short-range three-nucleon forces (and current operators), but have no effect on observable quantities. Their appearance is a manifestation of the redundancy of the basis of 15 contact interactions at N³LO used in all previous calculations at this and higher chiral orders [6–8, 16, 17]⁴. The impact of keeping/removing the redundant terms when performing the

⁴ In ref. [9], minimally nonlocal potentials involving TPEP with and without explicit $\Delta(1232)$ degrees of freedom up to N²LO, accompanied by short-range operators up to N³LO, were constructed. The short-range part of the potentials developed in that paper also involves 15 isospin-invariant operators at N³LO. More recently, fully local versions of these interactions have been constructed, which involve 11 isospin-invariant short-range operators at N³LO [11].

fits will be discussed in sect. 3. Finally, one should keep in mind that the convention of eq. (13) employed in the present work corresponds to one particular choice of the unitary transformations or, equivalently, off-shell behavior of the NN potential. There seems to be no obvious criterion for finding preferred choices other than that of the naturalness of the resulting LECs. In principle, one may think of exploiting the freedom in the choice of the UTs to *e.g.* enforce perturbativeness of the nuclear potentials in order to make them more suitable for many-body applications. In sect. 8 we will discuss an alternative choice of the basis of independent contact operators at order Q^4 which, however, will be shown to lead to less perturbative potentials.

We conclude this section by specifying the form of the leading contact interactions in F-waves whose impact will be discussed in the following sections. Such interactions contribute at sixth order in the chiral expansion, *i.e.* at N^5LO , and the corresponding partial wave matrix elements take the form

$$\langle i_F, p' | V_{\text{cont}} | i_F, p \rangle = E_{i_F} p^3 p'^3, \quad (17)$$

where $i_F = \{1F3, 3F2, 3F3, 3F4\}$ and E_{i_F} are the corresponding LECs.

3 Impact of removing redundant fourth-order contact interactions

We now discuss the impact of removing redundant contact interactions at order Q^4 for the already published EKM SCS potentials of ref. [7]. To this aim, we have constructed a version of the corresponding N^4LO potentials with the redundant contact interactions being removed according to the convention of eqs. (12), (13). The remaining LECs in the 1S_0 and ${}^3S_1-{}^3D_1$ channels are refitted to the Nijmegen PWA using the procedure of ref. [7]. While the χ^2 for the description of the Nijmegen phase shifts 1S_0 and 3S_1 and the mixing angle ϵ_1 does get considerably reduced upon including the redundant contact interactions, we do not observe any significant improvement in the description of scattering data. This indicates that the contributions of the redundant interactions likely go beyond the accuracy of our work in agreement with the discussion of sect. 2. In sect. 8, we will provide further numerical evidence to support this statement for the case of the SMS potentials.

We would also like to point out that the removal of the redundant contact interactions simplifies the data fitting procedure considerably. Including those interactions results in a very slow convergence of the fit once other terms have been adjusted properly and the parameters have entered the “valley” of the χ^2 surface formed by correlated values of the parameters, which result in almost equally good χ^2 values. The flatness of the χ^2 function poses a challenge to fitting algorithms, and it becomes extremely difficult to find a minimum irrespective of its statistical significance.

It is instructive to compare the partial wave momentum-space matrix elements of the N^4LO potential

with and without redundant contact interactions as visualized in fig. 1. Clearly, the peaks in the off-diagonal matrix elements in the 1S_0 , 3S_1 channels for momenta of the order of ~ 600 MeV are driven by the off-shell contact interactions. Notice that the corresponding LECs $\propto D_{1S0}^{\text{off}}$ and $\propto D_{3S1}^{\text{off}}$ were found in ref. [6] to be rather large. The behavior of these matrix elements suggests that the removal of the redundant interactions should lead to softer and more perturbative interactions. The standard method for quantifying perturbativeness of a potential is based on the Weinberg eigenvalue analysis [72, 73]. In this method, the convergence of the Born series of the Lippmann-Schwinger equation for the transfer matrix, written schematically in the operator form via

$$T(E + i\epsilon) = V + V G_0(E + i\epsilon) T(E + i\epsilon) = \sum_{n=0}^{\infty} V (G_0(E + i\epsilon) V)^n, \quad (18)$$

where $E > 0$ is the cms energy, $\epsilon \rightarrow 0^+$ and G_0 denotes the free resolvent operator, is analyzed by looking at the eigenvalues of the operator $G_0(E + i\epsilon) V$

$$G_0(E + i\epsilon) V |\Psi(E + i\epsilon)\rangle = \eta_i(E + i\epsilon) |\Psi(E + i\epsilon)\rangle, \quad (19)$$

which are complex (for $E > 0$) and form a discret set for a given value of E . The Born series converges if and only if the condition $\max(|\eta_i(E + i\epsilon)|) < 1$ is fulfilled [72, 73]. It is, therefore, instructive to look at the trajectories of the largest in magnitude Weinberg eigenvalues η in the complex plane as a function of energy E . For $E \leq 0$, all Weinberg eigenvalues are real. Positive and negative (for $E \leq 0$) eigenvalues η_i are referred to as attractive and repulsive, respectively. For NN potentials without spurious deeply bound states, the largest in magnitude attractive Weinberg eigenvalues are typically dominated by the deuteron in the ${}^3S_1-{}^3D_1$ channel and the virtual state in the 1S_0 partial wave. The corresponding attractive eigenvalues in these channels are of the order $|\eta| \sim 1$ at low energy and typically decrease in magnitude with increasing energies. On the other hand, the magnitude of repulsive eigenvalues can be significantly larger than 1 for potentials featuring a repulsive core at short distances. It is, therefore, instructive to look at the trajectories of the largest repulsive eigenvalues to quantify perturbativeness of a given potential. We refer the reader to ref. [74] and references therein for more details on the Weinberg eigenvalue analysis and applications to NN potentials derived in chiral EFT.

In the left panel of figs. 2 and 3, we show the largest repulsive Weinberg eigenvalues in the 1S_0 and ${}^3S_1-{}^3D_1$ channels, respectively, for the N^4LO SCS potentials of ref. [7]. The appearance of the repulsive eigenvalues with magnitude larger than 1 reflects the strongly nonperturbative nature of these interactions except for the two softest versions corresponding to $R = 1.1$ and 1.2 fm which, however, suffer from significant finite-cutoff artefacts. As demonstrated in figs. 2 and 3, the appearance of large repulsive Weinberg eigenvalues in the potentials of ref. [7] is a consequence of the large LECs of the redundant contact interactions at order Q^4 , as one already may expect from

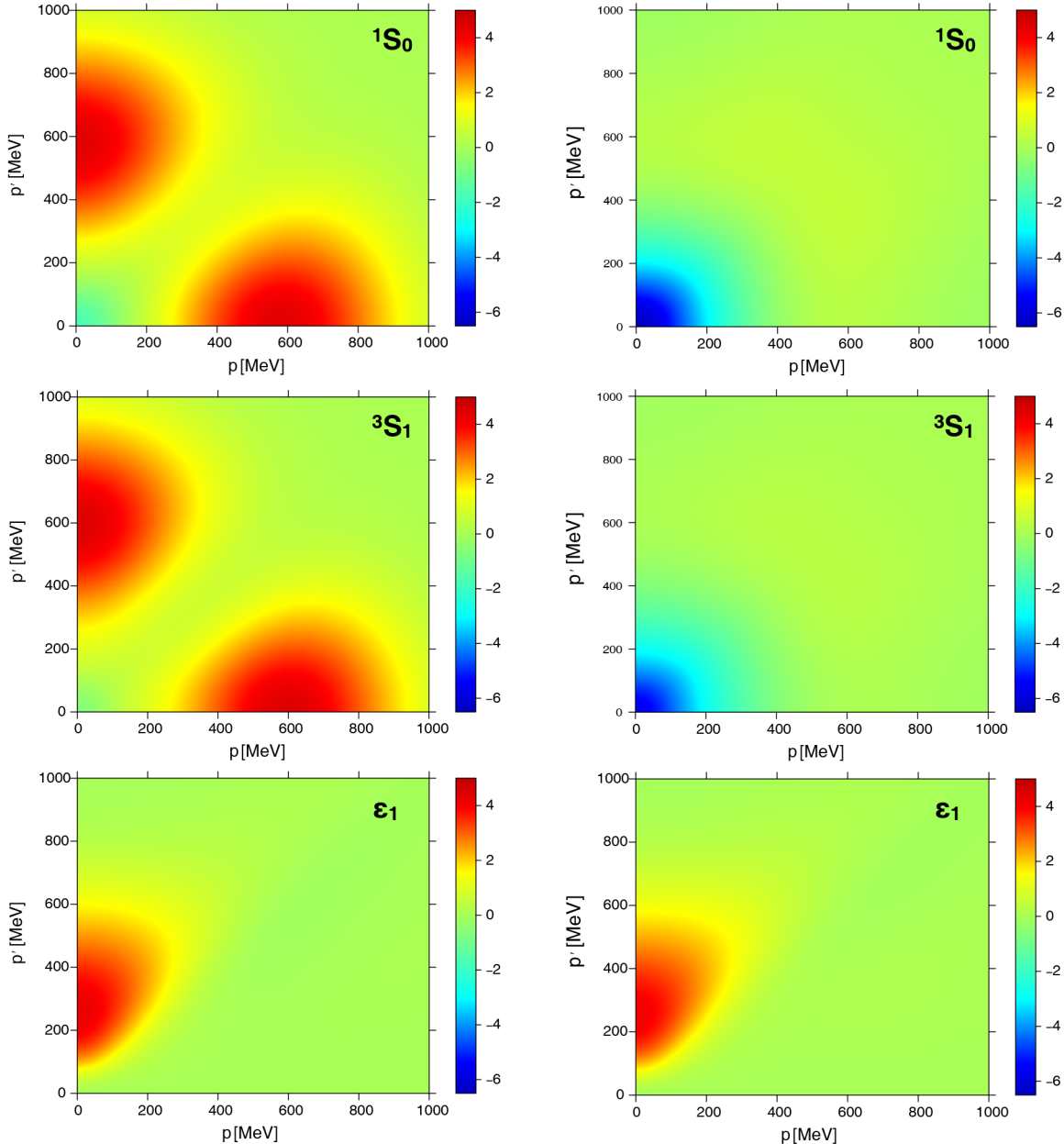


Fig. 1. (Color online) Left panel: matrix elements of the $N^4\text{LO}$ potential of ref. [7] in the 1S_0 , 3S_1 and 3S_1 - 3D_1 channels in units of GeV^{-2} . Right panel: the corresponding matrix elements after eliminating the redundant contact interactions by setting $D_{^1S0}^{\text{off}} = D_{^3S1}^{\text{off}} = D_{\epsilon_1}^{\text{off}} = 0$. In both cases, the cutoff is chosen to be $R = 0.9 \text{ MeV}$.

looking at the corresponding momentum-space matrix elements plotted in fig. 1.

4 Local regularization of long-range forces in momentum space

As already mentioned in the introduction, we employ a local regularization of the long-range interactions in momentum space. Specifically, we follow here the approach introduced in ref. [75], in which regularization is achieved by replacing the Feynman propagators for pions, exchanged

between different nucleons, by the spectral integrals via

$$\frac{1}{l^2 - M_\pi^2} \longrightarrow \int_0^\infty d\mu^2 \frac{\rho(\mu^2)}{l^2 - \mu^2 + i\epsilon}, \quad (20)$$

where $\rho(\mu^2)$ is a spectral function while l is a four-momentum of the exchanged pion. The spectral function is chosen to ensure that the static pion propagators get regularized,

$$\int_0^\infty d\mu^2 \frac{\rho(\mu^2)}{\vec{l}^2 + \mu^2} \longrightarrow \frac{F(\vec{l}^2)}{\vec{l}^2 + M_\pi^2}. \quad (21)$$

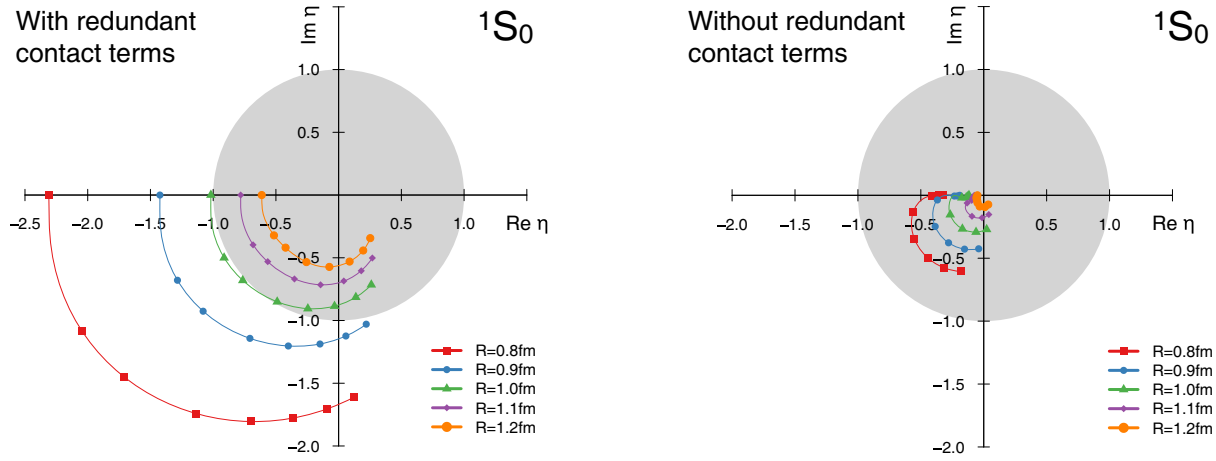


Fig. 2. (Color online) The largest in magnitude repulsive Weinberg eigenvalues η from the N^4LO SCS chiral potentials of ref. [7] at the cms energies from 0 to 300 MeV in the 1S_0 partial wave. Left (right) panel shows the results based on the original set of the order- Q^4 contact interactions as defined in ref. [6] (minimal set of independent contact interactions with the redundant terms being removed according to eqs. (12), (13)). Solid red squares, blue dots, green triangles, violet diamonds and orange circles refer to the cutoff values R of 0.8, 0.9, 1.0, 1.1 and 1.2 fm, respectively. The symbols starting from the negative real axis mark the cms energies of 0, 25, 50, 100, 150, 200, 250 and 300 MeV, in order.

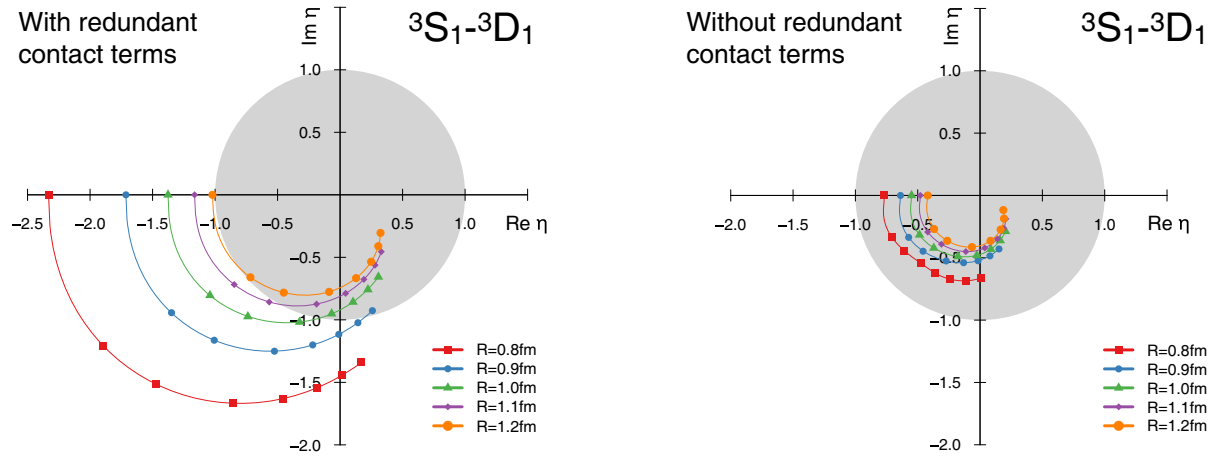


Fig. 3. (Color online) same as fig. 2 but for the $^3S_1-^3D_1$ -channel.

Here and in what follows, we choose the form factor $F(\vec{l}^2)$ to be of a Gaussian type

$$F(\vec{l}^2) = e^{-\frac{\vec{l}^2 + M_\pi^2}{\Lambda^2}}, \quad (22)$$

where Λ is an ultraviolet cutoff. Notice that the \vec{l}^2 -dependence of the form factor fixes unambiguously its M_π -dependence by the requirement that the residuum of the static pion propagator at the pion pole is unchanged. This ensures that the long-range part of the pion exchange is unaffected by the regularization (provided Λ is chosen of the order of the hard scale). Obviously, at any finite order in the $1/\Lambda^2$ -expansion, the employed regularization amounts to just adding to the unregularized one-pion exchange a sequence of contact interactions without inducing any long-range finite-cutoff artefacts.

Here and in what follows, we use the standard decomposition of the long-range potentials in momentum space

$$\begin{aligned} V(\vec{q}, \vec{k}) = & V_C(q) + \boldsymbol{\tau}_1 \cdot \boldsymbol{\tau}_2 W_C(q) \\ & + [V_S(q) + \boldsymbol{\tau}_1 \cdot \boldsymbol{\tau}_2 W_S(q)] \vec{\sigma}_1 \cdot \vec{\sigma}_2 \\ & + [V_T(q) + \boldsymbol{\tau}_1 \cdot \boldsymbol{\tau}_2 W_T(q)] \vec{\sigma}_1 \cdot \vec{q} \vec{\sigma}_2 \cdot \vec{q} \\ & + [V_{LS}(q) + \boldsymbol{\tau}_1 \cdot \boldsymbol{\tau}_2 W_{LS}(q)] i(\vec{\sigma}_1 + \vec{\sigma}_2) \cdot (\vec{q} \times \vec{k}), \end{aligned} \quad (23)$$

where $\boldsymbol{\tau}_i$ denote the Pauli isospin matrices of the nucleon i . Notice that at the order we are working, the scalar functions V_i and W_i generated by the two-pion exchange potential depend only on the momentum transfer \vec{q} . More generally, there may also be dependence on the average momentum \vec{k} . We also employ a similar decomposition in

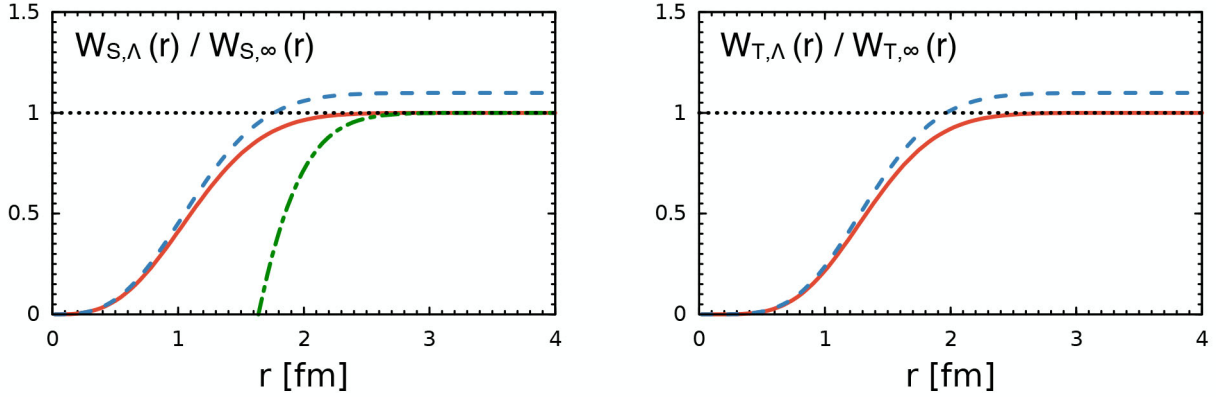


Fig. 4. (Color online) Ratio of the regularized to unregularized spin-spin (left panel) and tensor (right panel) potentials due to one-pion exchange as a function of the distance between two nucleons for the cutoff of $\Lambda = 450$ MeV. Red solid lines correspond to the employed regularization approach as given in eq. (30). Dash-dotted green line shows the result for the spin-spin potential without performing the additional subtraction, *i.e.* with $C(M_\pi) = 0$. Dashed blue lines show the results based on the regulator $\exp(-q^2/\Lambda^2)$ instead of $\exp(-(q^2 + M_\pi^2)/\Lambda^2)$.

coordinate space with

$$\begin{aligned} V(\vec{r}) &= V_C(r) + \boldsymbol{\tau}_1 \cdot \boldsymbol{\tau}_2 W_C(r) \\ &\quad + [V_S(r) + \boldsymbol{\tau}_1 \cdot \boldsymbol{\tau}_2 W_S(r)] \vec{\sigma}_1 \cdot \vec{\sigma}_2 \\ &\quad + [V_T(r) + \boldsymbol{\tau}_1 \cdot \boldsymbol{\tau}_2 W_T(r)] S_{12} \\ &\quad + [V_{LS}(r) + \boldsymbol{\tau}_1 \cdot \boldsymbol{\tau}_2 W_{LS}(r)] \vec{L} \cdot \vec{S}, \end{aligned} \quad (24)$$

where $S_{12} = \vec{\sigma}_1 \cdot \hat{r} \vec{\sigma}_2 \cdot \hat{r} - (1/3) \vec{\sigma}_1 \cdot \vec{\sigma}_2$, $\vec{S} = (\vec{\sigma}_1 + \vec{\sigma}_2)/2$ and $\vec{L} = -i\vec{r} \times \vec{\nabla}$.

Consider first the regularized expressions for the static one-pion exchange potential (OPEP)

$$\begin{aligned} V_{1\pi,\Lambda}^{pp} &= V_{1\pi,\Lambda}^{nn} = V_{1\pi,\Lambda}(M_{\pi^0}), \\ V_{1\pi,\Lambda}^{np} &= -V_{1\pi,\Lambda}(M_{\pi^0}) + 2(-1)^{I+1} V_{1\pi,\Lambda}(M_{\pi^\pm}), \end{aligned} \quad (25)$$

where I denotes the total isospin of the two-nucleon system. The above expressions include the IB correction due to the different pion masses which is the dominant long-range IB effect, see refs. [76–81] for more details on the isospin dependence of the NN force. Notice that charge dependence of the pion-nucleon coupling constant is consistent with zero [82] and for this reason will not be taken into account in the present analysis. The potential $V_{1\pi,\Lambda}(M_\pi)$ in eq. (25) has the following form in momentum space:

$$V_{1\pi,\Lambda}(M_\pi, \vec{q}) = -\frac{g_A^2}{4F_\pi^2} \left(\frac{\vec{\sigma}_1 \cdot \vec{q} \vec{\sigma}_2 \cdot \vec{q}}{q^2 + M_\pi^2} + C(M_\pi) \vec{\sigma}_1 \cdot \vec{\sigma}_2 \right) e^{-\frac{q^2 + M_\pi^2}{\Lambda^2}}, \quad (26)$$

where g_A , F_π , M_{π^0} and M_{π^\pm} are the axial-vector coupling constant of the nucleon, pion decay constant, neutral and charged pion mass, respectively. Notice that as a matter of convention, we include in the definition of the OPEP a leading-order contact interaction chosen in such a way that it minimizes the amount of short-range contributions in the regularized OPEP. More precisely, the constant $C(M_\pi)$ is determined by the requirement that

the spin-spin part of the corresponding coordinate-space potential vanishes for $r \rightarrow 0$, which leads to

$$C(M_\pi) = -\frac{\Lambda(\Lambda^2 - 2M_\pi^2) + 2\sqrt{\pi}M_\pi^3 e^{\frac{M_\pi^2}{\Lambda^2}} \operatorname{erfc}(\frac{M_\pi}{\Lambda})}{3\Lambda^3}, \quad (27)$$

where $\operatorname{erfc}(x)$ is the complementary error function

$$\operatorname{erfc}(x) = \frac{2}{\sqrt{\pi}} \int_x^\infty dt e^{-t^2}. \quad (28)$$

Using the coordinate-space expression for the regularized Yukawa potential

$$\begin{aligned} U_\Lambda(M_\pi, r) &= \int \frac{d^3 q}{(2\pi)^3} e^{i\vec{q} \cdot \vec{r}} \frac{1}{q^2 + M_\pi^2} e^{-\frac{q^2 + M_\pi^2}{\Lambda^2}} \\ &= \frac{e^{-M_\pi r} \operatorname{erfc}(\frac{M_\pi}{\Lambda} - \frac{Ar}{2}) - e^{M_\pi r} \operatorname{erfc}(\frac{M_\pi}{\Lambda} + \frac{Ar}{2})}{8\pi r}, \end{aligned} \quad (29)$$

it is easy to Fourier transform the potential $V_{1\pi,\Lambda}(M_\pi, \vec{q})$ to configuration space leading to

$$\begin{aligned} V_{1\pi,\Lambda}(M_\pi, \vec{r}) &= \int \frac{d^3 q}{(2\pi)^3} e^{i\vec{q} \cdot \vec{r}} V_{1\pi,\Lambda}(M_\pi, \vec{q}) \\ &= \frac{g_A^2}{4F_\pi^2} \left(S_{12} r \frac{\partial}{\partial r} \left(\frac{1}{r} \frac{\partial}{\partial r} \right) U_\Lambda(M_\pi, r) \right. \\ &\quad \left. + \vec{\sigma}_1 \cdot \vec{\sigma}_2 \left[\frac{M_\pi^2}{3} U_\Lambda(M_\pi, r) \right. \right. \\ &\quad \left. \left. - \left(C(M_\pi) + \frac{1}{3} \right) \frac{\Lambda^3}{8\pi^{3/2}} e^{-\frac{\Lambda^2 r^2}{4} - \frac{M_\pi^2}{\Lambda^2}} \right] \right). \end{aligned} \quad (30)$$

Up to regularization, the employed form of the static OPEP coincides with the one used in refs. [6, 7].

In fig. 4, we plot the ratio of the regularized to unregularized spin-spin and tensor potentials of the one-pion exchange (in the limit of exact isospin symmetry) for

$\Lambda = 450$ MeV, the intermediate cutoff value employed in our analysis, in comparison with the unregularized potential. One observes that the employed regulator in momentum space is indeed qualitatively similar to the coordinate-space regulator used in ref. [6]. Further, as already pointed out, it is important to keep the M_π -dependent term in the exponent of the regulator in eq. (22). Dropping this term as done *e.g.* in ref. [75] changes the strength of the one-pion exchange at the pion pole and will require renormalization of the pion-nucleon coupling constant to restore the long-range part of the OPEP. This is visualized in fig. 4 with dashed blue lines.

It is straightforward to work out the regularized expressions for the two-pion exchange potential (TPEP), see also ref. [75]. We start with a generic three-momentum loop integral emerging in the context of the method of unitary transformation [65–67], time-ordered perturbation theory [31, 83, 84] or S -matrix-based methods [85] after performing the loop integrations over the 0th momentum components. The corresponding integrands are expressed in terms of energies of the two exchanged pions $\omega_{1,2} = \sqrt{\vec{l}_{1,2}^2 + M_\pi^2}$. Using the identities given in ref. [75], it is possible to rewrite the integrals in the form which resembles a product of two static pion propagators, generally at the cost of introducing an additional integral over a mass parameter

$$I(\vec{q}) = \int d\lambda \frac{d^3 l_1}{(2\pi)^3} \frac{d^3 l_2}{(2\pi)^3} (2\pi)^3 \delta(\vec{q} - \vec{l}_1 - \vec{l}_2) \times \frac{1}{(\omega_1^2 + \lambda^2)(\omega_2^2 + \lambda^2)} \times \dots, \quad (31)$$

where \vec{q} is the nucleon momentum transfer and the ellipses refer to the isospin-spin-momentum structure emerging from vertices. Replacing the pion propagators by their regularized form as given in eqs. (21), (22), the regularized integral takes the form

$$I_A(\vec{q}) = e^{-\frac{q^2}{2\Lambda^2}} 2 \int d\lambda \frac{d^3 l}{(2\pi)^3} \frac{e^{-\frac{l^2 + 4M_\pi^2 + 4\lambda^2}{2\Lambda^2}}}{(\omega_+^2 + 4\lambda^2)(\omega_-^2 + 4\lambda^2)} \times \dots, \quad (32)$$

where $\vec{l} = \vec{l}_1 - \vec{l}_2$ and $\omega_\pm = \sqrt{(\vec{q} \pm \vec{l})^2 + 4M_\pi^2}$. Here and in what follows, we use the notation $q \equiv |\vec{q}|$, $l \equiv |\vec{l}|$. In practical calculations, the two-pion exchange contributions to the nucleon-nucleon (NN) potential are usually expressed in terms of the corresponding spectral integrals of the form

$$V(q) = \frac{2}{\pi} \int_{2M_\pi}^\infty \mu d\mu \frac{\rho(\mu)}{q^2 + \mu^2}, \quad (33)$$

with the spectral function given by $\rho(\mu) = \Im(V(q))|_{q=0+ - i\mu}$ (see footnote⁵). The explicit expressions for the spectral functions of the central, spin-spin, tensor and spin-orbit potentials up to and including N⁴LO can

⁵ One needs to introduce subtractions to render the spectral integrals finite. The required number of subtractions depends on the chiral order.

be found in refs. [4, 65, 85, 86], see also [6, 16]. It is easy to see for a general case of the TPEP that the regularization of the pion propagators introduced above leads to a particular form of the spectral function regularization, which amounts to (modulo a finite number of contact interactions) replacing $V(q)$ in eq. (33) by $V_A(q)$ given by

$$V_A(q) = e^{-\frac{q^2}{2\Lambda^2}} \frac{2}{\pi} \int_{2M_\pi}^\infty \mu d\mu \frac{\rho(\mu)}{q^2 + \mu^2} e^{-\frac{\mu^2}{2\Lambda^2}}. \quad (34)$$

The functional form of the regulator in q^2 follows from the employed regulator for the exchanged pion propagators in eqs. (21), (22) as shown in eq. (32). Since the modification of the pion propagator does not affect the pion pole contributions at any order in the $1/\Lambda$ expansion, the regularized expression for the TPEP must feature the same discontinuity across the left-hand cut as the original one in eq. (33). Together with the form of the regulator in q^2 , namely $\exp(-q^2/(2\Lambda^2))$, this then fixes unambiguously the form of the regulator in μ entering the spectral integral. Clearly, this can also be verified upon performing explicit calculations. Consider, for example, the leading two-pion exchange potential at order Q^2 [65, 85]

$$\begin{aligned} V^{(2)}(\vec{q}) = & \frac{g_A^2}{(2F_\pi)^4} \boldsymbol{\tau}_1 \cdot \boldsymbol{\tau}_2 \int \frac{d^3 l}{(2\pi)^3} \frac{l^2 - q^2}{\omega_+ \omega_- (\omega_+ + \omega_-)} \\ & - \frac{1}{8(2F_\pi)^4} \boldsymbol{\tau}_1 \cdot \boldsymbol{\tau}_2 \int \frac{d^3 l}{(2\pi)^3} \frac{(\omega_+ - \omega_-)^2}{\omega_+ \omega_- (\omega_+ + \omega_-)} \\ & - \frac{g_A^4}{2(2F_\pi)^4} \int \frac{d^3 l}{(2\pi)^3} \frac{\omega_+^2 + \omega_+ \omega_- + \omega_-^2}{\omega_+^3 \omega_-^3 (\omega_+ + \omega_-)} \\ & \times \left(\boldsymbol{\tau}_1 \cdot \boldsymbol{\tau}_2 (l^2 - q^2)^2 + 6 \vec{\sigma}_1 \cdot [\vec{q} \times \vec{l}] \vec{\sigma}_2 \cdot [\vec{q} \times \vec{l}] \right). \end{aligned} \quad (35)$$

The above integrals can be calculated in a closed form using dimensional regularization [66, 85]. The long-range behavior of the potential is determined by the non-polynomial (in momentum space) terms, which are independent of the scale introduced through dimensional regularization and have the form

$$\begin{aligned} V_{\text{non-pol.}}^{(2)}(\vec{q}) = & -\frac{\boldsymbol{\tau}_1 \cdot \boldsymbol{\tau}_2}{384\pi^2 F_\pi^4} L(q) \left\{ 4M_\pi^2 (5g_A^4 - 4g_A^2 - 1) \right. \\ & + q^2 (23g_A^4 - 10g_A^2 - 1) + \frac{48g_A^4 M_\pi^4}{4M_\pi^2 + q^2} \Big\} \\ & - \frac{3g_A^4}{64\pi^2 F_\pi^4} L(q) \left[(\vec{\sigma}_1 \cdot \vec{q}) (\vec{\sigma}_2 \cdot \vec{q}) \right. \\ & \left. - (\vec{\sigma}_1 \cdot \vec{\sigma}_2) q^2 \right], \end{aligned} \quad (36)$$

with the loop function $L(q)$ given by

$$L(q) = \frac{\sqrt{q^2 + 4M_\pi^2}}{q} \ln \frac{\sqrt{q^2 + 4M_\pi^2} + q}{2M_\pi}. \quad (37)$$

These expressions can also be represented (modulo contact terms) by means of the subtracted spectral integrals

$$\begin{aligned} W_C^{(2)}(q) &= \frac{2q^4}{\pi} \int_{2M_\pi}^\infty \frac{d\mu}{\mu^3} \frac{\eta_C^{(2)}(\mu)}{\mu^2 + q^2}, \\ V_S^{(2)}(q) &= \frac{2q^4}{\pi} \int_{2M_\pi}^\infty \frac{d\mu}{\mu^3} \frac{\rho_S^{(2)}(\mu)}{\mu^2 + q^2}, \\ V_T^{(2)}(q) &= -\frac{2q^2}{\pi} \int_{2M_\pi}^\infty \frac{d\mu}{\mu} \frac{\rho_T^{(2)}(\mu)}{\mu^2 + q^2}, \end{aligned} \quad (38)$$

where the corresponding spectral functions are given by

$$\begin{aligned} \eta_C^{(2)}(\mu) &= \Im \left(W_C^{(2)} \Big|_{q=0^+ - i\mu} \right) = \\ &\frac{1}{768\pi F_\pi^4} \left(4M_\pi^2(5g_A^4 - 4g_A^2 - 1) - \mu^2(23g_A^4 - 10g_A^2 - 1) \right. \\ &\left. + \frac{48g_A^4 M_\pi^4}{4M_\pi^2 - \mu^2} \right) \frac{\sqrt{\mu^2 - 4M_\pi^2}}{\mu}, \\ \rho_T^{(2)}(\mu) &= \Im \left(V_T^{(2)} \Big|_{q=0^+ - i\mu} \right) = \frac{1}{\mu^2} \rho_S^{(2)}(\mu) = \\ &\frac{3g_A^4}{128\pi F_\pi^4} \frac{\sqrt{\mu^2 - 4M_\pi^2}}{\mu}. \end{aligned} \quad (39)$$

Consider now the regularized expressions for the TPEP. Using the identities

$$\begin{aligned} \frac{(\omega_+ - \omega_-)^2}{\omega_+ \omega_- (\omega_+ + \omega_-)} &= \frac{1}{\omega_+} + \frac{1}{\omega_-} - \frac{4}{\omega_+ + \omega_-}, \\ \frac{\omega_+^2 + \omega_+ \omega_- + \omega_-^2}{\omega_+^3 \omega_-^3 (\omega_+ + \omega_-)} &= -\frac{4}{M_\pi} \frac{\partial}{\partial M_\pi} \frac{1}{\omega_+ \omega_- (\omega_+ + \omega_-)}, \\ \frac{1}{\omega_+ + \omega_-} &= \frac{2}{\pi} \int_0^\infty d\lambda \frac{\lambda^2}{(\omega_+^2 + \lambda^2)(\omega_-^2 + \lambda^2)}, \\ \frac{1}{\omega_+ \omega_- (\omega_+ + \omega_-)} &= \frac{2}{\pi} \int_0^\infty d\lambda \frac{1}{(\omega_+^2 + \lambda^2)(\omega_-^2 + \lambda^2)}, \\ \Im \left[\int \frac{d^3 l}{(2\pi)^3} \frac{f(l^2, q^2)}{(\omega_+^2 + \lambda^2)(\omega_-^2 + \lambda^2)} \Big|_{q=0^+ - i\mu} \right] &= \\ \frac{1}{16\mu} f(\mu^2 - 4M_\pi^2 - \lambda^2, -\mu^2) \theta(\mu - \sqrt{4M_\pi^2 + \lambda^2}), \end{aligned} \quad (40)$$

where f is a real function of l^2 and q^2 , it is easy to verify by explicitly calculating $\Im(\exp(q^2/(2\Lambda^2))V_\Lambda^{(2)}(q))|_{q=0^+ - i\mu}$ that the regularized two-pion exchange potential at NLO (modulo polynomial terms) indeed takes the form

$$\begin{aligned} W_{C,\Lambda}^{(2)}(q) &= e^{-\frac{q^2}{2\Lambda^2}} \frac{2q^4}{\pi} \int_{2M_\pi}^\infty \frac{d\mu}{\mu^3} \frac{\eta_C^{(2)}(\mu)}{\mu^2 + q^2} e^{-\frac{\mu^2}{2\Lambda^2}}, \\ V_{S,\Lambda}^{(2)}(q) &= e^{-\frac{q^2}{2\Lambda^2}} \frac{2q^4}{\pi} \int_{2M_\pi}^\infty \frac{d\mu}{\mu^3} \frac{\rho_S^{(2)}(\mu)}{\mu^2 + q^2} e^{-\frac{\mu^2}{2\Lambda^2}}, \\ V_{T,\Lambda}^{(2)}(q) &= -e^{-\frac{q^2}{2\Lambda^2}} \frac{2q^2}{\pi} \int_{2M_\pi}^\infty \frac{d\mu}{\mu} \frac{\rho_T^{(2)}(\mu)}{\mu^2 + q^2} e^{-\frac{\mu^2}{2\Lambda^2}}. \end{aligned} \quad (41)$$

Thus, the regularized expressions for the two-pion exchange potential can be easily obtained by using the

known analytical results for the corresponding spectral functions and employing the exponential regulator when performing the spectral integrals. As already pointed out above, this fixes the expressions for the two-pion exchange modulo contact interactions allowed at the given order in the chiral expansion. Here and in what follows, we eliminate this ambiguity by imposing a convention that the corresponding long-range potentials in coordinate space and derivatives thereof vanish at the origin. Such an approach qualitatively resembles the behavior of the coordinate-space regulator used in ref. [6].

To be specific we provide below the explicit expressions for the regularized long-range part of the two-pion exchange potential at different orders in the chiral expansion in terms of the corresponding spectral integrals.

- NLO

$$\begin{aligned} W_{C,\Lambda}^{(2)}(q) &= e^{-\frac{q^2}{2\Lambda^2}} \frac{2}{\pi} \int_{2M_\pi}^\infty \frac{d\mu}{\mu^3} \eta_C^{(2)}(\mu) \\ &\times \left(\frac{q^4}{\mu^2 + q^2} + C_{C,1}^2(\mu) + C_{C,2}^2(\mu) q^2 \right) e^{-\frac{\mu^2}{2\Lambda^2}}, \\ V_{S,\Lambda}^{(2)}(q) &= e^{-\frac{q^2}{2\Lambda^2}} \frac{2}{\pi} \int_{2M_\pi}^\infty \frac{d\mu}{\mu^3} \rho_S^{(2)}(\mu) \\ &\times \left(\frac{q^4}{q^2 + \mu^2} + C_{S,1}^2(\mu) + C_{S,2}^2(\mu) q^2 \right) e^{-\frac{\mu^2}{2\Lambda^2}}, \\ V_{T,\Lambda}^{(2)}(q) &= -e^{-\frac{q^2}{2\Lambda^2}} \frac{2}{\pi} \int_{2M_\pi}^\infty \frac{d\mu}{\mu^3} \rho_S^{(2)}(\mu) \\ &\times \left(\frac{q^2}{\mu^2 + q^2} + C_T^1(\mu) \right) e^{-\frac{\mu^2}{2\Lambda^2}}, \end{aligned} \quad (42)$$

where the superscript a of the functions $C_{C,i}^a(\mu)$, $C_{S,i}^a(\mu)$ and $C_T^a(\mu)$ refers to the number of subtractions. The corresponding spectral functions are specified in eq. (39), while the functions $C_{C,i}^2(\mu)$, $C_{S,i}^2(\mu)$, and $C_T^1(\mu)$ are determined by the required short-distance behavior of the coordinate-space potentials:

$$\begin{aligned} W_{C,\Lambda}^{(2)}(0) &= \frac{d^2}{dr^2} W_{C,\Lambda}^{(2)}(r) \Big|_{r=0} = V_{S,\Lambda}^{(2)}(0) \\ &= \frac{d^2}{dr^2} V_{S,\Lambda}^{(2)}(r) \Big|_{r=0} \\ &= \frac{d^2}{dr^2} V_{T,\Lambda}^{(2)}(r) \Big|_{r=0} = 0. \end{aligned} \quad (43)$$

Their explicit form can be found in appendix B.
- N²LO

$$\begin{aligned} V_{C,\Lambda}^{(3)}(q) &= e^{-\frac{q^2}{2\Lambda^2}} \frac{2}{\pi} \int_{2M_\pi}^\infty \frac{d\mu}{\mu^3} \rho_C^{(3)}(\mu) \\ &\times \left(\frac{q^4}{\mu^2 + q^2} + C_{C,1}^2(\mu) + C_{C,2}^2(\mu) q^2 \right) e^{-\frac{\mu^2}{2\Lambda^2}}, \end{aligned}$$

$$\begin{aligned} W_{S,A}^{(3)}(q) &= e^{-\frac{q^2}{2A^2}} \frac{2}{\pi} \int_{2M_\pi}^\infty \frac{d\mu}{\mu^3} \eta_S^{(3)}(\mu) \\ &\times \left(\frac{q^4}{q^2 + \mu^2} + C_{S,1}^2(\mu) + C_{S,2}^2(\mu) q^2 \right) e^{-\frac{\mu^2}{2A^2}}, \\ W_{T,A}^{(3)}(q) &= -e^{-\frac{q^2}{2A^2}} \frac{2}{\pi} \int_{2M_\pi}^\infty \frac{d\mu}{\mu^3} \eta_S^{(3)}(\mu) \\ &\times \left(\frac{q^2}{\mu^2 + q^2} + C_T^1(\mu) \right) e^{-\frac{\mu^2}{2A^2}}, \end{aligned} \quad (44)$$

where the corresponding spectral functions are given by

$$\begin{aligned} \rho_C^{(3)}(\mu) &= -\frac{3g_A^2}{64F_\pi^4} (2M_\pi^2(2c_1 - c_3) + c_3\mu^2) \frac{(2M_\pi^2 - \mu^2)}{\mu}, \\ \eta_S^{(3)}(\mu) &= -\frac{g_A^2}{128F_\pi^4} c_4 \mu (4M_\pi^2 - \mu^2). \end{aligned} \quad (45)$$

- N³LO

The static contributions to the TPEP are given by

$$\begin{aligned} X_{C,A}^{(4)}(q) &= -e^{-\frac{q^2}{2A^2}} \frac{2}{\pi} \int_{2M_\pi}^\infty \frac{d\mu}{\mu^5} x_C^{(4)}(\mu) \\ &\times \left(\frac{q^6}{\mu^2 + q^2} + C_{C,1}^3(\mu) + C_{C,2}^3(\mu) q^2 + C_{C,3}^3(\mu) q^4 \right) e^{-\frac{\mu^2}{2A^2}}, \\ X_{S,A}^{(4)}(q) &= -e^{-\frac{q^2}{2A^2}} \frac{2}{\pi} \int_{2M_\pi}^\infty \frac{d\mu}{\mu^5} x_S^{(4)}(\mu) \\ &\times \left(\frac{q^6}{q^2 + \mu^2} + C_{S,1}^3(\mu) + C_{S,2}^3(\mu) q^2 + C_{S,3}^3(\mu) q^4 \right) e^{-\frac{\mu^2}{2A^2}}, \\ X_{T,A}^{(4)}(q) &= e^{-\frac{q^2}{2A^2}} \frac{2}{\pi} \int_{2M_\pi}^\infty \frac{d\mu}{\mu^5} x_S^{(4)}(\mu) \\ &\times \left(\frac{q^4}{\mu^2 + q^2} + C_{T,1}^2(\mu) + C_{T,2}^2(\mu) q^2 \right) e^{-\frac{\mu^2}{2A^2}}, \end{aligned} \quad (46)$$

where X and x refer to either V and ρ or to W and η , respectively. The functions $C_{C,i}^3(\mu)$, $C_{S,i}^3(\mu)$, and $C_{T,i}^2(\mu)$ are determined by the conditions

$$\begin{aligned} X_{C,A}^{(4)}(0) &= \left. \frac{d^2}{dr^2} X_{C,A}^{(4)}(r) \right|_{r=0} = \left. \frac{d^4}{dr^4} X_{C,A}^{(4)}(r) \right|_{r=0} = 0, \\ X_{S,A}^{(4)}(0) &= \left. \frac{d^2}{dr^2} X_{S,A}^{(4)}(r) \right|_{r=0} = \left. \frac{d^4}{dr^4} X_{S,A}^{(4)}(r) \right|_{r=0} = 0, \\ \left. \frac{d^2}{dr^2} X_{T,A}^{(4)}(r) \right|_{r=0} &= \left. \frac{d^4}{dr^4} X_{T,A}^{(4)}(r) \right|_{r=0} = 0, \end{aligned} \quad (47)$$

and are listed in appendix B. The spectral functions $\rho_C^{(4)}(\mu)$, $\rho_S^{(4)}(\mu)$, $\eta_C^{(4)}(\mu)$ and $\eta_S^{(4)}(\mu)$ have been derived in ref. [86]. The two-loop contributions are also listed in eq. (12) of ref. [6]. The spectral functions corresponding to the one-loop contributions proportional to the LECs c_i^2 can be extracted from the TPEP contributions given in eq. (10) of this reference via replacements $L(q) \rightarrow -\pi/(2\mu)\sqrt{\mu^2 - 4M_\pi^2}$ and $q^2 \rightarrow -\mu^2$.

In addition to the static contributions, one also needs to account for the leading $1/m_N$ -corrections to the TPEP. Here and in what follows, m_N refers to the nucleon mass, for which we use the value $m_N = 2m_p m_n / (m_p + m_n)$ in terms of the proton and neutron masses m_p and m_n , respectively. Throughout this work, we employ the same treatment of the relativistic corrections as in our previous papers [6, 7]. Specifically, we use the Schrödinger equation as given in eq. (20) of ref. [6] at all considered orders and adopt the “minimal nonlocality” choice for the two unitary transformations which affect the $1/m_N^2$ -contributions to the OPEP and $1/m_N$ -contributions to the TPEP at N³LO. Thus, all unregularized expressions for the relativistic corrections to the TPEP given in ref. [6] remain valid in our case. The regularized expressions for the leading relativistic corrections to the TPEP are written in terms of the spectral integrals

$$\begin{aligned} X_{C,A}^{(4)}(q) &= e^{-\frac{q^2}{2A^2}} \frac{2}{\pi} \int_{2M_\pi}^\infty \frac{d\mu}{\mu^3} x_C^{(4)}(\mu) \\ &\times \left(\frac{q^4}{\mu^2 + q^2} + C_{C,1}^2(\mu) + C_{C,2}^2(\mu) q^2 \right) e^{-\frac{\mu^2}{2A^2}}, \\ X_{S,A}^{(4)}(q) &= e^{-\frac{q^2}{2A^2}} \frac{2}{\pi} \int_{2M_\pi}^\infty \frac{d\mu}{\mu^3} x_S^{(4)}(\mu) \\ &\times \left(\frac{q^4}{q^2 + \mu^2} + C_{S,1}^2(\mu) + C_{S,2}^2(\mu) q^2 \right) e^{-\frac{\mu^2}{2A^2}}, \\ X_{T,A}^{(4)}(q) &= -e^{-\frac{q^2}{2A^2}} \frac{2}{\pi} \int_{2M_\pi}^\infty \frac{d\mu}{\mu^3} x_S^{(4)}(\mu) \\ &\times \left(\frac{q^2}{\mu^2 + q^2} + C_T^1(\mu) \right) e^{-\frac{\mu^2}{2A^2}}, \\ X_{LS,A}^{(4)}(q) &= -e^{-\frac{q^2}{2A^2}} \frac{2}{\pi} \int_{2M_\pi}^\infty \frac{d\mu}{\mu} x_{LS}^{(4)}(\mu) \\ &\times \left(\frac{q^2}{\mu^2 + q^2} + C_{LS}^1(\mu) \right) e^{-\frac{\mu^2}{2A^2}}, \end{aligned} \quad (48)$$

where, again, X and x stay for either V and ρ or W and η , respectively. The function $C_{LS}^1(\mu)$ is determined by the requirement

$$\left. \frac{d}{dr} X_{LS,A}^{(4)}(r) \right|_{r=0} = 0 \quad (49)$$

and can be found in appendix B. The corresponding spectral functions can be read off from the expressions for the potentials derived in refs. [85, 87] and given in eqs. (19) and (22) of ref. [6] upon performing the replacements $A(q) \rightarrow \pi/(4\mu)$ and $q^2 \rightarrow -\mu^2$ in the non-pole contributions (*i.e.* in the contributions proportional to the loop function $A(q)$). The regularized expressions for the pole contributions to $V_C^{(4)}$ and $W_C^{(4)}$

in eq. (19) of ref. [6] take the form

$$V_{C,A}^{(4)}(q) = \frac{1}{2} W_{C,A}^{(4)}(q) = \frac{3g_A^4 M_\pi^5}{256\pi m_N F_\pi^4} \left(\frac{1}{q^2 + 4M_\pi^2} + C_1^2 + C_2^2 q^2 \right) e^{-\frac{q^2 + 4M_\pi^2}{2A^2}}, \quad (50)$$

where the constants C_1^2 and C_2^2 are determined by the requirement that the corresponding r -space potentials and their second derivatives vanish at the origin and are specified in appendix B.

– N⁴LO

Finally, regularized N⁴LO contributions to the TPEP have the form

$$\begin{aligned} X_{C,A}^{(5)}(q) &= -e^{-\frac{q^2}{2A^2}} \frac{2}{\pi} \int_{2M_\pi}^{\infty} \frac{d\mu}{\mu^5} x_C^{(5)}(\mu) \\ &\times \left(\frac{q^6}{\mu^2 + q^2} + C_{C,1}^3(\mu) + C_{C,2}^3(\mu) q^2 + C_{C,3}^3(\mu) q^4 \right) e^{-\frac{\mu^2}{2A^2}}, \\ X_{S,A}^{(5)}(q) &= -e^{-\frac{q^2}{2A^2}} \frac{2}{\pi} \int_{2M_\pi}^{\infty} \frac{d\mu}{\mu^5} x_S^{(5)}(\mu) \\ &\times \left(\frac{q^6}{q^2 + \mu^2} + C_{S,1}^3(\mu) + C_{S,2}^3(\mu) q^2 + C_{S,3}^3(\mu) q^4 \right) e^{-\frac{\mu^2}{2A^2}}, \\ X_{T,A}^{(5)}(q) &= e^{-\frac{q^2}{2A^2}} \frac{2}{\pi} \int_{2M_\pi}^{\infty} \frac{d\mu}{\mu^5} x_S^{(5)}(\mu) \\ &\times \left(\frac{q^4}{\mu^2 + q^2} + C_{T,1}^2(\mu) + C_{T,2}^2(\mu) q^2 \right) e^{-\frac{\mu^2}{2A^2}}, \\ X_{LS,A}^{(5)}(q) &= e^{-\frac{q^2}{2A^2}} \frac{2}{\pi} \int_{2M_\pi}^{\infty} \frac{d\mu}{\mu^3} x_{LS}^{(5)}(\mu) \\ &\times \left(\frac{q^4}{\mu^2 + q^2} + C_{LS,1}^2(\mu) + C_{LS,2}^2(\mu) q^2 \right) e^{-\frac{\mu^2}{2A^2}}, \end{aligned} \quad (51)$$

where the functions $C_{LS,1}^2(\mu)$ and $C_{LS,2}^2(\mu)$ are determined by the requirements

$$\frac{d}{dr} X_{LS,A}^{(5)}(r) \Big|_{r=0} = \frac{d^3}{dr^3} X_{LS,A}^{(5)}(r) \Big|_{r=0} = 0 \quad (52)$$

and are given in appendix B. The spectral functions $\rho_C^{(5)}$, $\rho_S^{(5)}$, $\eta_C^{(5)}$ and $\eta_S^{(5)}$ receive contributions from the static terms which are given in ref. [4]. In addition, one has to account for the relativistic corrections $\propto c_i/m_N$. The corresponding contributions to the spectral functions can be read off from eqs. (13)–(17) of ref. [86] by performing the replacements $L(q) \rightarrow -\pi/(2\mu)\sqrt{\mu^2 - 4M_\pi^2}$ and $q^2 \rightarrow -\mu^2$ (see footnote⁶).

It is instructive to compare various regularization approaches for the TPEP with each other. To this end, we consider the isovector central TPEP at NLO $W_C^{(2)}$ as a representative example. Its non-regularized momentum-space expression $W_{C,\infty}^{(2)}$ is given in the first line of eq. (36)

⁶ Notice that refs. [4, 86] use a different sign convention in the definition of the potential.

up to irrelevant polynomial terms. While the Fourier transform of $W_{C,\infty}^{(2)}(q)$ does not exist, one can define its coordinate-space representation via the limit

$$W_{C,\infty}^{(2)}(r) = \lim_{A \rightarrow \infty} \int \frac{d^3 q}{(2\pi)^3} e^{iq \cdot r} W_{C,\infty}^{(2)}(q) e^{-\frac{q^2}{A^2}}, \quad (53)$$

which exists for $r > 0$. The resulting potential can be obtained in a more convenient way by making use of the spectral representation which leads to [85]

$$\begin{aligned} W_{C,\infty}^{(2)}(r) &= \frac{1}{2\pi^2 r} \int_{2M_\pi}^{\infty} d\mu \mu e^{-\mu r} \eta_C^{(2)}(\mu) \\ &= \frac{M_\pi}{128\pi^3 F_\pi^4 r^4} \left[(1 + 2g_A^2(5 + 2x^2) \right. \\ &\quad \left. - g_A^4(23 + 12x^2)) K_1(2x) \right. \\ &\quad \left. + x(1 + 10g_A^2 - g_A^4(23 + 4x^2)) K_0(2x) \right], \end{aligned}$$

where $x \equiv M_\pi r$ and $K_i(x)$ denote the modified Bessel-functions. We regard this expression as our reference potential in coordinate space. We now consider four different ways to implement regularization as described below.

- 1) First, we retain only the momentum-independent part of the Gaussian regulator in eq. (34) responsible for the spectral function regularization. The corresponding coordinate-space TPEP can be calculated by means of the spectral integral

$$W_{C,A,1}^{(2)}(r) = \frac{1}{2\pi^2 r} \int_{2M_\pi}^{\infty} d\mu \mu e^{-\mu r} \eta_C^{(2)}(\mu) e^{-\frac{\mu^2}{2A^2}}. \quad (54)$$

- 2) Next, we follow the opposite approach and retain only the momentum-dependent part of the regulator without introducing spectral function regularization. The regularized potential is defined by means of the twice subtracted spectral integral

$$\begin{aligned} W_{C,A,2}^{(2)}(q) &= e^{-\frac{q^2}{2A^2}} \frac{2}{\pi} \int_{2M_\pi}^{\infty} \frac{d\mu}{\mu^3} \eta_C^{(2)}(\mu) \frac{q^4}{\mu^2 + q^2}, \\ W_{C,A,2}^{(2)}(r) &= \frac{1}{2\pi^2} \int q^2 dq j_0(qr) W_{C,A,2}^{(2)}(q). \end{aligned} \quad (55)$$

Alternatively, one can simply multiply $W_{C,\infty}^{(2)}(q)$ by the regulator $e^{-\frac{q^2}{2A^2}}$, which leads to a different admixture of contact interactions. We found, however, that this definition leads to larger distortions at short distances as compared to the one in eq. (55).

- 3) In the third approach, the regularized potential is defined according to eq. (42) but without explicitly subtracting the short-range terms, *i.e.*

$$W_{C,A,3}^{(2)}(q) = e^{-\frac{q^2}{2A^2}} \frac{2}{\pi} \int_{2M_\pi}^{\infty} \frac{d\mu}{\mu^3} \eta_C^{(2)}(\mu) \frac{q^4}{\mu^2 + q^2} e^{-\frac{\mu^2}{2A^2}}, \quad (56)$$

and the Fourier transform to coordinate space can be performed using the second relation in eq. (55).

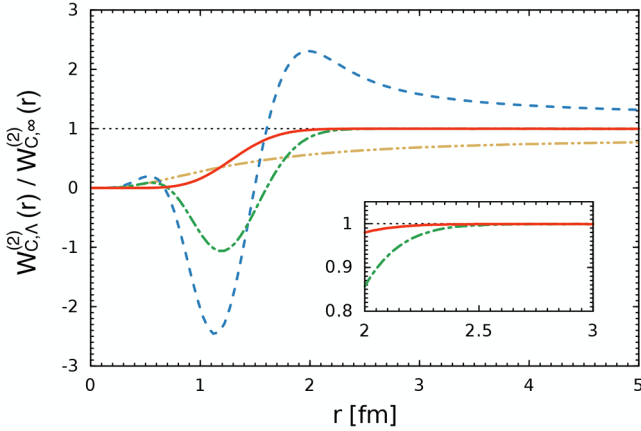


Fig. 5. (Color online) Ratios $W_{C,\Lambda,i}^{(2)}(r)/W_{C,\infty}^{(2)}(r)$ for different implementations of the regularization $i = 1, \dots, 4$ defined in the text as a function of the relative distance between the nucleons. Dash-double-dotted light-brown, dashed blue, dash-dotted green and solid red lines refer to $i = 1, 2, 3$ and 4 , respectively. The cutoff Λ is set to be $\Lambda = 450$ MeV. The dotted horizontal line corresponds to the unregularized potential, *i.e.*, the ratio is equal to 1.

4) Finally, the approach to define the regularized potential $W_{C,\Lambda}^{(2)}(q)$ adopted in the present analysis is

$$W_{C,\Lambda,4}^{(2)}(q) = e^{-\frac{q^2}{2\Lambda^2}} \frac{2}{\pi} \int_{2M_\pi}^{\infty} \frac{d\mu}{\mu^3} \eta_C^{(2)}(\mu) \times \left(\frac{q^4}{\mu^2 + q^2} + C_{C,1}^2(\mu) + C_{C,2}^2(\mu) q^2 \right) e^{-\frac{\mu^2}{2\Lambda^2}}, \quad (57)$$

where the functions $C_{C,i}^2(\mu)$ are determined as described above and given in appendix B.

In fig. 5, we show the ratios of the potentials $W_{C,\Lambda,i}^{(2)}(r)$, with $i = 1, \dots, 4$, to the unregularized expression $W_{C,\infty}^{(2)}(r)$. As before, we use the intermediate value of the cutoff of $\Lambda = 450$ MeV. Retaining either only the momentum-transfer- or the μ -dependent part of the regulator in eq. (34), *i.e.* refraining from performing the spectral function or momentum regularization, strongly affects the long-range part of the TPEP and results in large deviations from the unregularized TPEP even at rather large distances. While both the third and fourth approaches maintain the long-range part of the TPEP, one observes that our final approach, which minimizes the amount of short-range contributions in the long-range potentials, leads to the smoothest behavior at intermediate distances with the smallest amount of distortions, similarly to what has been observed in the case of the OPEP in fig. 4. Notice further that the resulting coordinate-space behavior of the regularized potentials is qualitatively similar to that of potentials in ref. [6].

After these preparations, we have all the necessary tools to address the convergence of the chiral expansion for the long-range interactions in a meaningful way. In figs. 6 and 7, we show the chiral expansion of the long-range

isoscalar and isovector potentials $V_{i,\Lambda}(r)$ and $W_{i,\Lambda}(r)$. While we employ in this work the cutoff values in the range of $\Lambda = 350 \dots 550$ MeV, here we only show the results for the intermediate cutoff value of $\Lambda = 450$ MeV as representative examples. The values of the pion-nucleon (πN) LECs are taken from the recent analysis of πN scattering in the framework of the Roy-Steiner equation [88] as discussed in sect. 6.1. Notice that the vanishing of the corresponding central and spin-spin potentials at short distances is enforced by the adopted convention in our definition of the long-range contributions as discussed above. It should be understood that the short-distance behavior of $V_{i,\Lambda}(r)$ and $W_{i,\Lambda}(r)$ is scheme dependent which manifests itself *e.g.* in their strong dependence on Λ . On the other hand, we found that the profile functions are largely insensitive to the considered cutoff variation at distances of $r \gtrsim 2$ fm. The strongest long-range potentials are generated by the OPEP in the isovector tensor channel and the TPEP in the isoscalar singlet channel, the feature which follows from the large- N_c analysis of nuclear forces [89] and is also supported by phenomenological studies. Generally, one observes a fairly good convergence of the chiral expansion except for the cases where the corresponding potentials are weak such as especially the isovector spin-orbit and, to a lesser extent, the isovector central potentials $W_{LS,\Lambda}(r)$ and $W_{C,\Lambda}(r)$, respectively. Notice that while in these cases the N^4 LO contribution appears to be much larger than the N^3 LO one, its absolute size is comparable in magnitude with the size of N^4 LO contributions in other channels. We further emphasize that the somewhat peculiar convergence pattern of the chiral expansion of the TPEP at orders NLO and N^2 LO is, to a large extent, related to the implicit treatment of the $\Delta(1232)$ resonance. This results in numerically large values of the subleading pion-nucleon LECs c_3 and c_4 and leads to enhanced subleading contributions to the TPEP. The convergence of the chiral expansion for the long-range part of the nuclear forces is improved in the chiral EFT formulation with explicit Δ degrees of freedom [84, 90–93]. Clearly, final conclusions on the convergence of the chiral expansion can only be drawn from looking at observables rather than profile functions. Further discussion is thus relegated to sect. 7.

To summarize the main results of this section, we have introduced a momentum-space regularization framework for pion exchange contributions by regularizing the static propagators of pions exchanged between different nucleons. Our approach maintains the long-range part of the interaction and can be easily implemented at the level of the spectral representation of the TPEP with no need to recalculate loop integrals entering the definition of the potential. The method is highly flexible and by no means restricted to the cases where the spectral function representation is available. In particular, it can be easily applied to the ring diagrams appearing in the three-nucleon force starting from N^3 LO [34, 69] by switching to coordinate space. It can also be employed straightforwardly to regularize the exchange electroweak charge and current operators derived using the method of unitary transformation [37–39] or based on time-ordered perturbation

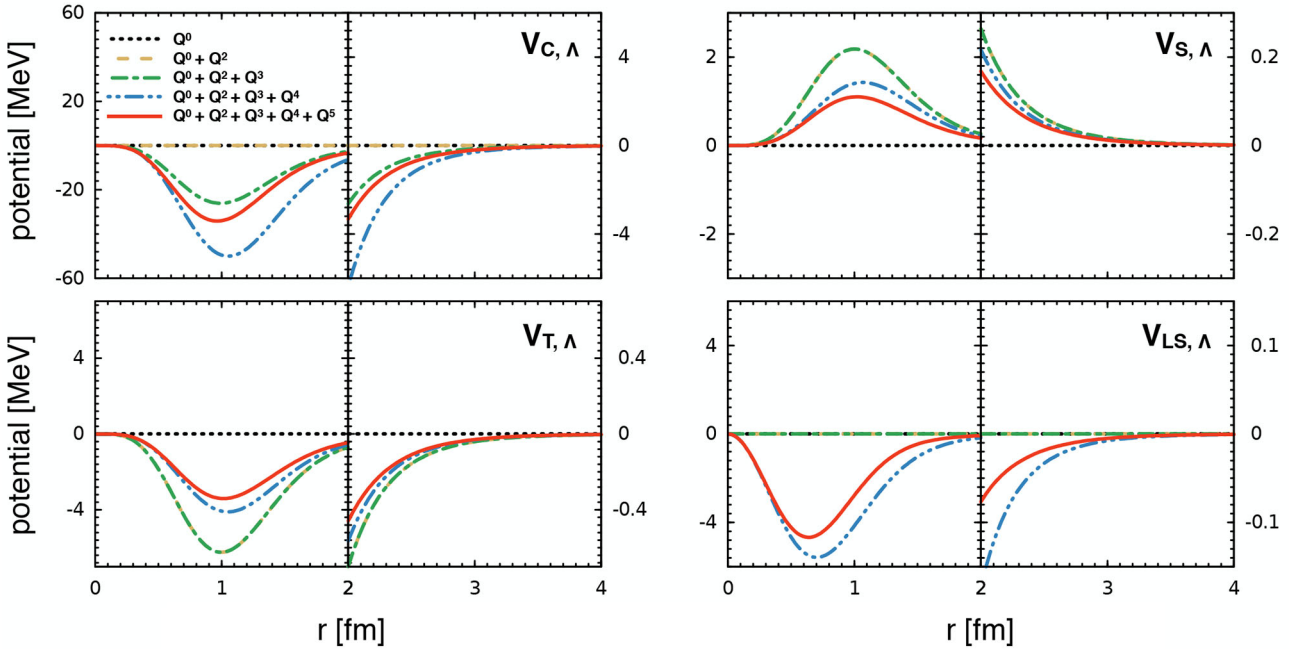


Fig. 6. (Color online) Chiral expansion of the regularized long-range isoscalar potentials $V_{i,A}(r)$ for the cutoff value of $A = 450$ MeV. Black dotted, orange dashed, green dash-dotted, blue dash-double-dotted and red solid lines refer to LO, NLO, N^2 LO, N^3 LO and N^4 LO, respectively.

theory [40–42]. Notice that in contrast with the simple coordinate-space regularization scheme of ref. [6], the new approach, being less phenomenological, determines unambiguously the form of the regulator in *e.g.* the ring contributions to the three-nucleon force.

5 Scattering amplitude in the presence of electromagnetic interactions

In addition to the strong nuclear force, the inclusion of electromagnetic interactions is mandatory for an accurate description of NN observables. We follow the treatment of the Nijmegen PWA [20] and include for np scattering the magnetic moment potential

$$V_{MM}^{np}(r) = -\frac{\alpha \kappa_n}{2m_nr^3} \left[\frac{3\mu_p}{2m_p} S_{12} + \frac{1}{m_r} (\vec{L} \cdot \vec{S} + \vec{L} \cdot \vec{A}) \right], \quad (58)$$

where $\vec{A} = (\vec{\sigma}_1 - \vec{\sigma}_2)/2$. Furthermore, m_r is the np reduced mass, μ_p is the proton magnetic moment and κ_n denotes the neutron anomalous magnetic moment. For pp scattering, we include the so-called improved Coulomb potentials V_{C1} , V_{C2} , the magnetic moment potential V_{MM}^{pp} and the

vacuum polarization potential V_{VP}

$$V_{C1}(r) = \frac{\alpha'}{r}, \quad (59)$$

$$V_{C2}(r) = -\frac{1}{m_p^2} \left[(\Delta + q^2) \frac{\alpha}{r} + \frac{\alpha}{r} (\Delta + q^2) \right] \approx -\frac{\alpha \alpha'}{m_p^2} \frac{1}{r^2}, \quad (60)$$

$$V_{VP}(r) = \frac{2\alpha}{3\pi} \frac{\alpha'}{r} \int_1^\infty e^{-2m_e rx} \left(1 + \frac{1}{2x^2} \right) \frac{\sqrt{x^2 - 1}}{x^2} dx, \quad (61)$$

$$V_{MM}^{pp}(r) = -\frac{\alpha}{4m_p^2 r^3} \left[3\mu_p^2 S_{12} + (6 + 8\kappa_p) \vec{L} \cdot \vec{S} \right]. \quad (62)$$

The energy-dependent factor α' is defined as

$$\alpha' = \alpha \left(1 + \frac{2q^2}{m_p^2} \right) \left(1 + \frac{q^2}{m_p^2} \right)^{-\frac{1}{2}}. \quad (63)$$

The magnetic moment potential $V_{MM}^{np/pp}$ has been derived from the one-photon-exchange diagram while V_{C1} and V_{C2} also include contributions from the two-photon-exchange box and cross-boxed diagrams [94]. The vacuum polarization is a loop correction and of a finite range as opposed to the other electromagnetic (e.m.) interactions. In spite of its finite (but still very long) range, it can be important at low energies [95].

The potentials given above only represent the long-range part of the e.m. interaction. The short-range part of those interactions can be represented by contact terms which are of the same type as the contact interactions already included in the nuclear potential. Thus, these effects

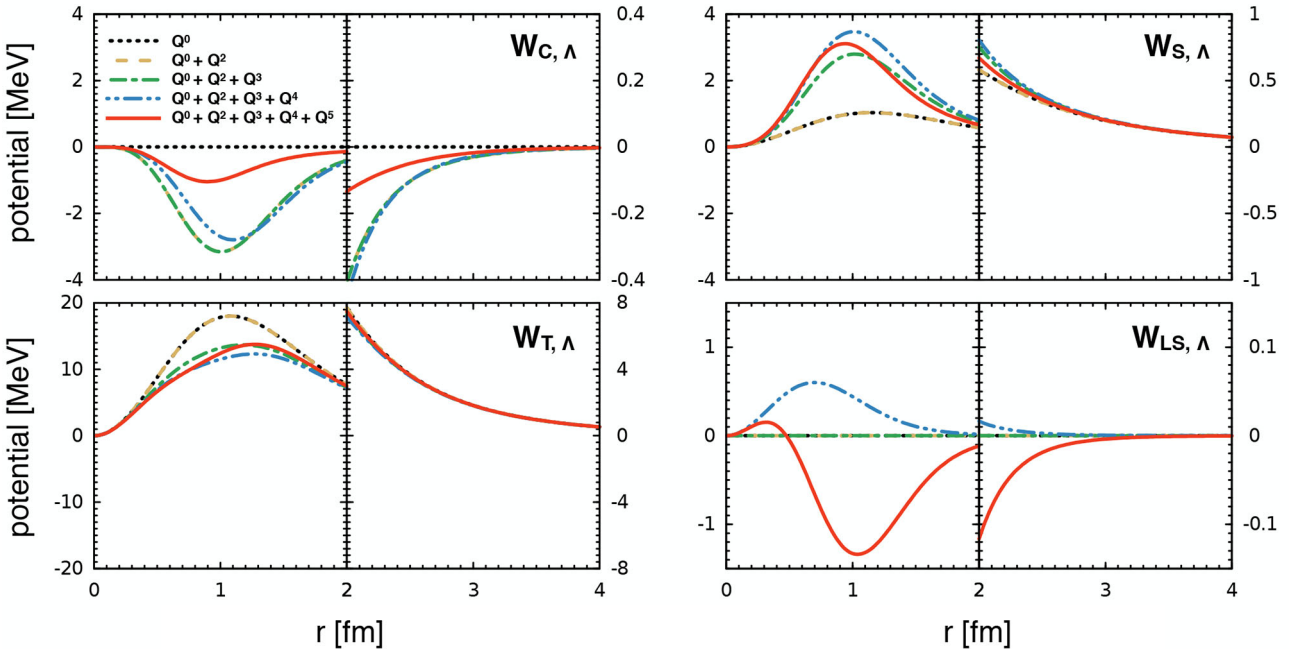


Fig. 7. (Color online) Chiral expansion of the regularized long-range isovector potentials $W_{i,\Lambda}(r)$ for the cutoff value of $\Lambda = 450$ MeV. Black dotted, orange dashed, green dash-dotted, blue dash-double-dotted and red solid lines refer to LO, NLO, N^2 LO, N^3 LO and N^4 LO, respectively.

are implicitly incorporated into the values of the corresponding LECs.

The partial wave expansion of the amplitude converges only slowly in the presence of long-range e.m. interactions. Therefore, the e.m. amplitudes are separated from the nuclear amplitude, allowing fast recalculation of the nuclear amplitude during the fitting process by summing nuclear partial waves up to the total angular momentum $j = 20$, while the e.m. amplitudes need to be calculated only once. The total amplitudes are given by

$$M_{np} = M_{MM} + M_N, \quad (64)$$

$$M_{pp} = M_{C1} + M_{C2} + M_{MM} + M_{VP} + M_N. \quad (65)$$

In the case of np scattering both the amplitude and the nuclear phase shifts are calculated with respect to Riccati-Bessel functions. The analytic expression of the magnetic moment amplitude in terms of the Saclay amplitudes can be found *e.g.* in [96, 97], where the point-particle approximation corresponds to the following Dirac and Pauli form factors:

$$F_1^p = 1, \quad F_1^n = 0, \quad F_2^p = \frac{\kappa_p}{2m_p}, \quad F_2^n = \frac{\kappa_n}{2m_n}, \quad (66)$$

with the anomalous magnetic moments $\kappa_p = 1.792847$ and $\kappa_n = -1.913043$.

Due to the amplitude separation, the nuclear partial wave S -matrix elements have to be adjusted as $S_N - 1 \rightarrow (S_{MM})^{1/2}(S_N - 1)(S_{MM})^{1/2}$ when calculating the nuclear amplitude, with S_{MM} being the partial wave S -matrix elements of the magnetic moment interaction. We again refer to [96] for explicit expressions and a detailed discussion.

For pp scattering, the potentials V_{C1} , V_{C2} and V_{VP} are spin-independent and their anti-symmetrized spin-scattering matrix is given by

$$M_{m'_s, m_s}^s = [f_X(\theta) + (-1)^s f_X(\pi - \theta)] \delta_{m'_s m_s}, \quad (67)$$

where X can be $C1$, $C2$ or VP . The amplitude f_{C1} is given by

$$\begin{aligned} f_{C1}(\theta) &= \frac{1}{2iq} \sum_l (2l+1) \left(e^{2i(\sigma_l - \sigma_0)} - 1 \right) P_l(\theta) \\ &= -\frac{\eta'}{q} \frac{e^{i\eta' \ln[\frac{1}{2}(1-\cos(\theta))]} }{1 - \cos(\theta)}, \end{aligned} \quad (68)$$

with $\eta' = \frac{m_p}{2q} \alpha'$ and the Coulomb phase shifts $\sigma_l = \arg \Gamma(l+1+i\eta)$. Notice that the amplitude includes an additional phase factor of $e^{-2i\sigma_0}$. The other pp scattering e.m. amplitudes are determined with respect to the V_{C1} interaction in the so-called Coulomb distorted-wave Born approximation (CDWBA) and include the $e^{-2i\sigma_0}$ phase as well.

For f_{C2} , one has to sum over the partial wave contributions to the amplitude

$$f_{C2}(\theta) = \frac{1}{2iq} \sum_{l=0}^{\infty} e^{2i(\sigma_l - \sigma_0)} (e^{2i\rho_l} - 1) P_l(\theta) \quad (69)$$

numerically, employing the corresponding phase-shifts ρ_l given by

$$\rho_l = \sigma_\lambda - \sigma_l + \frac{(l - \lambda)\pi}{2}, \quad (70)$$

with $\lambda = \frac{1}{2}(-1 + \sqrt{(2l+1)^2 - \alpha\alpha'})$. In our calculations, the sum in f_{C2} is performed up to $l = 1000$.

The CDWBA vacuum polarization (VP) amplitude to first order in the VP phase shifts τ_l is derived by Durand [98],

$$\begin{aligned} f_{VP}(\theta) &= \frac{\alpha\eta'}{3\pi q} |\Gamma(1+i\eta')|^2 \int_0^1 \frac{(1+\frac{y}{2})\sqrt{1-y}}{(1-\cos\theta)y+\nu} \\ &\quad \times \left(\frac{2y+\nu}{(1-\cos\theta)y+\nu} \right)^{i\eta'} \\ &\quad \times \exp \left(-2\eta' \arctan \left(\sqrt{\frac{\nu}{2y}} \right) \right) \\ &\quad \times {}_2F_1 \left(-i\eta', 1+i\eta', 1; \frac{y}{y+X} \right) dy, \end{aligned} \quad (71)$$

where $\nu = 2m_e^2/q^2$, $X = \nu/(1-\cos\theta)$ and ${}_2F_1(a, b, c; z)$ is the hypergeometric function. The integral in eq. (71) can be evaluated numerically via quadrature. Analogously, we also evaluate the expressions for the VP phase shifts τ_l numerically.

$$\tau_l = -\frac{a\eta'}{3\pi} \int_0^1 \left(1 + \frac{y}{2}\right) \frac{\sqrt{1-y}}{y} M_l(1+\nu y^{-1}) dy, \quad (72)$$

with

$$\begin{aligned} M_l(1+\nu y^{-1}) &= \frac{1}{2} e^{-\pi\eta'} \left(\frac{2y}{\nu+2y} \right)^{l+1} \\ &\times \left(\frac{\sqrt{\nu}-i\sqrt{2y}}{\sqrt{\nu}+i\sqrt{2y}} \right)^{i\eta'} \frac{|\Gamma(l+1+i\eta')|^2}{\Gamma(2l+2)} \\ &\times {}_2F_1 \left(l+1+i\eta', l+1-i\eta', 2l+2; \frac{2y}{\nu+2y} \right). \end{aligned} \quad (73)$$

The magnetic moment interaction for pp scattering has been derived by Stoks and de Swart [96]. Like in the case of f_{C2} , there exists no simple analytic expression for the scattering amplitude in CDWBA and, instead, the corresponding partial wave S -matrix contributions have to be summed up numerically using eq. (C.5). The authors of ref. [96] have found that M_{10}^1 and M_{01}^1 are not sufficiently converged when the sum is performed up to $j = 1000$ (see footnote⁷), but that the biggest contribution to these amplitudes,

$$Z_{LS} := -\sqrt{2\pi} m_p f_{LS} \sum_{j \text{ even}} e^{2i(\sigma_j - \sigma_0)} \sqrt{\frac{2j-1}{j(j-1)}} Y_{j1}(\theta, 0) \quad (74)$$

for M_{10}^1 and $-Z_{LS}$ for M_{01}^1 , can be summed up analytically leading to

$$Z_{LS} = \frac{m_p f_{LS}}{\sin\theta\sqrt{2}} \left(e^{-i\eta \ln[\frac{1}{2}(1-\cos\theta)]} + e^{-i\eta \ln[\frac{1}{2}(1+\cos\theta)]} - 1 \right). \quad (75)$$

It remains to calculate the nuclear amplitude in accordance to the e.m. amplitude separation. Like in the case

of the np amplitude, the nuclear partial wave S -matrix elements have to be adjusted with the partial wave matrices of the included e.m. interactions.

$$\begin{aligned} (S_{EM+N} - 1) &\rightarrow (S_{C1})^{1/2} (S_{C1+C2}^{C1})^{1/2} (S_{C1+MM}^{C1})^{1/2} \\ &\quad \times (S_{C1+VP}^{C1})^{1/2} (S_{EM+N}^{EM} - 1) \\ &\quad \times (S_{C1+VP}^{C1})^{1/2} (S_{C1+MM}^{C1})^{1/2} \\ &\quad \times (S_{C1+C2}^{C1})^{1/2} (S_{C1})^{1/2}. \end{aligned} \quad (76)$$

Here we follow the notation of [95] and denote with *e.g.* S_{EM+N}^{EM} the partial wave S -matrix of all e.m. interactions plus the nuclear interaction with respect to the e.m. wavefunctions. Analogously, S_{C1+X}^{C1} corresponds to the CDWBA of an arbitrary interaction X . The nuclear phase-shifts, however, are calculated with respect to $C1$ alone, employing the method of Vincent and Phatak [99]. Using these phase-shifts in the construction of the amplitude, *i.e.* $\delta_{EM+N}^{EM} \approx \delta_{C1+N}^{C1}$, is sufficiently accurate except for the 1S_0 partial wave [20]. Here we use the decomposition

$$(\delta_{EM+N}^{EM})_0 = (\delta_{C1+N}^{C1})_0 + \tilde{\Delta}_0 - \rho_0 - \tau_0. \quad (77)$$

The so-called improved Coulomb-Foldy correction $\tilde{\Delta}_0$ has been calculated for the Nijmegen78 potential and tabulated in the range of $E_{\text{lab}} = 0\text{--}30\text{ MeV}$ in ref. [95]. It is argued in that paper that the model-dependence of this quantity is small, and we use the corresponding values from ref. [95] in the given energy range. Above $E_{\text{lab}} = 30\text{ MeV}$, the corrections to δ_{C1+N}^{C1} in eq. (77) are small and can be neglected.

6 Fits to the data

6.1 Parameters of the potential

We are now in the position to specify the values of the nucleon masses and various parameters entering the long-range part of the potentials. For the proton and neutron masses we use the values of $m_p = 938.272\text{ MeV}$ and $m_n = 939.565\text{ MeV}$, respectively. When calculating the relativistic corrections to the NN interaction, the average value of the nucleon mass of $m_N = 2m_p m_n / (m_p + m_n) = 938.918\text{ MeV}$ is adopted. As explained in sect. 4, we take into account isospin-breaking corrections to the OPEP due to the different values of the charged and neutral pion masses, for which the values of $M_{\pi^\pm} = 139.57\text{ MeV}$ and $M_{\pi^0} = 134.98\text{ MeV}$ are employed. In the expressions for the TPEP, we use the pion mass value of $M_\pi = 138.03\text{ MeV}$. Following our recent work [6, 7], we adopt the value of $F_\pi = 92.4\text{ MeV}$ for the pion decay constant. We set the LECs d_{18} , which accounts for the Goldberger-Treiman discrepancy, equal to zero and employ the shifted value of $g_A = 1.29$ for the nucleon axial coupling constant, which is larger than the experimental one of $g_A \simeq 1.267$. This yields for the pion-nucleon coupling constant $g_{\pi N} = g_A m_N / F_\pi$ the value of

⁷ We have verified that this is indeed the case.

Table 1. Values of the πN LECs c_i , \bar{d}_i and \bar{e}_i in units of GeV^{-1} , GeV^{-2} and GeV^{-3} , respectively, used in the semilocal momentum-space regularized potentials of this work (set 1). Values given in set 2 were employed in the potentials of refs. [6,7] and are used in the error analysis to assess the sensitivity of our results to the πN LECs as discussed in sect. 7.5.3.

	set 1			set 2		
	N ² LO	N ³ LO	N ⁴ LO	N ² LO	N ³ LO	N ⁴ LO
c_1	-0.74	-1.07	-1.10	-0.81	-0.81	-0.75
c_2	—	3.20	3.57	—	3.28	3.49
c_3	-3.61	-5.32	-5.54	-4.69	-4.69	-4.77
c_4	2.44	3.56	4.17	3.40	3.40	3.34
$\bar{d}_1 + \bar{d}_2$	—	1.04	6.18	—	3.06	6.21
\bar{d}_3	—	-0.48	-8.91	—	-3.27	-6.83
\bar{d}_5	—	0.14	0.86	—	0.45	0.78
$\bar{d}_{14} - \bar{d}_{15}$	—	-1.90	-12.18	—	-5.65	-12.02
\bar{e}_{14}	—	—	1.18	—	—	1.52
\bar{e}_{17}	—	—	-0.18	—	—	-0.37

$g_{\pi N}^2/(4\pi) = 13.67$, which is consistent with the recent determination based on the Goldberger-Miyazawa-Oehme sum rule $g_{\pi N}^2/(4\pi) = 13.69 \pm 0.20$ [100, 101].

For the pion-nucleon LECs, we employ the central values from ref. [88], obtained by matching the solution of the Roy-Steiner equations to chiral perturbation theory at the subthreshold point as specified in table 1 (set 1). Notice that this paper also quotes uncertainties related to the accuracy of the subthreshold parameters which, however, turn out to be rather small.

To estimate the sensitivity of our results to the values of the πN LECs, we will also perform calculations using the values from set 2, which were employed in our recent studies [6, 7], see sect. 7.5.3 for more details. The LECs c_1 , c_3 and c_4 from set 2 used at N²LO and N³LO and listed in the fifth and sixth columns of table 1, respectively, correspond to the central values of the determination of ref. [102] from πN scattering inside the Mandelstam triangle. The LEC c_2 could not be reliably extracted in that analysis, and the quoted value of $c_2 = 3.28 \text{ GeV}^{-1}$ is taken from the order Q^3 calculation of πN scattering of ref. [103] in the framework of heavy-baryon chiral perturbation theory (in the physical region). Also the values of the LECs d_i used at N³LO and listed in the sixth column of table 1 are taken from fit 1 of that paper. Finally, the values of the LECs used at N⁴LO and given in the last column of table 1 correspond to the order- Q^4 extraction of ref. [68] based on the Karlsruhe-Helsinki partial wave analysis of πN scattering [104]. We emphasize once again that the πN LECs from set 2 are only used in the uncertainty estimations, while all our results are obtained with the LECs from the Roy-Steiner equation analysis (set 1). We refer the reader to refs. [105–107] for review articles on the applications of chiral perturbation theory in the single-nucleon sector.

Finally, for the cutoff Λ , we consider in this study the values in the range of $\Lambda = 350\text{--}550 \text{ MeV}$, namely $\Lambda = 350$, 400, 450, 500 and 550 MeV. As will be shown in sect. 7.3, choosing $\Lambda = 350 \text{ MeV}$ already leads to large regulator

artefacts in the description of NN scattering, and for this reason we do not consider lower values of Λ . On the other hand, increasing Λ beyond the highest considered value of $\Lambda = 550 \text{ MeV}$ leads to highly nonperturbative potentials, see the discussion in sect. 7.4, and eventually to the emergence of spurious deeply bound states signaling that one enters the highly nonlinear regime, in which the arguments based on naive dimensional analysis and assumed in our study become invalid. Notice further that the cut-off $\Lambda = 550 \text{ MeV}$ in the local regulator $\exp(-q^2/\Lambda^2)$ corresponds to the distance of $R = 2\Lambda^{-1} \simeq 0.7 \text{ fm}$, which is close to the breakdown distance of the chiral expansion for the multi-pion exchange potential estimated in ref. [13]. We also emphasize that strongly nonperturbative NN potentials featuring spurious deeply bound states are of little use for *ab initio* few- and many-body calculations.

6.2 Database

For experimental data, we use the SAID database [108] containing elastic NN scattering data from 1950 up to 2008. The data are divided into different experiments, which consist of individual measurements taken either at a fixed beam energy and different angles (angle-dependent observables) or at different energies (total cross sections or observables measured at a fixed angle).

Not all data are mutually compatible, and the exclusion of outliers is important in order to obtain good fits. We, therefore, restrict the database to the mutually compatible data listed in [109], which is also referred to as the 2013 Granada database. The only data set from the 2013 Granada database not included in our analysis is that from ref. [110], which should be updated by more accurate data from an improved version of the experiment carried out by the same group [111]. The database was obtained by iteratively fitting all scattering data in the range of $E_{\text{lab}} = 0\text{--}350 \text{ MeV}$ to a delta-shell potential (and including the one-pion exchange and electromagnetic potentials for the long-range part of the interaction) and

then rejecting those experimental data whose χ^2 -residuals lay outside of the 99.46% confidence interval of the χ^2 -distribution. This data-selection procedure is also known as 3σ -criterion. The self-consistency of the selected data was verified in a subsequent publication [112].

In our analysis, the values of χ^2 are calculated up to the maximum energy of $E_{\text{lab}} = 300$ MeV. The resulting database, restricted to the energy range of $E_{\text{lab}} = 0 - 300$, consists of 2697 np and 2158 pp experimental data. Notice that the actual number of experimental data used in a fit depends on the energy range which is chosen differently from order to order, see sect. 6.3 for more details.

6.3 Fitting procedure

Our fitting procedure is divided into two steps: first, we fit phase shifts and mixing angles to the Nijmegen PWA [20] in the same way as it was done for the EKM potentials of ref. [6, 7]. The resulting LECs then serve as a starting point for the second step, in which the optimization with respect to scattering data is performed. The fit to phase shifts allows us to decompose the parameter space of the LECs accompanying the contact interactions into smaller subspaces, since each LEC enters only one partial wave. Thus, fits can be performed on the partial wave basis. This remains true if the contact potential is regularized according to eq. (2). In this way we avoid the need to perform much more costly searches in the whole parameter space including parameter values far away from the physical minimum. The fitting procedure for the phase shifts is described in detail in ref. [6]. However, the removal of the redundant contact interactions renders the additional constraints on the approximate Wigner $SU(4)$ symmetry and the deuteron D-state probability employed in ref. [6] obsolete since we do not observe any ambiguities in the 3S_1 - 3D_1 channel without them.

Having determined the initial LECs from phase shifts, we refine them in a direct fit to scattering data. The comparison between experimental and calculated scattering observables is done via a standard χ^2 measure whose value is minimized during the fit. We employ the same definition of χ^2 as used in ref. [20, 44, 95, 109, 113]. For the sake of completeness, we provide below the definition of the χ^2 function.

The experimental data are grouped in experiments as discussed in sect. 6.2. The total χ^2 is the sum over all experiments and the contribution of the j -th experiment χ_j^2 comprising n_j measured observable values is defined as [20]

$$\chi_j^2 = \sum_{i=1}^{n_j} \left(\frac{O_i^{\text{exp}} - Z O_i^{\text{theo}}}{\delta O_i} \right)^2 + \left(\frac{Z - 1}{\delta_{\text{norm}}} \right)^2, \quad (78)$$

where O_i^{exp} is the measured value of the observable, O_i^{theo} is its calculated value while δO_i is the (statistical) error. Furthermore, δ_{norm} is the normalization error of the data set and Z is the inverse of the estimated normalization. The contribution of the term $\chi_{\text{norm}}^2 = (Z - 1)^2 \delta_{\text{norm}}^{-2}$ in

eq. (78) can be thought of as an additional data point for the overall normalization. In the case of absolute data ($\delta_{\text{norm}} = 0$), we have $Z = 1$ and $\chi_{\text{norm}}^2 = 0$. For experiments which give a normalization error $\delta_{\text{norm}} \neq 0$, the inverse normalization estimator Z is calculated as

$$Z = \left(\sum_{i=1}^n \frac{O_i^{\text{exp}} O_i^{\text{theo}}}{\delta O_i^2} + \frac{1}{\delta_{\text{norm}}^2} \right) \left(\sum_{i=1}^n \frac{(O_i^{\text{theo}})^2}{\delta O_i^2} + \frac{1}{\delta_{\text{norm}}^2} \right)^{-1}, \quad (79)$$

which minimizes χ_j^2 with respect to Z . In this way, all χ_j^2 become independent of the norms Z and only the LECs entering the NN potential have to be treated as free parameters in the fit. Some experiments allow the normalization of the data to float thus providing relative data which have essentially $\delta_{\text{norm}} = \infty$. Further, if data with $\delta_{\text{norm}} < \infty$ yield $\chi_{\text{norm}}^2 > 9$, the estimated normalization is deemed incompatible with the given normalization error δ_{norm} and these data are also treated as floating (i.e. we calculate Z and χ_j^2 with $\delta_{\text{norm}} = \infty$). This corresponds to the application of the 3σ -criterion to the norm Z as a single data point.

One note is in order regarding the χ^2 /datum values. We again follow the convention of refs. [20, 114] and divide χ^2 by the total number of data $N = N_{\text{exp}} + N_{\text{norm}}$, which consists of the number of measurements N_{exp} and the number of estimated normalizations N_{norm} for all experiments which have not been floated.

The χ^2 -function defined above gets minimized in a simultaneous fit to both neutron-proton and proton-proton scattering data and, therefore, all NN contact LECs are varied at once with the exception of the isospin-breaking \tilde{C}_{1S0}^{nn} contact interaction in the 1S_0 phase, whose determination requires neutron-neutron scattering data. Its value is fixed afterwards from a fit to the neutron-neutron scattering length, for which the value of $a_{1S0}^{nn} = -18.90$ fm from ref. [115] is taken. Notice, however, that this scattering length is not well known experimentally, and the results from different extractions and experiments yield different values.

The energy range of included scattering data is chosen differently at different chiral orders. Starting from $N^4\text{LO}$, we found that setting the maximum fitting energy $E_{\text{lab}}^{\text{max}} \sim 250$ MeV leads to stable results for the LECs and phase shifts for all employed cutoff values in the range of $\Lambda = 350$ – 550 MeV. Given the abundance of np spin-observables available at the energies around $E_{\text{lab}} \sim 260$ MeV and coming from the recent experiments of [116–118], we decided to set $E_{\text{lab}}^{\text{max}} = 260$ MeV at this chiral order. We will address the sensitivity of our results on the choice of $E_{\text{lab}}^{\text{max}}$ in sect. 7.5. At $N^3\text{LO}$, we fit up to $E_{\text{lab}} = 200$ MeV while the maximum energy of included scattering data at LO, NLO and $N^2\text{LO}$ is chosen to be $E_{\text{lab}} = 25, 100$ and 125 MeV. Similar energy ranges were used in the fits of the EKM potentials in refs. [6, 7].

In addition to the scattering data, we also include the deuteron binding energy $B_d = 2.224575(9)$ MeV [119] and the world average for the np coherent scattering length $b_{\text{np}} = -3.7405(9)$ fm [120] to additionally stabilize our fits starting from $N^3\text{LO}$. Tuning these two observables to

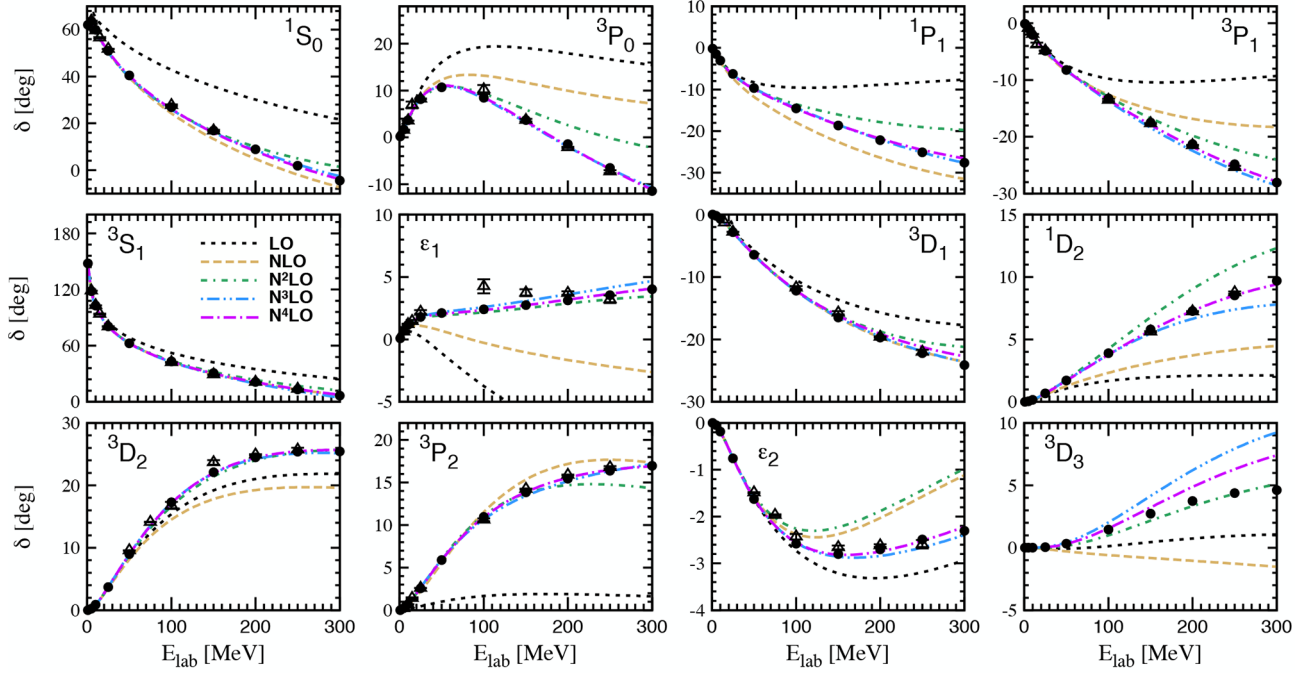


Fig. 8. (Color online) Chiral expansion of the np phase shifts in comparison with the Nijmegen [20] (solid dots) and the GWU [122] (open triangles) np partial wave analysis. Black dotted, orange dashed, green short-dash-dotted, blue dash-double-dotted and violet long-dash-dotted lines show the results at LO, NLO, N^2 LO, N^3 LO and N^4 LO, respectively, calculated using the cutoff $\Lambda = 450$ MeV. Only those partial waves are shown which involve contact interactions at N^4 LO.

their experimental values by simply adding the two corresponding data points to the χ^2 does, however, significantly affect the conditioning and thus worsens the convergence of the fits. Instead of following this path, we use routines for constrained optimization and set the deuteron binding energy and the np coherent scattering length to their central values as explicit constraints while maintaining a fast convergence towards the minimum. Specifically, we use the Interior Point OPTimizer (IPOPT) [121] in our fits, which allows us to incorporate the above mentioned constraints and second-derivative information.

Finally, we comment on the fitting procedures at lower orders, namely at LO, NLO and N^2 LO. While we consider the potentials starting from N^3 LO accurate enough to perform a reliable estimation of the relative norms Z throughout the whole energy range, we allow neither for an estimation of Z nor for floating data sets in case of a too high value of χ^2_{norm} based on those lower-order potentials. Instead, we use this information from the highest order fit at the given cutoff value and keep the normalizations unchanged during the fit. We also do not include the deuteron binding energy and the np coherent scattering length in the fits at these chiral orders.

7 Results for the semilocal momentum-space regularized potentials

In the following sections, we provide a detailed description of our results for the new family of semilocal momentum-space regularized chiral potentials.

7.1 Convergence of the chiral expansion

Having specified the fitting procedure, we are now in the position to present our results. In fig. 8, we show the resulting np phase shifts and mixing angles in the fitted channels, namely in the S-, P- and D-waves and the mixing angles ϵ_1 and ϵ_2 , in comparison with the Nijmegen multi-energy [20] and the GWU single-energy [122] partial wave analyses, see also ref. [123] for a most recent version of the partial wave analysis by the GWU group. While we restrict ourselves to the case of the intermediate cutoff of $\Lambda = 450$ MeV throughout this section, the results for other cutoff values are qualitatively similar. Notice further that the P- and D-wave phase shifts and the mixing angles ϵ_1 and ϵ_2 (the D-wave phase shifts and the mixing angle ϵ_2) are predicted in a parameter-free way at LO (up to N^2 LO). As expected, our results are similar to the ones of refs. [6, 7], where a coordinate-space version of the local regulator was employed and the fits were performed to the NPWA. In most of the channels shown, one observes a good convergence of the chiral expansion with the results showing little changes between N^3 LO and N^4 LO.

The situation is, however, different for F-waves where the results are still not converged at the level of N^4 LO as shown in fig. 9. Here, the differences between the N^3 LO and N^4 LO predictions are clearly visible, and the empirical phase shifts are still not reproduced at N^4 LO. To further elaborate on this issue, we performed fits based on the N^4 LO chiral potential and including the leading F-wave contact interactions which appear at N^5 LO and are given in eq. (17). Here and in what follows, the resulting

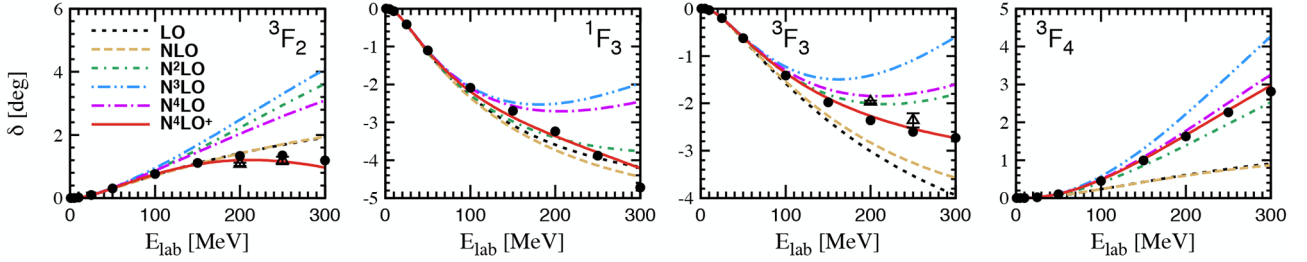


Fig. 9. (Color online) Chiral expansion of the np F-wave phase shifts in comparison with the Nijmegen [20] (solid dots) and the GWU [122] (open triangles) np partial wave analysis. Black dotted, orange dashed, green short-dash-dotted, blue dash-double-dotted, violet long-dash-dotted and red solid lines show the results at LO, NLO, N²LO, N³LO, N⁴LO and N⁴LO⁺, respectively, calculated using the cutoff $\Lambda = 450$ MeV.

partial N⁵LO potential is referred to as N⁴LO⁺. As will be discussed in sect. 7.2, the resulting N⁵LO contact interactions appear to be of a natural size. The difference between the N⁴LO and N⁴LO⁺ results can thus be regarded as a lower bound of the N⁴LO theoretical uncertainty. In the resonance-saturation picture, it can be traced back to the short-range contributions due to heavy-meson exchanges which are not accounted for at the level of N⁴LO. The fact that the LECs E_i come out of a natural size suggests that the poor convergence pattern for F-waves shown in fig. 9 does not reflect any failure of the chiral EFT. Rather, the ³F₂, ¹F₃ and ³F₃ partial waves simply do not provide a suitable testing ground for the chiral pion exchange potential as originally suggested in ref. [85] due to the large short-range contributions to the corresponding phase shifts at energies $E_{\text{lab}} \gtrsim 150$ MeV. Notice that the impact of short-range operators decreases rapidly with increasing values of the orbital angular momentum and becomes small for G- and higher partial waves. Finally, we emphasize that the inclusion of the leading F-wave contact interactions appears to be necessary in order to describe some of the very precisely measured proton-proton scattering data, see the discussion in sect. 7.3.

7.2 Low-energy constants of the contact interactions

In table 2, we show the extracted values of the LECs at N⁴LO⁺ for all employed cutoff values along with the corresponding statistical uncertainties. We remind the reader that $\tilde{C}_i(\Lambda)$, $C_i(\Lambda)$, $D_i(\Lambda)$ and $E_i(\Lambda)$ are *bare* parameters and thus have to be refitted at every chiral order. As discussed in ref. [6], the natural size of the LECs in the spectroscopic notation can be estimated via

$$\begin{aligned} |\tilde{C}_i| &\sim \frac{4\pi}{F_\pi^2}, & |C_i| &\sim \frac{4\pi}{F_\pi^2 \Lambda_b^2}, \\ |D_i| &\sim \frac{4\pi}{F_\pi^2 \Lambda_b^4}, & |E_i| &\sim \frac{4\pi}{F_\pi^2 \Lambda_b^6}, \end{aligned} \quad (80)$$

with the factor of 4π emerging from the angular integration and Λ_b denoting the breakdown scale of the chiral expansion. Using the estimated value of $\Lambda_b = 600$ MeV proposed in ref. [6] and verified in ref. [124], the natural

size of the LECs is expected to be of the order of

$$|\tilde{C}_i| \sim 0.15, \quad |C_i| \sim 0.4, \quad |D_i| \sim 1.1, \quad |E_i| \sim 3, \quad (81)$$

in units used in table 2. We observe that all values of the LECs at N⁴LO⁺ are of a natural size for the cutoff values in the range of $\Lambda = 450 \dots 550$ MeV. For softer cutoff values and especially for the lowest value of $\Lambda = 350$ MeV, the magnitude of some of the LECs increases considerably. This pattern is expected and points towards significant cutoff artefacts, which effectively lower the breakdown scale Λ_b for too small values of Λ . As already mentioned in the previous section, all F-wave LECs E_i appear to be of a natural size. Notice further that the apparently rather smooth Λ -dependence of the various LECs does not extend to higher cutoff values. In particular, in channels where the dominant short-distance singularity (in the infinite-cutoff limit) of the long-range interaction is attractive, Λ -dependence of the LECs accompanying contact terms has to be discontinuous in order to accommodate for the appearance of deeply bound states without, at the same time, affecting the low-energy behavior of the amplitude. Such a discontinuous behavior of the LECs signals a highly nonperturbative regime, in which naive dimensional analysis and the above-mentioned naturalness estimations are not applicable anymore. The values of Λ at which the first deeply bound states are generated depend on several factors such as the chiral order, the employed form of the regulator and the values of the πN coupling constants. While all LECs at N⁴LO⁺ stay natural for cutoff values $\Lambda \leq 550$ MeV (see footnote⁸), we do observe at N³LO the LEC D_{3S1} becoming unnaturally large for $\Lambda = 550$ MeV. As will be shown in sect. 7.4, this also manifests itself in the appearance of a very large repulsive Weinberg eigenvalue in the ³S₁-³D₁ channel, indicating that the corresponding potential is highly nonperturbative. The larger available cutoff range at N⁴LO as compared to N³LO can presumably be traced back to the more accurate representation of the two-pion exchange potential at this order in the chiral expansion.

⁸ The values of \tilde{C}_i , C_i and D_i at N⁴LO are similar to the ones at N⁴LO⁺ for the same cutoff value, but the differences are, in certain cases, larger than the statistical uncertainties given in table 2.

Table 2. The determined LECs of the NN contact interactions at N^4LO^+ along with the statistical uncertainties (except for \tilde{C}_{1S0}^{mn} which is fixed from the value of the nn scattering length of $a_{nn} = -18.9$ fm). The values of the order- Q^{2n} LECs are given in units of 10^4 GeV^{-2-2n} .

LEC	$\Lambda = 350 \text{ MeV}$	$\Lambda = 400 \text{ MeV}$	$\Lambda = 450 \text{ MeV}$	$\Lambda = 500 \text{ MeV}$	$\Lambda = 550 \text{ MeV}$
Low-energy constants at order Q^0					
\tilde{C}_{1S0}^{pp}	-0.061 ± 0.000	-0.029 ± 0.000	0.012 ± 0.000	0.058 ± 0.000	0.106 ± 0.000
\tilde{C}_{1S0}^{mn}	-0.061	-0.029	0.011	0.058	0.105
\tilde{C}_{1S0}^{np}	-0.067 ± 0.001	-0.031 ± 0.000	0.010 ± 0.000	0.056 ± 0.000	0.103 ± 0.001
\tilde{C}_{3S1}	-0.079 ± 0.002	-0.037 ± 0.002	0.011 ± 0.002	0.067 ± 0.002	0.124 ± 0.002
Low-energy constants at order Q^2					
$C_{1S0}^{pp,mn}$	-0.014 ± 0.008	0.099 ± 0.006	0.133 ± 0.005	0.131 ± 0.003	0.124 ± 0.003
C_{1S0}^{np}	0.074 ± 0.017	0.105 ± 0.014	0.121 ± 0.013	0.119 ± 0.012	0.119 ± 0.012
C_{3P0}	0.040 ± 0.008	0.350 ± 0.006	0.591 ± 0.005	0.756 ± 0.004	0.833 ± 0.004
C_{1P1}	0.570 ± 0.019	0.692 ± 0.015	0.753 ± 0.013	0.794 ± 0.012	0.819 ± 0.012
C_{3P1}	0.705 ± 0.005	0.767 ± 0.004	0.828 ± 0.003	0.856 ± 0.004	0.844 ± 0.004
C_{3S1}	-0.190 ± 0.015	-0.063 ± 0.015	-0.024 ± 0.017	-0.044 ± 0.021	-0.083 ± 0.030
$C_{\epsilon 1}$	0.750 ± 0.022	0.550 ± 0.017	0.410 ± 0.014	0.312 ± 0.011	0.233 ± 0.010
C_{3P2}	-0.119 ± 0.002	0.009 ± 0.001	0.127 ± 0.001	0.224 ± 0.001	0.288 ± 0.001
Low-energy constants at order Q^4					
D_{1S0}	6.531 ± 0.190	4.044 ± 0.155	2.579 ± 0.151	1.722 ± 0.159	1.182 ± 0.178
D_{3P0}	3.161 ± 0.067	1.829 ± 0.055	0.813 ± 0.053	0.010 ± 0.052	-0.626 ± 0.046
D_{1P1}	5.394 ± 0.180	1.475 ± 0.137	-0.055 ± 0.118	-0.733 ± 0.104	-1.091 ± 0.086
D_{3P1}	2.528 ± 0.067	1.110 ± 0.055	0.215 ± 0.053	-0.384 ± 0.050	-0.772 ± 0.043
D_{3S1}	4.670 ± 0.247	3.525 ± 0.187	2.663 ± 0.175	2.344 ± 0.189	2.463 ± 0.243
$D_{\epsilon 1}$	0.286 ± 0.282	-0.345 ± 0.216	-0.329 ± 0.200	-0.271 ± 0.205	-0.184 ± 0.233
D_{3D1}	3.617 ± 0.180	2.171 ± 0.133	1.525 ± 0.119	1.140 ± 0.113	0.903 ± 0.108
D_{1D2}	-0.950 ± 0.016	-0.153 ± 0.010	0.218 ± 0.008	0.377 ± 0.006	0.410 ± 0.006
D_{3D2}	-3.180 ± 0.050	-0.858 ± 0.030	0.186 ± 0.022	0.680 ± 0.018	0.941 ± 0.017
D_{3P2}	-1.402 ± 0.016	-0.683 ± 0.010	-0.449 ± 0.008	-0.386 ± 0.007	-0.373 ± 0.005
$D_{\epsilon 2}$	-0.909 ± 0.014	-0.424 ± 0.009	-0.219 ± 0.007	-0.118 ± 0.006	-0.067 ± 0.006
D_{3D3}	-0.483 ± 0.067	-0.081 ± 0.041	0.140 ± 0.030	0.257 ± 0.025	0.282 ± 0.022
Low-energy constants at order Q^6					
E_{3F2}	2.298 ± 0.254	2.489 ± 0.162	2.290 ± 0.130	2.138 ± 0.119	2.018 ± 0.122
E_{1F3}	-0.637 ± 0.470	1.521 ± 0.327	2.161 ± 0.275	2.347 ± 0.261	2.483 ± 0.286
E_{3F3}	2.926 ± 0.339	1.770 ± 0.218	1.319 ± 0.172	1.022 ± 0.149	0.836 ± 0.138
E_{3F4}	-1.816 ± 0.138	-0.221 ± 0.088	0.278 ± 0.067	0.428 ± 0.056	0.425 ± 0.049

It is instructive to compare the values of the LECs D_i in the 1S_0 , 3S_1 and 3S_1 - 3D_1 channels, which are affected by the short-range UTs defined in eq. (5), with the results of earlier studies. In particular, we find that our choice of the off-shell behavior of the contact interactions specified in eqs. (12), (13) leads to the LECs D_{1S0} , D_{3S1} and $D_{\epsilon 1}$ which are all of a natural size. This is in a strong contrast with the large-in-magnitude values of D_{1S0}^1 , D_{1S0}^2 , D_{3S1}^1 , D_{3S1}^2 , $D_{\epsilon 1}^1$ and $D_{\epsilon 1}^2$ found in ref. [6] at N^3LO^9 . Our findings suggest that these large values appeared as a result of overfitting in the presence of the redundant terms

⁹ The same statement applies to the N^4LO EKM potentials of ref. [7] as well.

as already emphasized in sect. 3 for the case of semilocal coordinate-space regularized potentials introduced in refs. [6, 7]. In sect. 8, we will further elaborate on this point by explicitly demonstrating that our fits to scattering data are, to a very good approximation, independent on the choice of the redundant parameters D_{1S0}^{off} , D_{3S1}^{off} and $D_{\epsilon 1}^{\text{off}}$.

Next, we comment on the statistical uncertainties of the various LECs listed in table 2. First, one observes that the statistical uncertainties of the LECs, taken relative to their expected natural values, tend to increase from \tilde{C}_i to C_i to D_i to E_i . This pattern is consistent with the power counting, which suggests that the contributions of contact

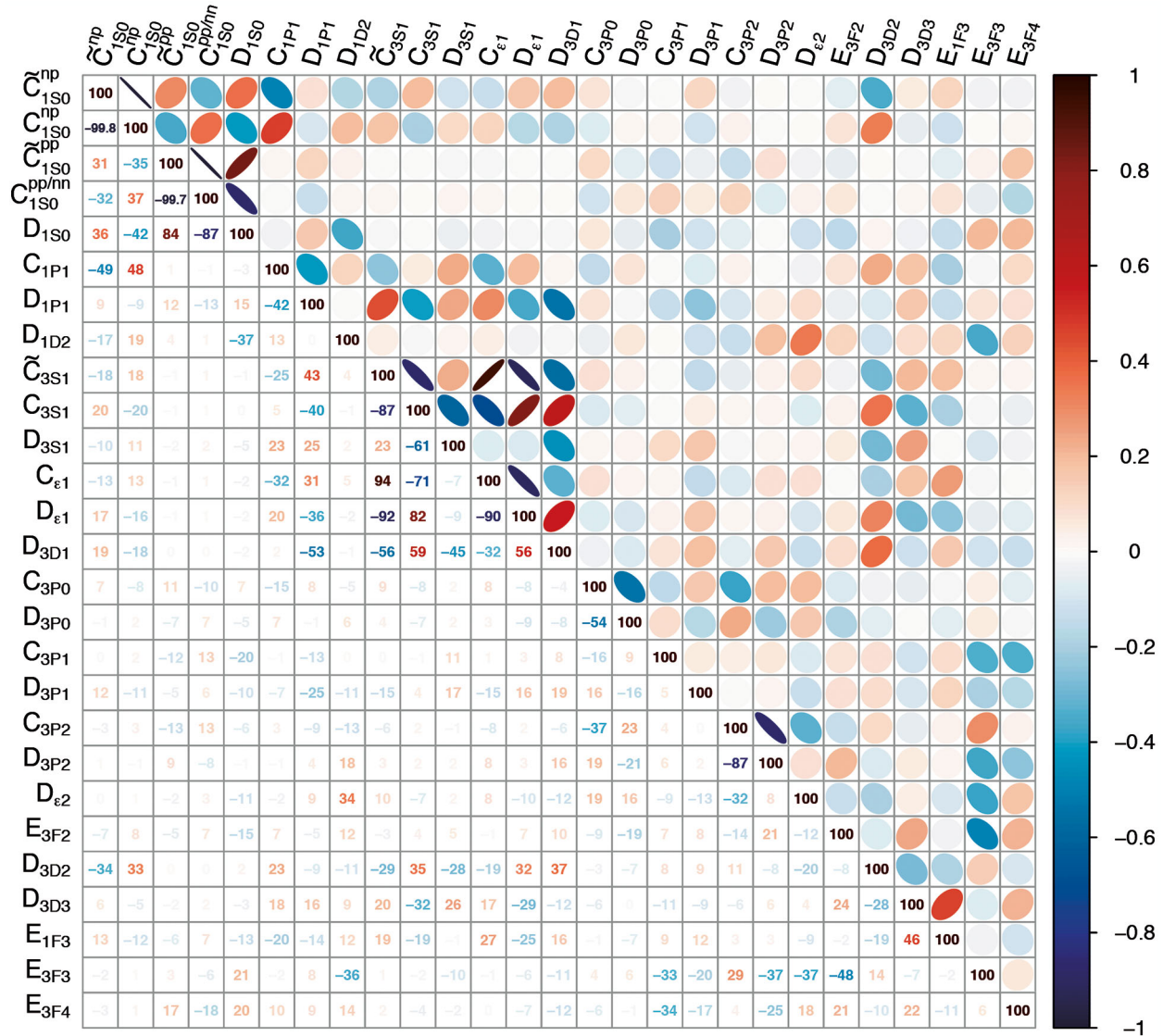


Fig. 10. Correlations between the various LECs for the case of the N^4LO^+ potential with $\Lambda = 450$ MeV. The lower triangle gives the correlation coefficients in percent.

interactions to the scattering amplitude decrease with the chiral order. We also observe considerably smaller statistical uncertainties in the isovector channels as compared to the isoscalar ones, which are extracted from the combined np and pp data and thus benefit from the larger amount of experimental data and the generally higher precision of pp data. Last but not least, the statistical uncertainties tend to increase for soft choices of the regulator as one would expect as a consequence of the less accurate description of the data, which is especially true for the case of $\Lambda = 350$ MeV, see sect. 7.3 for more details, but show little cutoff dependence otherwise.

Finally, we have also looked at the correlations between the various LECs as visualized in fig. 10 for the case of the intermediate cutoff $\Lambda = 450$ MeV. As one may expect, the strongest correlations and/or anti-correlations appear between the LECs in the channels with the largest number of parameters, namely 1S_0 and in 3S_1 - 3D_1 . This is reflected

in the statistical uncertainties of the corresponding LECs being larger than the uncertainties of the LECs C_i and D_i in most of the other channels. Still, in spite of the strong correlations/anticorrelations present, most of the LECs are determined by the scattering data with good accuracy. The large statistical uncertainty for E_{1F3} reflects the fact that the corresponding phase shifts provide only a minor contribution to the NN scattering amplitude in the considered energy range. The impact of the statistical uncertainties of the LECs on the calculated observables in the NN system will be quantified in sect. 7.5.1.

7.3 Description of NN scattering data

We now turn to the description of the scattering data. In table 3, we give the χ^2/datum for the description of the neutron-proton and proton-proton scattering data at

Table 3. χ^2/datum for the description of the neutron-proton and proton-proton scattering data at various orders in the chiral expansion for $\Lambda = 450 \text{ MeV}$. The values in the brackets give the χ^2/datum without including the “outlier” proton-proton scattering data set CO(67) from ref. [127] as described in the text.

E_{lab} bin	LO	NLO	$N^2\text{LO}$	$N^3\text{LO}$	$N^4\text{LO}$	$N^4\text{LO}^+$
neutron-proton scattering data						
0–100	73	2.2	1.2	1.08	1.07	1.08
0–200	62	5.4	1.7	1.10	1.08	1.07
0–300	75	14	4.2	2.01	1.16	1.06
proton-proton scattering data						
0–100	2290	10	2.2	0.90	0.88	0.86
0–200	1770	90	37	1.99 (1.67)	1.42 (1.16)	0.95
0–300	1380	90	41	3.43 (3.23)	1.67 (1.50)	1.00

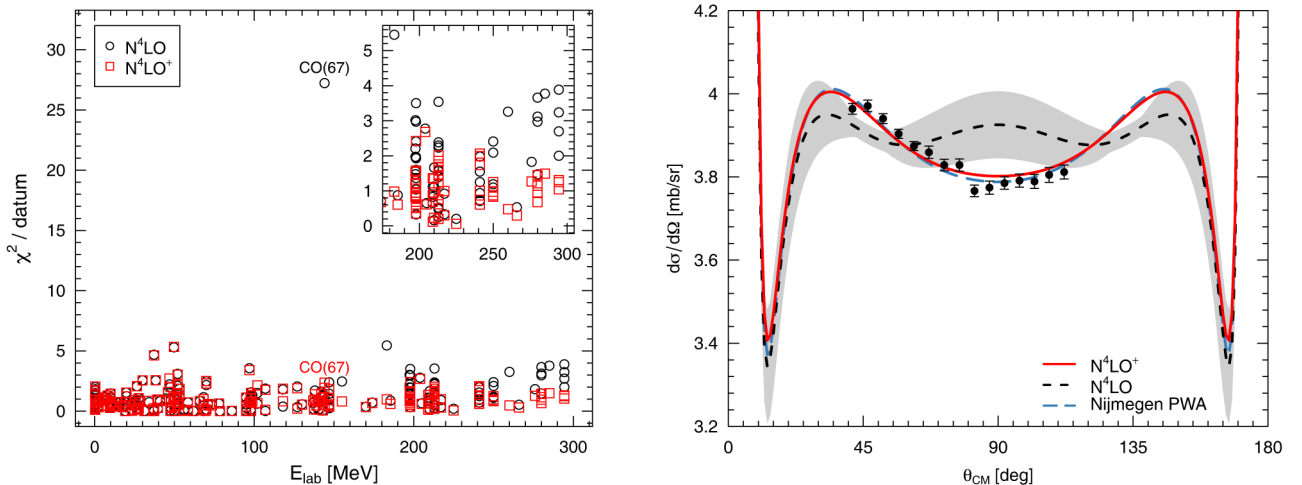


Fig. 11. (Color online) Left panel: contributions of various pp data sets to the χ^2/datum . Open black circles and red squares correspond to the results at $N^4\text{LO}$ and $N^4\text{LO}^+$, respectively. Right panel: pp differential cross section at $E_{\text{lab}} = 144 \text{ MeV}$ as function of the scattering angle calculated at $N^4\text{LO}$ (black short-dashed line) and $N^4\text{LO}^+$ (red solid line) in comparison with the experimental data of the CO(67) data set of ref. [127], which have been divided by the inverse norm of $Z = 1.012$ estimated in the $N^4\text{LO}^+$ fit. The grey shaded band shows the theoretical uncertainty at $N^4\text{LO}$ from the truncation of the chiral expansion estimated using the approach formulated in refs. [6, 7] (without taking into account the information at order $N^4\text{LO}^+$). Long-dashed blue line shows the result of the Nijmegen PWA [20]. In both panels, the chiral potentials correspond to the intermediate cutoff of $\Lambda = 450 \text{ MeV}$.

various chiral orders for the case of the intermediate cut-off $\Lambda = 450 \text{ MeV}$. Our results agree qualitatively with the ones reported in refs. [6, 7], where fits to the Nijmegen PWA have been performed. As expected, the value of χ^2/datum decreases with increasing chiral order. It is particularly comforting to observe a significant improvement in the description of the experimental data at $N^2\text{LO}$ and $N^4\text{LO}$ as compared to NLO and $N^3\text{LO}$, which can be traced back to the corresponding parameter-free contributions to the two-pion exchange potential¹⁰. This provides

¹⁰ At $N^4\text{LO}$, we take into account an additional isospin-breaking contact interaction in the 1S_0 channel as compared to $N^3\text{LO}$, which gives the difference between $C_{1S0}^{\text{pp},\text{nn}}$ and C_{1S0}^{np} , see ref. [7] for more details.

a clear evidence of the chiral two-pion exchange, a feature which was already reported in refs. [6, 7] based on the Nijmegen PWA, see also refs. [125, 126] for related earlier studies.

While the description of the np scattering data up to $E_{\text{lab}} = 200 \text{ MeV}$ and pp data up to $E_{\text{lab}} = 100 \text{ MeV}$ is found to be very good starting from $N^3\text{LO}$, the χ^2/datum is significantly larger than 1 for pp data at intermediate energy. To better understand the origin of this behavior, we show in the left panel of fig. 11 the contributions of the individual data sets to the χ^2 . One observes that the large value of the χ^2/datum for the energy bin of $E_{\text{lab}} = 0 \dots 200 \text{ MeV}$ at $N^4\text{LO}$ is, to a considerable extent, caused by the CO(67) [127] set of differential cross sections, which generates a large contribution of

Table 4. χ^2/datum for the description of the neutron-proton and proton-proton scattering data at $N^4\text{LO}^+$ for all considered cutoff values.

E_{lab} bin	$\Lambda = 350 \text{ MeV}$	$\Lambda = 400 \text{ MeV}$	$\Lambda = 450 \text{ MeV}$	$\Lambda = 500 \text{ MeV}$	$\Lambda = 550 \text{ MeV}$
neutron-proton scattering data					
0–100	1.13	1.08	1.08	1.07	1.07
0–200	1.17	1.07	1.07	1.07	1.07
0–300	1.84	1.17	1.06	1.06	1.07
proton-proton scattering data					
0–100	0.98	0.88	0.86	0.86	0.87
0–200	1.10	0.96	0.95	0.96	0.99
0–300	1.30	1.02	1.00	1.04	1.11

$[\chi^2/\text{datum}]_{\text{CO}(67)} = 27.88$. This can be traced back to the very high precision of these experimental data, which exceeds substantially the accuracy of our $N^4\text{LO}$ results. We emphasize that this does not indicate any failure of the chiral EFT: indeed, as shown in the right panel of fig. 11, the CO(67) experimental data are actually fairly well described at $N^4\text{LO}$ if one takes into account the theoretical uncertainties at this order estimated using the approach of ref. [6] (see footnote¹¹). Still, the shape of the CO(67) cross section data is not properly described at $N^4\text{LO}$, see also ref. [128] for a related discussion. We found that this can be traced back to the still poor description of F-waves at $N^4\text{LO}$ as visualized in fig. 9. To further elaborate on this point, we have redone the $N^4\text{LO}$ fits including the leading contact interactions in the F-waves defined in eq. (17). With 4 additional parameters, we indeed observe that the shape of the cross section data is well described, see the right panel of fig. 11. We also show in the left panel of fig. 11 that the χ^2/datum for the description of pp data at higher energies decreases significantly upon including these contact interactions in F-waves. We are then able to achieve a nearly perfect description of the np and pp scattering data up to $E_{\text{lab}} = 300 \text{ MeV}$ as shown in the last column of table 3. We refer to the resulting potentials as $N^4\text{LO}^+$ and expect them to be particularly useful for a reliable quantification of the theoretical uncertainties at $N^4\text{LO}$. They also allow for a more precise extraction of the LECs \tilde{C}_i , C_i and D_i at $N^4\text{LO}$.

Finally, in table 4, we show the values of the χ^2/datum for the description of the np and pp scattering data at $N^4\text{LO}^+$ for all considered cutoff values. As expected, the softest version of the potential with $\Lambda = 350 \text{ MeV}$ leads to significant cutoff artefacts, which manifest themselves in the rather large values of the χ^2/datum at higher energies. The description of the data improves with increasing the cutoff Λ and reaches its optimum for $\Lambda = 450 \text{ MeV}$. No improvement is observed when increasing the cutoff Λ beyond this value. A similar picture emerges at lower orders in the chiral expansion. This pattern is qualitatively

similar to the one observed for the coordinate-space regularized potentials of refs. [6, 7].

7.4 Weinberg eigenvalue analysis

To assess perturbativeness of the new SMS potentials we have performed a Weinberg eigenvalue analysis as outlined in sect. 3. In figs. 12 and 13, we show the magnitude of the largest repulsive and attractive eigenvalues as function of the cms energy at all orders and for all considered cutoff values. In most cases, the largest in magnitude eigenvalues are given by the trajectory of a single eigenvalue as function of the energy. In a few exceptions, however, the trajectories corresponding to the two largest in magnitude eigenvalues cross each other within the considered energy range. In such cases, we show the part of the eigenvalue trajectory corresponding to the second-largest in magnitude eigenvalue by open symbols connected with dotted lines. The remaining kinks do not reflect any discontinuous behavior and emerge when the corresponding eigenvalues change primarily in the radial direction in the complex plane when increasing the energy E_{cms} .

As expected, one observes a clear tendency towards increasingly nonperturbative potentials for larger cutoff values. Except for the ${}^3\text{S}_1$ - ${}^3\text{D}_1$ channel, all potentials are perturbative in the considered energy range for the cutoff values of $\Lambda = 350 \dots 450 \text{ MeV}$. In this perturbative regime, the eigenvalues do change strongly at lower orders but appear to reach convergence starting from $N^3\text{LO}$. The only exception is the ${}^3\text{P}_2$ - ${}^3\text{F}_2$ channel, where the repulsive eigenvalues are driven by the leading contact interaction first taken into account at $N^4\text{LO}^+$. The largest repulsive eigenvalues increase significantly in S- and P-waves at NLO and $N^2\text{LO}$ and in S-waves at $N^3\text{LO}$ starting from the cutoff $\Lambda = 500 \text{ MeV}$, but the corresponding potentials still remain perturbative in most cases. This trend becomes much more pronounced for the largest considered cutoff value of $\Lambda = 550 \text{ MeV}$. Here, by far the largest in magnitude repulsive eigenvalue emerges at $N^3\text{LO}$ in the ${}^3\text{S}_1$ - ${}^3\text{D}_1$ channel, and the corresponding potential is strongly non-perturbative. This pattern is presumably related to the unnaturally large value of the order- Q^4 LEC D_{3S1} we find in this case, namely $D_{3S1} = 22.7 \times 10^4 \text{ GeV}^{-6}$. Notice

¹¹ Notice that the leftmost point at $\theta_{\text{CM}} = 41.4^\circ$ is declared as an outlier in the SAID database and is, therefore, not included in the fits.

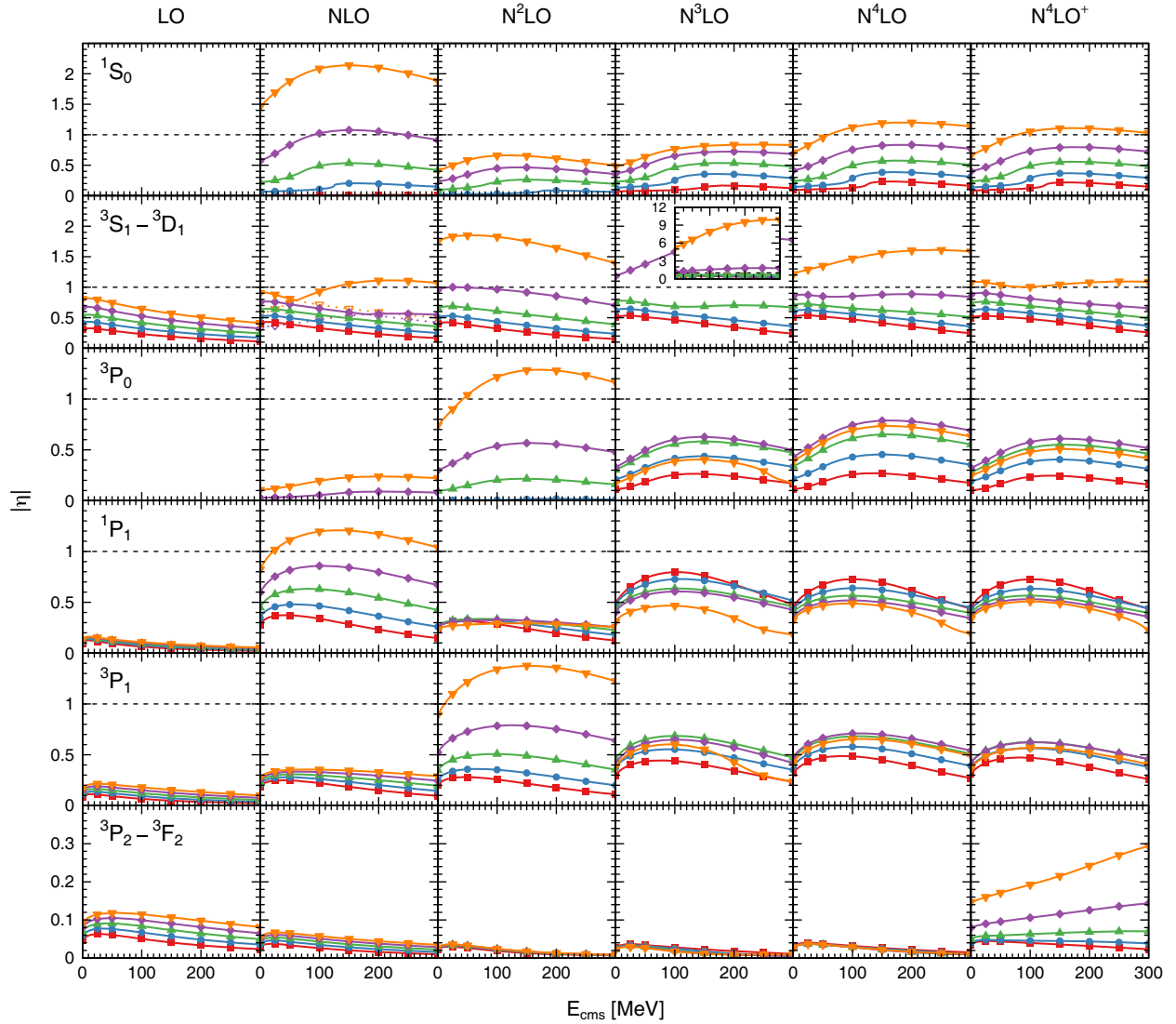


Fig. 12. (Color online) The magnitude of the largest repulsive Weinberg eigenvalues $|\eta|$ in the ${}^1\text{S}_0$, ${}^3\text{S}_1 - {}^3\text{D}_1$, ${}^3\text{P}_0$, ${}^1\text{P}_1$, ${}^3\text{P}_1$ and ${}^3\text{P}_2 - {}^3\text{F}_2$ channels at different orders in the chiral expansion. Red squares, blue dots, green up triangles, violet diamonds and orange down triangles correspond to $\Lambda = 350, 400, 450, 500$ and 550 MeV, respectively.

that this is the only case we observe an unnaturally large LEC. Interestingly, the potentials at N^4LO and N^4LO^+ are considerably more perturbative for the largest considered cutoff value than that at N^3LO .

7.5 Error analysis

We now turn to the discussion of the various sources of uncertainties of our calculations. Specifically, we address below the statistical uncertainty, truncation error of the chiral expansion, uncertainties in the pion-nucleon LECs c_i , \bar{d}_i and \bar{e}_i as well as the uncertainty associated with the choice of the energy range in the fits. We emphasize that the discussed uncertainties are not completely independent of each other. For this reason we refrain from combining them into a single theoretical error and prefer

to specify them separately when giving results for observables.

7.5.1 Statistical uncertainty

We begin with the discussion of the statistical uncertainty of the LECs accompanying NN contact interactions, which we collectively denote as c . In the context of parameters estimation, the statistical errors of the LECs quantify the accuracy of their determination by the scattering data used in the fit. For the case at hand, we regard the χ^2 -function as a measure of the goodness of the fits with the optimal values of LECs $c = c_{\min}$ corresponding to the minimum of χ^2 . The statistical uncertainty of the determined LECs can be naturally assessed via corresponding variations of χ^2 . Specifically, we define the uncertainty of the LECs to comprise all values c compatible with the maximum

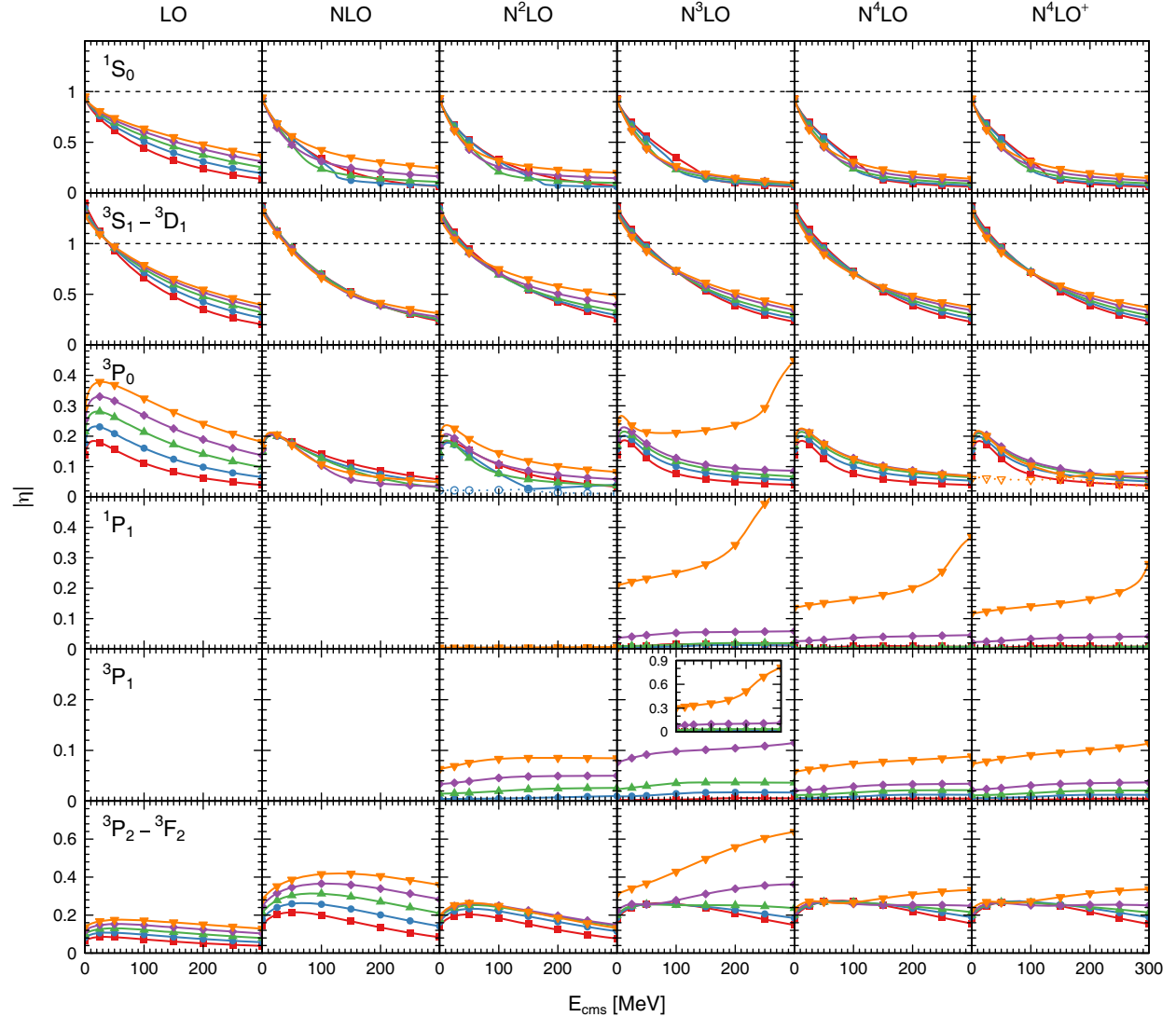


Fig. 13. (Color online) The magnitude of the largest attractive Weinberg eigenvalues $|\eta|$ in the 1S_0 , $^3S_1 - ^3D_1$, 3P_0 , 1P_1 , 3P_1 and $^3P_2 - ^3F_2$ channels at different orders in the chiral expansion. For notation see fig. 12.

allowed variation T of χ^2

$$\chi^2(c) \leq \chi^2(c_{\min}) + T. \quad (82)$$

Different choices of T lead to different confidence levels for the obtained parameter uncertainties. While the exact connection between T and the confidence level is not immediately clear in a most general case, we can be guided by the more specific situation described below, which can often be regarded as a good approximation. Namely, for the case of normally distributed residuals, which are further assumed to be approximately linear functions of the parameters in the vicinity of the minimum, the increase of χ^2 can be related to a confidence level via the χ^2 distribution. For the uncertainty of a single parameter, *i.e.* while other parameters are allowed to vary, $T = 1$ leads to a 1σ or 68% confidence level. Under the aforementioned assumptions, one would also expect χ^2_{\min} to follow the χ^2

distribution with $N_{\text{dof}} = N_{\text{exp}} - N_{\text{float}} - N_c$ degrees of freedom, where N_{exp} is the number of experimental data (not including the norms), N_{float} is the number of floated data while N_c is the number of LECs entering the fit. For a proper description of the data, χ^2_{\min} is expected to have the value of $N_{\text{dof}} \pm \sqrt{2N_{\text{dof}}}$. However, in practice, one often finds higher values of χ^2_{\min} . To account for this situation, we follow a commonly used approach, see *e.g.* ref. [10], and normalize the residuals with the Birge factor [129] according to $\chi^2 \rightarrow \chi^2 N_{\text{dof}} / \chi^2_{\min}$, so that the expectation value $\chi^2_{\min} = N_{\text{dof}}$ is trivially fulfilled. We then get $T = \chi^2_{\min} / N_{\text{dof}}$, which increases the uncertainties to account for the non-optimal description of the data.

While it is certainly important to quantify the uncertainty of the LECs, our main goal is to estimate the statistical errors of the calculated observables. In a complete analogy with the above considerations for the LECs, the

uncertainty regions δO_{\pm} for an observable of interest O are defined in terms of the allowed maximum variation of the χ^2 -function as

$$\begin{aligned}\delta O_- &= -\min [O(c) - O(c_{\min})], \\ \delta O_+ &= \max [O(c) - O(c_{\min})],\end{aligned}\quad (83)$$

subject to the constraint in eq. (82), see also ref. [130] for a similar approach. For the sake of generality, we have separately defined the lower and upper errors δO_- and δO_+ , which, of course, coincide if the underlying probability distribution is symmetric as it is *e.g.* the case for normally distributed observables. This definition can also be straightforwardly extended to include other constraints in addition to eq. (82). For the case at hand, the allowed variation of the LECs c is further restricted to exactly reproduce the deuteron binding energy and the np coherent scattering length starting from N³LO. In our analysis, we have directly implemented eq. (83) as a constrained optimization problem and applied it to calculate the statistical uncertainty for selected observables. Notice that in such an optimization procedure, which explores variations of χ^2 away from the optimal solution, the set of data sets with floated norm must be fixed according to its determination at the χ^2 minimum. While it, by itself, makes little sense to apply the decision criterion for floating the data based on a non-optimal solution, additional floating would also introduce discontinuities in the χ^2 hypersurface and can lead to χ^2 values lower than the previously determined minimum, a feature we certainly want to avoid in our error analysis.

While the approach for estimating the statistical uncertainty outlined above is quite general, it requires performing additional fits for every quantity of interest. Consequently, it is usually too expensive to be employed in practical calculations, especially when carrying out error analysis beyond the two-nucleon system. We will, therefore, use a more convenient approach to propagating the statistical uncertainties based on the covariance matrix throughout our analysis except for the few cases, where this approach is expected to be inaccurate and where we will resort to the general method described at the beginning of this section. This also allows us to easily assess the amount of linear correlations between the LECs. We emphasize that many of the results discussed below are, strictly speaking, only valid for model functions (in our case observables), which depend linearly on the parameters. For nonlinear fits like the ones we perform, several assumptions have to be made. First, we assume that the χ^2 function can be approximated around the minimum $c = c_{\min}$ via

$$\chi^2(c) \approx \chi^2_{\min} + \frac{1}{2}(c - c_{\min})^T H(c - c_{\min}), \quad (84)$$

where c is the vector of the LECs while H denotes the Hessian of χ^2 at the minimum, *i.e.* $H_{ij} = \frac{\partial^2 \chi^2}{\partial c_i \partial c_j}|_{c=c_{\min}}$. The parameters c are assumed to follow a multivariate

Gaussian probability distribution

$$\begin{aligned}p(c, c_{\min}, \Sigma) &= \frac{1}{\sqrt{(2\pi)^n \det(\Sigma)}} \\ &\times \exp \left[-\frac{1}{2} (c - c_{\min})^T \Sigma^{-1} (c - c_{\min}) \right]\end{aligned}\quad (85)$$

in the vicinity of the minimum, where the covariance matrix Σ is given by

$$\Sigma = 2 \frac{\chi^2}{N_{\text{dof}}} H^{-1}. \quad (86)$$

This relation (modulo the χ^2/N_{dof} factor) can be easily obtained by inserting the quadratic approximation (84) into the likelihood function $\mathcal{L} \propto \exp(-\chi^2/2)$ and by matching the resulting expression to eq. (85). The additional factor of χ^2/N_{dof} is related to a rescaling of χ^2 with the Birge factor as discussed above. In our fits, the deuteron binding energy and the value of the coherent np scattering length are adjusted via constrained optimization techniques, which cannot be included in the estimation of the covariance matrix in a straightforward way. Instead, we employ an augmented χ^2 -function, where we have added two quadratic penalty terms for the deuteron binding energy B_d and the np coherent scattering length b_{np}

$$\chi^2_{\text{aug}} = \chi^2_{\text{data}} + \left(\frac{B_d - B_d^{\text{exp}}}{\Delta B_d} \right)^2 + \left(\frac{b_{\text{np}} - b_{\text{np}}^{\text{exp}}}{\Delta b_{\text{np}}} \right)^2, \quad (87)$$

with $\Delta B_d = 5 \times 10^{-5}$ MeV and $\Delta b_{\text{np}} = 9 \times 10^{-4}$ fm. Hence, we have relaxed the constraints to the additional data points. The augmented χ^2 in eq. (87) does not have exactly the same location of the minimum as the χ^2 in the constrained problem, and, consequently, we have to readjust the LECs to be at the minimum of χ^2_{aug} before we can estimate the covariance matrix from its Hessian. The changes in the LECs and observables compared to our constrained fits are very small and well within the statistical uncertainties, but the additional fits of χ^2_{aug} are, nonetheless, rather time-consuming due to the slow convergence as already mentioned in sect. 6.3. The resulting values of the LECs are only used for the calculation of the covariance matrix. The statistical errors $\sigma_i = \sqrt{\Sigma_{ii}}$ and correlation coefficients $\text{Corr}(c_i, c_j) = \Sigma_{ij}/\sqrt{\Sigma_{ii}\Sigma_{jj}}$ of the LECs given in sect. 7.2 are then easily obtained from the covariance matrix.

When calculating observables, propagation of statistical uncertainties can be carried out in a general way by Monte Carlo sampling of the assumed multivariate Gaussian distribution of the LECs in the vicinity of the minimum. We avoid the costly sampling by expanding an observable of interest O in powers of $c - c_{\min}$. While it is common to use just a linear expansion, it was argued in [10] that some observables need to be expanded quadratically in $c - c_{\min}$,

$$O(c) = O(c_{\min}) + J_O(c - c_{\min}) + \frac{1}{2}(c - c_{\min})^T H_O(c - c_{\min}), \quad (88)$$

in order to have an accurate estimation of uncertainties. Here, J_O and H_O denote the corresponding Jacobian and Hessian, respectively. Here and in what follows, we assume the validity of this quadratic approximation. Using eq. (88) it is easy to obtain the mean or expectation value μ of $O(c)$

$$\mu(O) \equiv \langle O \rangle = O + \frac{1}{2} \text{Tr}(H_O \Sigma) \quad (89)$$

as well as its variance

$$\text{Var}(O) \equiv \langle O^2 \rangle - \langle O \rangle^2 = J_O^T \Sigma J_O + \frac{1}{2} \text{Tr}((H_O \Sigma)^2), \quad (90)$$

where $\langle X \rangle$ denotes the expectation value of a random variable X and it was again assumed that the parameters c_i follow the multivariate Gaussian distribution (85) in order to evaluate their moments. We then define the confidence interval for O as $[\mu(O) - \sqrt{\text{Var}(O)}, \mu(O) + \sqrt{\text{Var}(O)}]$. Notice that, due to the second-order term in eq. (89), $\mu(O)$ does not necessarily coincide with $O(c_{\min})$, making the error bars for $O(c_{\min})$ asymmetric. We further emphasize that given that $O(c)$ do not necessarily follow a Gaussian distribution, the interpretation of the quoted statistical uncertainties in terms of confidence intervals should be taken with care.

7.5.2 Truncation error

To estimate the uncertainties from the truncation of the chiral expansion we employ the approach formulated in [6, 7]. Specifically, let $X(p)$ be a NN observable calculated using the chiral nuclear forces in terms of the expansion

$$X^{(\nu)}(p) = \sum_{i=0}^{\nu} a_i Q^i, \quad (91)$$

where p is the characteristic cms momentum scale, Q denotes the expansion parameter of the chiral EFT and a_i are the corresponding coefficients with $a_1 = 0$ in accordance with the vanishing contribution to the nuclear Hamiltonian at that order. Following ref. [6], the expansion parameter Q is defined as

$$Q = \max \left(\frac{M_\pi}{\Lambda_b}, \frac{p}{\Lambda_b} \right), \quad (92)$$

and we use for the breakdown scale Λ_b the value of $\Lambda_b = 600$ MeV as suggested in that paper except for the results in sect. 7.8 and appendix D, where a slightly larger value of $\Lambda_b = 650$ MeV is adopted. Notice that due to the appearance of significant cutoff artefacts for the softest choice of the regulator $\Lambda = 350$ MeV, we do not expect this assignment to provide a realistic estimation of the breakdown scale in that case, see also the related discussions in refs. [6, 131]. Following refs. [6, 7, 25], we use $Q = M_\pi/\Lambda_b$ when estimating the uncertainties of various deuteron properties.

To calculate the expansion coefficients a_i we exploit the knowledge of the available results for $X^{(i)}$ at various chiral orders. Specifically, we build the differences

$$\begin{aligned} \Delta X^{(2)} &= X^{(2)} - X^{(0)}, \\ \Delta X^{(i)} &= X^{(i)} - X^{(i-1)}, \quad i \geq 3, \end{aligned} \quad (93)$$

and identify $a_0 \equiv X^{(0)}$ and $a_i Q^i \equiv \Delta X^{(i)}$ for $i \geq 2$. As the expansion of $X^{(\nu)}$ is assumed to be convergent for $\nu \rightarrow \infty$ and, therefore, the contributions are expected to become smaller at higher orders, it is reasonable to assume the truncation error to be dominated by the first neglected chiral order, *i.e.* we assume that the error scales with $Q^{\nu+1}$. Specifically, we define the truncation error for an observable at chiral order ν to be [6]

$$\begin{aligned} \delta X^{(0)} &= Q^2 |X^{(0)}|, \\ \delta X^{(\nu)} &= \max_{2 \leq i \leq \nu} (Q^{\nu+1} |X^{(0)}|, Q^{\nu+1-i} |\Delta X^{(i)}|), \quad \nu \geq 2, \end{aligned} \quad (94)$$

subject to the additional constraint

$$\delta X^{(\nu)} \geq \max_{i,j} (|X^{(i \geq \nu)} - X^{(j \geq \nu)}|). \quad (95)$$

Notice that the Bayesian analysis of the results of refs. [6, 7] for various NN observables carried out in refs. [124, 131] has revealed that the above algorithm corresponds to a particular form of the prior probability distribution, and that the estimated truncation errors are (on average) consistent with the $\sim 68\% \dots 83\%$ degree-of-belief intervals at NLO...N⁴LO for not too soft cutoff choices. Those studies have also confirmed the estimation of the breakdown scale $\Lambda_b \sim 600$ MeV of refs. [6]. For further discussion of this approach to quantifying the truncation error and of its limitations the reader is referred to ref. [132].

7.5.3 Uncertainty in the πN LECs

Another source of uncertainty is related to the employed values of the πN LECs c_i , \bar{d}_i and \bar{e}_i , which are taken from matching chiral perturbation theory to the recent Roy-Steiner-equation analysis of πN scattering in the subthreshold region [88]. This paper also quotes uncertainties emerging from the known accuracy of the subthreshold coefficients used as input in the determination of the πN LECs, which can, in principle, be propagated when calculating NN observables. Such an error analysis would, however, not reflect the systematic uncertainty in the πN LECs related to the truncation error of the chiral expansion and to the employed method and/or kinematics chosen to determine the LECs. In fact, by far the dominant source of uncertainty in these LECs is known to reside in the chiral expansion of the πN scattering amplitude as reflected by the significant shifts in the LECs extracted at different orders, see table 1. Thus, we follow here a different procedure and estimate the sensitivity of our predictions to the employed values of these parameters by

Table 5. χ^2/datum for the description of the neutron-proton and proton-proton scattering data at $N^4\text{LO}^+$ for $\Lambda = 450 \text{ MeV}$ as a function of the maximum fitting energy E_{lab}^{\max} .

E_{lab} bin	$E_{\text{lab}}^{\max} = 220 \text{ MeV}$	$E_{\text{lab}}^{\max} = 260 \text{ MeV}$	$E_{\text{lab}}^{\max} = 300 \text{ MeV}$
neutron-proton scattering data			
0–100	1.07	1.08	1.08
0–200	1.06	1.07	1.07
0–300	1.10	1.06	1.06
proton-proton scattering data			
0–100	0.86	0.86	0.87
0–200	0.95	0.95	0.96
0–300	1.00	1.00	0.98

calculating NN observables using an alternative set of the πN LECs as specified in table 1 (set 2). This allows us to probe also some of the systematic uncertainties mentioned above since the πN LECs employed at $N^4\text{LO}/N^4\text{LO}^+$ are determined from different kinematical regions of πN scattering, namely from the unphysical region around the sub-threshold point for set 1 and from the physical region for set 2, see sect. 6.1 for more details.

To this aim, we have redone the fits of the NN LECs using the same protocol at all orders starting from $N^2\text{LO}$ and for all cutoff values using the πN LECs from set 2. The resulting description of the data is generally found to be comparable to the one based on the LECs from the Roy-Steiner equation analysis (set 1) as given in tables 3 and 4. More precisely, the πN LECs from set 2 typically yield a better description of the NN data at $N^3\text{LO}$ and $N^4\text{LO}$ (except for low-energy data). On the other hand, the results at $N^4\text{LO}^+$ appear to be somewhat worse than those based on the πN LECs from set 1. For example, for the intermediate cutoff $\Lambda = 450 \text{ MeV}$, we obtain at $N^4\text{LO}^+$ the values of χ^2/datum of 1.10 (0.93), 1.09 (0.98) and 1.09 (1.05) for np (pp) data in the energy ranges of $E_{\text{lab}} = 0$ –100 MeV, $E_{\text{lab}} = 0$ –200 MeV and $E_{\text{lab}} = 0$ –300 MeV, respectively, which have to be compared with the ones for πN LECs from set 1 given in the last column of table 3. The worse description of the low-energy pp data can be traced back to deviations in the ${}^1\text{D}_2$ partial wave. Interestingly, we find that for hard cutoff choices, the potentials based on the πN LECs from set 2 tend to be more perturbative than the ones based on the LECs from the Roy-Steiner equation analysis. This is especially pronounced at $N^3\text{LO}$ for $\Lambda = 550 \text{ MeV}$.

7.5.4 Systematic uncertainty due to the choice of the energy range in the fits

Last but not least, we address the uncertainty related to the choice of the maximum energy when performing fits to NN data. Here and in what follows, we restrict ourselves to the highest chiral order and thus consider only $N^4\text{LO}^+$ potentials. As will be shown in the following sections, the resulting uncertainty typically appears to be small compared with the other error sources. When lowering the

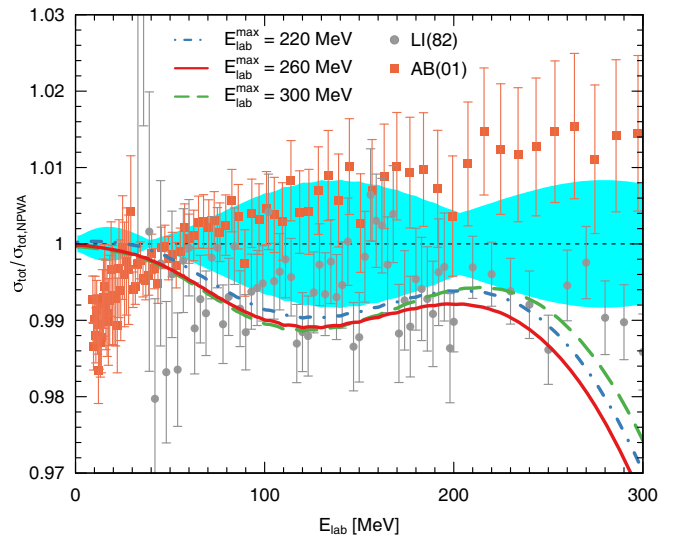


Fig. 14. (Color online) The total cross section σ_{tot} , normalized to the values from the Nijmegen PWA, as obtained at $N^4\text{LO}^+$ using $\Lambda = 450 \text{ MeV}$. Blue dash-dotted, red solid and green dashed lines correspond to the fits up to $E_{\text{lab}}^{\max} = 220$, 260 and 300 MeV, respectively. The cyan band shows the results based on the Nijm I, II and Reid93 potentials of ref. [133]. The LI(82) and AB(01) data are taken from refs. [134] and [135], respectively.

chiral order, the truncation error increases rapidly, and the systematic uncertainty due to the choice of E_{lab}^{\max} in the fits may be expected to become even less relevant.

As described in sect. 6.3, the fits of the $N^4\text{LO}^+$ potentials are performed to scattering data with the laboratory energy of up to $E_{\text{lab}}^{\max} = 260 \text{ MeV}$. To assess the sensitivity to this choice, we performed two additional fits by varying the maximum energy by $\pm 40 \text{ MeV}$, *i.e.* by including the data up to $E_{\text{lab}}^{\max} = 220$ and 300 MeV, and using the same fitting protocol. Notice that further reducing E_{lab}^{\max} makes our fits unstable simply because the data do not contain sufficient information to accurately constrain the values of the NN LECs. The resulting values of the χ^2/datum for three different fits are collected in table 5 for the intermediate cutoff of $\Lambda = 450 \text{ MeV}$. The description of pp data in terms of the χ^2/datum turns out to be very stable with

Table 6. S-wave scattering lengths and effective range parameters as obtained at N^4LO^+ for the cutoff values of $\Lambda = 400, 450, 500$ and 550 MeV . The first uncertainty is statistical, the second one corresponds to the truncation error at N^4LO , the third one estimates the sensitivity to the πN LECs while the last uncertainty reflects the sensitivity to the choice of the maximum energy in the fits as explained in the text. The statistical uncertainty of the np scattering lengths are calculated from the corresponding allowed variation of the χ^2/datum as described in sect. 7.5.1. For all other observables, the estimations are based on the quadratic approximation in eq. (88) along with the corresponding covariance matrices. The np (pp) phase shifts are calculated with respect to Riccati-Bessel (Coulomb) functions.

	$\Lambda = 400\text{ MeV}$	$\Lambda = 450\text{ MeV}$	$\Lambda = 500\text{ MeV}$	$\Lambda = 550\text{ MeV}$	Empirical
a_{1S0}^{np} (fm)	$-23.739^{(+4)}_{(-4)}(4)(4)(5)$	$-23.739^{(+4)}_{(-4)}(4)(6)(2)$	$-23.742^{(+4)}_{(-4)}(4)(8)(0)$	$-23.744^{(+4)}_{(-4)}(4)(9)(1)$	$-23.748(10)$ [136] $-23.740(20)$ [115]
r_{1S0}^{np} (fm)	$2.706^{(+8)}_{(-8)}(19)(20)(30)$	$2.697^{(+7)}_{(-8)}(16)(22)(17)$	$2.698^{(+6)}_{(-7)}(12)(24)(15)$	$2.702^{(+6)}_{(-7)}(11)(25)(14)$	$2.75(5)$ [136] $2.77(5)$ [115]
a_{3S1} (fm)	$5.420^{(+1)}_{(-1)}(1)(1)(2)$	$5.420^{(+1)}_{(-1)}(1)(2)(1)$	$5.421^{(+1)}_{(-1)}(1)(3)(0)$	$5.422^{(+1)}_{(-1)}(1)(3)(0)$	$5.424(4)$ [136] $5.4194(20)^{(a)}$ [137]
r_{3S1} (fm)	$1.754^{(+2)}_{(-2)}(2)(1)(2)$	$1.754^{(+2)}_{(-2)}(1)(2)(1)$	$1.755^{(+2)}_{(-2)}(1)(3)(0)$	$1.756^{(+2)}_{(-2)}(1)(3)(0)$	$1.759(5)$ [136] $1.7536(25)^{(a)}$ [137]
a_{1S0}^{pp} (fm)	$-7.814^{(+1)}_{(-1)}(1)(2)(0)$	$-7.815^{(+1)}_{(-1)}(1)(2)(0)$	$-7.816^{(+1)}_{(-2)}(1)(2)(0)$	$-7.816^{(+1)}_{(-3)}(2)(3)(0)$	$-7.817(4)^{(b)}$ [95]
r_{1S0}^{pp} (fm)	$2.766^{(+2)}_{(-2)}(4)(7)(1)$	$2.770^{(+2)}_{(-2)}(3)(9)(1)$	$2.772^{(+2)}_{(-2)}(6)(10)(0)$	$2.773^{(+2)}_{(-2)}(8)(10)(0)$	$2.780(20)^{(b)}$ [95]

(a) Recommended values; the errors are claimed to be “educated guesses”.

(b) Recommended values for the phase shifts δ_C with respect to Coulomb functions.

respect to the included energy range. We do, however, observe minor improvement for high-energy data upon including them in the fits as may be expected. Quite remarkably, there is almost no worsening in the description of pp data when lowering E_{lab}^{\max} down to 220 MeV. The stability of the pp results is also reflected in the very small changes of the corresponding NN LECs and phase shifts. For np data, the dependence of the χ^2/datum on E_{lab}^{\max} appears to be somewhat larger. This is in line with the discussion in sect. 7.5.1 and presumably can be traced back to larger experimental errors of np data as compared to pp ones, along with the larger number of parameters which need to be determined for np observables. The resulting variations in the values of LECs turn out to be roughly of the same size as the corresponding statistical uncertainties except for E_{1F3} , which does change strongly when performing fits up to $E_{\text{lab}}^{\max} = 220\text{ MeV}$. Again, this is a consequence of the fact that the scattering data below this energy do not allow for an accurate determination of this LEC. Still, even for np results, it is still fair to say that the sensitivity to the variation of E_{lab}^{\max} is very small except for the softest cutoff choice of $\Lambda = 350\text{ MeV}$. As a representative example, we show in fig. 14 the dependence of the total cross section for np scattering as function of the laboratory energy, normalized to the values from the Nijmegen partial wave analysis, on the choice of E_{lab}^{\max} for N^4LO^+ using $\Lambda = 450\text{ MeV}$. Notice that the data by Abfalterer *et al.*, AB(01), are not included in the 2013 Granada database. It is clear that the size of the variations is small compared with the other un-

certainties such as especially the truncation error, which *e.g.* amounts to $\delta(\sigma_{\text{tot}}/\sigma_{\text{tot, NPWA}}) \sim 1.5\%$ at the energy of $E_{\text{lab}} = 200\text{ MeV}$.

7.6 Effective range parameters

Having specified our approach to uncertainty quantification, we are now in the position to present results for the S-wave scattering lengths and effective range parameters. Our N^4LO^+ predictions for the various quantities are collected in table 6 for the cutoff values of $\Lambda = 400\text{--}550\text{ MeV}$. A significant amount of cutoff artefacts for the case of $\Lambda = 350\text{ MeV}$ makes the uncertainty analysis in that case less straightforward, and for this reason we refrain from showing the corresponding results. We have, however, verified that the values for all considered quantities based on the softest cutoff choice are consistent with the ones given in table 6. Finally, we remind the reader that given the essentially perfect description of the data at N^4LO^+ , the results of our partial wave analysis at this order can be regarded as reference values for these quantities and include a comprehensive analysis of the various sources of uncertainty. The quoted truncation errors correspond to N^4LO . We regard the results for the cutoff choice of $\Lambda = 450\text{ MeV}$, which leads to the best description of the experimental data, as our final predictions.

For np scattering, our results correspond to the standard phase shifts calculated with respect to Riccati-Bessel

functions. For pp 1S_0 phase shift, the values shown in table 6 correspond to the phase shifts δ_{C1+N}^{C1} calculated with respect to Coulomb wave functions by means of the well-known modified effective range expansion, see *e.g.* ref. [138] and references therein. We emphasize that due to the presence of the long-range electromagnetic interactions beyond the Coulomb one, the definition of the corresponding phase shift is, strictly speaking, model dependent, see ref. [95] for more details. We, however, expect the emerging model dependence to be small at the level of accuracy of our calculations. The quoted empirical values for the np 1S_0 parameters are the ones which are most frequently used in the literature, see refs. [115, 139] and references therein for more details. For the pp 1S_0 parameters, we show the recommended values from the partial wave analysis of ref. [95]. More precisely, we have used the results from table VI of that paper to adjust their recommended values of $a_{1S0, \text{EM}}^{\text{PP}} = -7.804 \pm 0.004 \text{ fm}$, $r_{1S0, \text{EM}}^{\text{PP}} = 2.784 \pm 0.020 \text{ fm}$, calculated from the phase shift $\delta_{\text{EM}+N}^{\text{EM}}$ with respect to the full electromagnetic interaction and employing a more complicated definition of the effective range function, to the ones corresponding to δ_{C1+N}^{C1} . Finally, for the 3S_1 parameters, we provide, in addition to the compilation of experimental values of ref. [136], also the results from the Nijmegen partial wave analysis [137].

Our results for the scattering lengths and effective range parameters are in an excellent agreement with the empirical numbers. The largest deviations are observed for r_{1S0}^{np} , but the discrepancy is still only at the level of $\sim 1.5\sigma$. We further emphasize that our predictions are, in many cases, more precise than the quoted experimental and/or empirical values. The results collected in table 6 also illustrate the usefulness of the approach for quantifying truncation errors in chiral EFT advocated in ref. [6], which allows one to perform independent error analysis for each cutoff value. While the results corresponding to different cutoffs are correlated with each other and, therefore, cannot be combined together to decrease the uncertainty, they do provide a useful consistency check of the calculations and error analysis. In particular, it is comforting to see that the analyses carried out at different values of Λ yield consistent results for all extracted quantities.

We find that the np 1S_0 effective range shows by far the largest uncertainty. This can probably be traced back to the lower accuracy of the np data as compared to the pp ones and to the weaker theoretical constraints on the long-range interaction in this channel, which is not sensitive to the tensor part of the OPEP¹². It is also instructive to look at the systematics of various uncertainties with respect to the cutoff variation. In particular, the statistical uncertainty turns out to be largely insensitive to the value of Λ in line with the already discussed results for the LECs. On the other hand, decreasing the cutoff values results in integrating out a part of the TPEP. This explains why our results for soft choices of Λ show a smaller un-

¹² The same arguments apply to the np 1S_0 scattering length too, which is, however, additionally stabilized by constraining the value of the np coherent scattering length in our fits.

tainty from the variation of the πN LECs. On the other hand, lower values of the cutoff result in increased distortions of phase shifts at larger energies, which increases the sensitivity of the fits to the choice of $E_{\text{lab}}^{\text{max}}$. Again, this is clearly reflected in the uncertainty pattern of our predictions. For $\Lambda \geq 450 \text{ MeV}$, the uncertainty from the choice of $E_{\text{lab}}^{\text{max}}$ in the fits turns out to be negligible compared to the other error sources.

Further, we emphasize that while the uncertainties from different sources turn out to be of a comparable size for the effective range parameters at $N^4\text{LO}$, the uncertainty at lower chiral orders and for higher-energy observables at $N^4\text{LO}$ and $N^4\text{LO}^+$ is, in most cases, dominated by the truncation error, see sect. 7.8 for more details.

Finally, given the fact that our results for the S-wave scattering lengths are affected by the constrained values of the deuteron binding energy and the np coherent scattering length, we have used in these cases a more general approach for quantifying the statistical uncertainty based on the corresponding allowed variation of the χ^2/datum as explained in sect. 7.5.1. The usage of the covariance matrix together with the quadratic approximation in eq. (88) is found to yield overestimated statistical uncertainties for these observables.

7.7 Deuteron properties

We now turn to the deuteron properties. As already pointed out before, we use the deuteron binding energy of $B_d = 2.224575 \text{ MeV}$ [119] as an additional constraint when performing the fits starting from $N^3\text{LO}$. All other deuteron properties come out as predictions. Similarly to our earlier studies in refs. [6, 7], we find a very good convergence for the deuteron parameters with respect to the chiral order as exemplified in table 7 for the case of the intermediate cutoff $\Lambda = 450 \text{ MeV}$. Notice further that contrary to those studies, we do not include in our fits any constraints on the D-state probability P_D as already explained in sect. 6.3. In table 8, we compare our $N^4\text{LO}^+$ predictions for all considered cutoff values with each other and with the corresponding results based on the potentials of ref. [8]¹³. We also show the expectation value of the kinetic energy which, while not being an observable quantity, allows one to draw conclusions regarding the strength of the short-range repulsion and perturbativeness of the potentials. For the semilocal coordinate-space regularized potentials of refs. [6, 7], the expectation value of the kinetic energy in the deuteron varies in the range of $\langle T_{\text{kin}} \rangle = 16.13 \dots 23.33 \text{ MeV}$ at $N^3\text{LO}$ and $\langle T_{\text{kin}} \rangle = 15.27 \dots 20.59 \text{ MeV}$ at $N^4\text{LO}$ depending on the cutoff R . These large values are in line with the nonperturbative nature of these potentials [74] and signal the appearance of a strong repulsive core in the 3S_1 channel, which can be traced back to the large numerical values

¹³ While the corresponding potentials are referred to as $N^4\text{LO}$ in ref. [8], we prefer to regard them as $N^4\text{LO}^+$ since they also include the four $N^5\text{LO}$ contact interactions in F-waves given in eq. (17). No strict $N^4\text{LO}$ potentials are provided in that paper.

Table 7. Deuteron binding energy B_d , expectation value of the kinetic energy $\langle T_{\text{kin}} \rangle$, asymptotic S state normalization A_S , asymptotic D/S state ratio η , radius r_d and quadrupole moment Q at various orders in the chiral expansion for the cutoff $\Lambda = 450$ MeV in comparison with empirical values. Also shown is the D -state probability P_D . Notice that r_d and Q_d are calculated without taking into account meson-exchange current contributions and relativistic corrections. The deuteron binding energy is calculated by solving the relativistic Schrödinger equation.

	LO	NLO	$N^2\text{LO}$	$N^3\text{LO}$	$N^4\text{LO}$	$N^4\text{LO}^+$	Empirical
B_d (MeV)	2.1201	2.1843	2.2012	2.2246 ^(a)	2.2246 ^(a)	2.2246 ^(a)	2.224575(9) [119]
$\langle T_{\text{kin}} \rangle$ (MeV)	14.24	13.47	14.44	14.35	14.16	14.22	—
A_S (fm $^{-1/2}$)	0.8436	0.8727	0.8786	0.8844	0.8847	0.8847	0.8846(8) [140]
η	0.0220	0.0236	0.0251	0.0257	0.0255	0.0255	0.0256(4) [141]
r_d (fm)	1.946	1.967	1.970	1.966	1.966	1.966	1.97535(85) ^(b) [142]
Q (fm 2)	0.227	0.249	0.268	0.272	0.269	0.270	0.2859(3) [143]
P_D (%)	2.77	3.59	4.63	4.70	4.54	4.59	—

^(a) The deuteron binding energy has been taken as input in the fit.

^(b) This value corresponds to the so-called deuteron structure radius, which is defined as a square root of the difference of the deuteron, proton and neutron mean square charge radii.

Table 8. Deuteron properties calculated based on the $N^4\text{LO}^+$ potentials of this work and the ones of ref. [8] for different cutoff values Λ (in units of MeV). For notation see table 7. Notice that the deuteron binding energy is calculated by solving the nonrelativistic (relativistic) Schrödinger equation for the potentials of ref. [8] (of this work).

$N^4\text{LO}^+$ potentials of [8]			SMS chiral potentials at $N^4\text{LO}^+$, this work					Empirical
$\Lambda = 450$	$\Lambda = 500$	$\Lambda = 550$	$\Lambda = 350$	$\Lambda = 400$	$\Lambda = 450$	$\Lambda = 500$	$\Lambda = 550$	
B_d (MeV)	2.2246 ^(a)	2.2246 ^(a)	2.2246 ^(a)	2.2246 ^(a)	2.2246 ^(a)	2.2246 ^(a)	2.2246 ^(a)	2.224575(9) [119]
$\langle T_{\text{kin}} \rangle$ (MeV)	13.05	13.32	14.04	12.73	13.44	14.22	15.11	15.98
A_S (fm $^{-1/2}$)	0.8852	0.8852	0.8851	0.8848	0.8847	0.8847	0.8849	0.8846(9) [140]
η	0.0254	0.0258	0.0257	0.0256	0.0255	0.0255	0.0257	0.0256(4) [141]
r_d (fm)	1.966	1.973	1.970	1.965	1.965	1.966	1.967	1.968
Q (fm 2)	0.269	0.273	0.271	0.265	0.267	0.270	0.273	0.276
P_D (%)	4.38	4.10	4.13	3.58	4.12	4.59	5.01	5.34

^(a) The deuteron binding energy has been taken as input in the fit.

^(b) This value corresponds to the so-called deuteron structure radius, which is defined as a square root of the difference of the deuteron, proton and neutron mean square charge radii.

of the redundant contact interactions at order Q^4 , see table II of ref. [6]. Further, we observe somewhat larger values for the asymptotic S -state normalization A_S as compared with $A_S = 0.8843 \dots 0.8846 \text{ fm}^{-1/2}$ using the $N^4\text{LO}$ potentials of ref. [7]. This difference emerges primarily from using the πN LECs from the Roy-Steiner equation analysis. The remaining deuteron properties come out rather similar to the ones based on the coordinate-space regularized potentials of refs. [7].

In fig. 15, we show the deuteron wave functions at $N^4\text{LO}^+$ for all considered cutoff values (left panel). The S -state wave functions appear to be very stable with respect to the cutoff variation at distances $r \gtrsim 1 \text{ fm}$ and take the values of $u(r)/r|_{r=0} = 0.32 \dots 0.55 \text{ fm}^{-3/2}$, depending on the cutoff, at the origin. This has to be compared with the corresponding variation for the $N^4\text{LO}$ potentials of ref. [7], $u(r)/r|_{r=0} = -0.22 \dots 0.14 \text{ fm}^{-3/2}$, and is in line with a significantly smaller amount of short-distance repulsion in

the new potentials already mentioned in connection with the expectation value of the kinetic energy. The D -state wave function shows a considerably stronger cutoff variation and becomes insensitive to the values of Λ only for $r \gtrsim 2.5 \text{ fm}$. We also show in the right panel of fig. 15 the corresponding wave functions from the nonlocal potentials of ref. [8] at $N^4\text{LO}^+$. The oscillations occur presumably due to the non-Gaussian form of the regulator functions employed in that paper, *i.e.* due to choosing $n \geq 2$ in eq. (2). Interestingly, one observes that the maximum probability for the nucleons be in a D -state is shifted in the potentials of ref. [8] towards considerably larger distances. This could be a consequence of a stronger suppression of the tensor part of the OPEP at intermediate distances for the nonlocal regulator employed in that paper.

Finally, we list in table 9 our results for the asymptotic S state normalization A_S and asymptotic D/S state ratio η at $N^4\text{LO}^+$ along with the corresponding uncer-

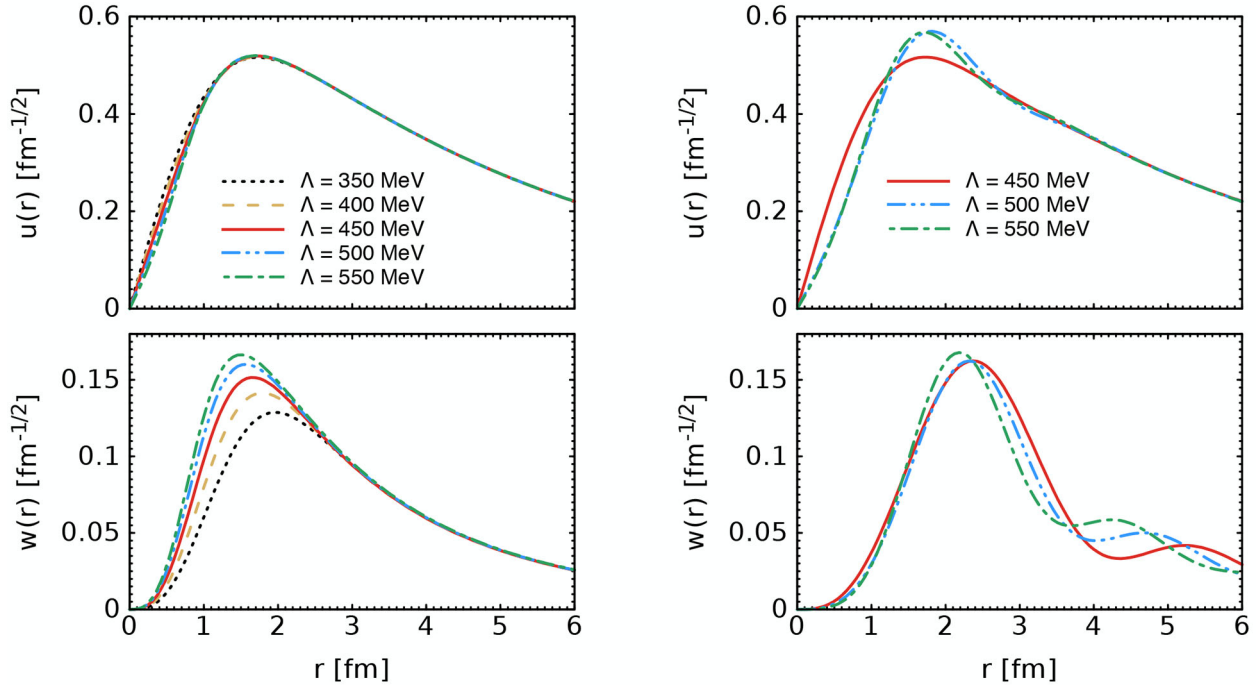


Fig. 15. (Color online) Deuteron wave functions in coordinate space based on the SMS N^4LO^+ potentials of this work (left panel) and N^4LO^+ potentials of ref. [8] (right panel). Black dotted, brown dashed, red solid, blue dash-dotted and green dash-double-dotted lines show the results obtained using the cutoffs $\Lambda = 350, 400, 450, 500$, and 550 MeV, respectively.

Table 9. Predictions for the asymptotic S state normalization A_S and asymptotic D/S state ratio η at N^4LO^+ for the cutoff values of $\Lambda = 400, 450, 500$ and 550 MeV. The first uncertainty is statistical, the second one corresponds to the truncation error at N^4LO , the third one estimates the sensitivity to the πN LECs while the last uncertainty reflects the sensitivity to the choice of the maximum energy in the fits as explained in the text. The statistical uncertainty of A_S is calculated from the corresponding allowed variation of the χ^2/datum as described in sect. 7.5.1. For η , the estimations are based on the quadratic approximation in eq. (88) along with the corresponding covariance matrices.

	$\Lambda = 400$ MeV	$\Lambda = 450$ MeV	$\Lambda = 500$ MeV	$\Lambda = 550$ MeV	Empirical
A_S (fm $^{-1/2}$)	$0.8847^{(+3)}_{(-3)}(6)(4)(4)$	$0.8847^{(+3)}_{(-3)}(3)(5)(1)$	$0.8849^{(+3)}_{(-3)}(1)(7)(0)$	$0.8851^{(+3)}_{(-3)}(3)(8)(1)$	$0.8846(8)$ [140]
η	$0.0255^{(+1)}_{(-1)}(1)(3)(2)$	$0.0255^{(+1)}_{(-1)}(1)(4)(1)$	$0.0257^{(+1)}_{(-1)}(1)(5)(1)$	$0.0258^{(+1)}_{(-1)}(1)(5)(1)$	$0.0256(4)$ [141]

tainties. Our predictions for these quantities agree with the empirical values and with the values obtained from the phenomenological potentials including the CD Bonn [115], Nijm I, II and Reid93 [133] potentials. On the other hand, there is a significant disagreement with the partial wave analysis by the Granada group of ref. [114], which quotes the values of $A_S = 0.8829(4)$ fm $^{1/2}$ and $\eta = 0.02493(8)$ (where the uncertainties are of the purely statistical nature). The systematics of the various error sources of A_S and η with respect to the cutoff variation appears to be similar to the one discussed in sect. 7.6 in the context of the effective range parameters. Notice that in spite of a significant dependence of A_S and η on the values of the πN LECs, it is not possible to discriminate between the different sets given the accuracy of the empirical values (and statistical and truncation uncertainties of our results). We do not quote the uncertainty for the remaining deuteron properties either because they are not ob-

servable ($\langle T_{\text{kin}} \rangle, P_D$) or since our present calculations of them are incomplete (r_d, Q). Interestingly, these features are also clearly reflected in the cutoff variation for these quantities, which reaches $\sim 23\%$ ($\sim 40\%$) for $\langle T_{\text{kin}} \rangle$ (P_D) for $\Lambda = 350\text{--}550$ MeV. For Q and r_d , the cutoff variation is smaller and amounts to $\sim 4\%$ and 0.15% , respectively¹⁴. In both cases, the observed Λ -dependence is smaller than the deviations from the very precisely known experimental/empirical values listed in table 8. These deviations amount to ~ 0.015 fm 2 and ~ 0.009 fm for Q and r_d , respectively, and are comparable with the truncation errors for these quantities at N^2LO , namely $\delta Q^{(3)} = \pm(0.005\ldots 0.011)$ fm 2 (depending on the cutoff) and $\delta r_d^{(3)} = \pm 0.005$ fm, which estimate the expected size of N^3LO contributions to these observables. This is in

¹⁴ The smaller cutoff dependence of the deuteron radius reflects the long-range nature of this observable as opposed to that of Q .

line with the fact that our calculations do not take into account the relativistic corrections and contributions to the exchange charge operator at $N^3\text{LO}$, see ref. [37, 38] for explicit expressions. Notice, however, that short-range contributions to the exchange charge operator at $N^4\text{LO}$ will likely play a significant role in explaining the discrepancies between our results for Q and r_d and the corresponding empirical values [144, 145]. Our results further indicate that starting from $N^3\text{LO}$, the theoretical uncertainty for both quantities is dominated by the one of the πN LECs similarly to other low-energy observables considered in this and previous sections. For both Q and r_d , employing the πN LECs from set 2 tends to increase the discrepancy with the empirical numbers.

7.8 Phase shifts

In fig. 16, we show the np S-, P-, D- and F-wave phase shifts and the mixing angles ϵ_1 and ϵ_2 as obtained at $N^4\text{LO}^+$ for the cutoff $\Lambda = 450 \text{ MeV}$ along with the estimated truncation uncertainties as explained in appendix D. The resulting values for the pp and np phase shifts and mixing angles in the fitted channels at the laboratory energies of $E_{\text{lab}} = 1, 5, 10, 25, 50, 100, 150, 200, 250$ and 300 MeV are listed in tables 12–19 of this appendix together with the estimated statistical and truncation errors as well as the uncertainties reflecting the sensitivity to the πN LECs and the choice of the maximum fitting energy in the fits. Similarly to the effective range parameters and the deuteron properties, the theoretical uncertainty of the phase shifts at very low energy is typically dominated by the uncertainty in the πN LECs. On the other hand, starting from $E_{\text{lab}} \sim 100 \text{ MeV}$, the truncation error starts becoming dominant. With very few exceptions, the statistical uncertainty is found to be negligibly small as compared to other error sources. The sensitivity to the employed energy range in the fits also appears to be small except for few cases such as especially the $^1\text{F}_3$ phase shift, for which it dominates the theoretical uncertainty.

As already pointed out, our $N^4\text{LO}^+$ fit for $\Lambda = 450 \text{ MeV}$ provides a nearly perfect description of the data and thus qualifies to be considered as partial wave analysis. It is, therefore, interesting to compare our results for phase shifts with the ones from other PWAs. For pp phase shifts and mixing angles, our results are in a very good agreement with the Nijmegen PWA [20] except for the $^3\text{P}_0$ phase shift at low energy, where the differences are at the $\sim 3\sigma$ level assuming that our uncertainty is dominated by the statistical error. The discrepancy is slightly less pronounced for the Granada PWA of ref. [114]. Notice that similarly to that paper, we find considerably smaller statistical uncertainties as compared with the Nijmegen PWA. More differences are found for np phase shifts and mixing angles. First, the already mentioned discrepancy in the $^3\text{P}_0$ phase shift at low energy persists in the np system, where it becomes even more pronounced. For example, we obtain at $E_{\text{lab}} = 50 \text{ MeV}$ the value of $\delta_{3P0}^{\text{np}} = 11.02^\circ \pm 0.05^\circ$, where the uncertainty is purely statistical, which has to be compared

with the results from the Nijmegen and Granada PWA of $\delta_{3P0}^{\text{np}} = 10.70^\circ$ and $\delta_{3P0}^{\text{np}} = 11.30^\circ \pm 0.03^\circ$, respectively, and with the value from the Gross-Stadler analysis of ref. [146], $\delta_{3P0}^{\text{np}} = 10.61^\circ$. Furthermore, there are significant differences between our results and the ones of both the Granada and Gross-Stadler PWA for the $^3\text{S}_1$ phase shifts at the lowest considered energy of $E_{\text{lab}} = 1 \text{ MeV}$. Since the deuteron S-state normalization A_S is correlated with the $^3\text{S}_1$ scattering length, this discrepancy is probably the origin of the different predictions for this observable mention in sect. 7.7. Our results for the $^3\text{S}_1$ phase shift are, however, in an excellent agreement with those from the Nijmegen PWA. We also observe some discrepancies between our results and those from the Nijmegen [20] and Granada [114] PWA for the mixing angle ϵ_2 (ϵ_3) at low energies (at energies $E_{\text{lab}} \gtrsim 200 \text{ MeV}$). Comparison of our results with those from the Gross-Stadler analysis of ref. [146] reveals more differences, in particular also in the $^3\text{P}_1$, $^3\text{F}_3$ and $^3\text{F}_4$ channels. We emphasize, however, that their analysis is based solely on np scattering data and thus potentially suffers from considerably larger statistical uncertainties, which are, however, not quoted in that paper. Finally, our $N^4\text{LO}^+$ results agree with the ones from our earlier $N^3\text{LO}$ analysis in ref. [6], see table 7 of that paper. The largest deviation at the level of $\sim 1.5\sigma$ occurs for the pp $^3\text{P}_0$ phase shift at $E_{\text{lab}} = 100 \text{ MeV}$.

We conclude this section with emphasizing that our error analysis does not involve propagation of the uncertainty in the value(s) of the πN coupling constant which, in principle, could significantly affect the results for phase shifts and mixing angles at low energy. Also, a more complete treatment of isospin-breaking effects as compared to the one employed in our analysis would be required in order to draw final conclusions regarding the observed discrepancies. Work along these lines is in progress.

8 Alternative choice of the contact interactions at order Q^4

As described in sect. 2, our choice of the basis of the independent order- Q^4 contact interactions in eqs. (12) and (13) represents just one possible convention. In this section we explore an alternative choice using the parametrization

$$\begin{aligned} D_{1S0}^1 p^2 p'^2 + D_{1S0}^2 (p^4 + p'^4) &=: \tilde{D}_{1S0} (p'^2 + p^2)^2 \\ &\quad + \tilde{D}_{1S0}^{\text{off}} (p'^2 - p^2)^2, \\ D_{3S1}^1 p^2 p'^2 + D_{3S1}^2 (p^4 + p'^4) &=: \tilde{D}_{3S1} (p'^2 + p^2)^2 \\ &\quad + \tilde{D}_{3S1}^{\text{off}} (p'^2 - p^2)^2, \\ D_{\epsilon 1}^1 p^2 p'^2 + D_{\epsilon 1}^2 p^4 &=: \tilde{D}_{\epsilon 1} p^2 (p'^2 + p^2) \\ &\quad + \tilde{D}_{\epsilon 1}^{\text{off}} p^2 (p'^2 - p^2), \end{aligned} \quad (96)$$

and setting

$$\tilde{D}_{1S0}^{\text{off}} = \tilde{D}_{3S1}^{\text{off}} = \tilde{D}_{\epsilon 1}^{\text{off}} = 0. \quad (97)$$

To have a meaningful comparison between the two choices of the contact interactions, we have redone the fits based

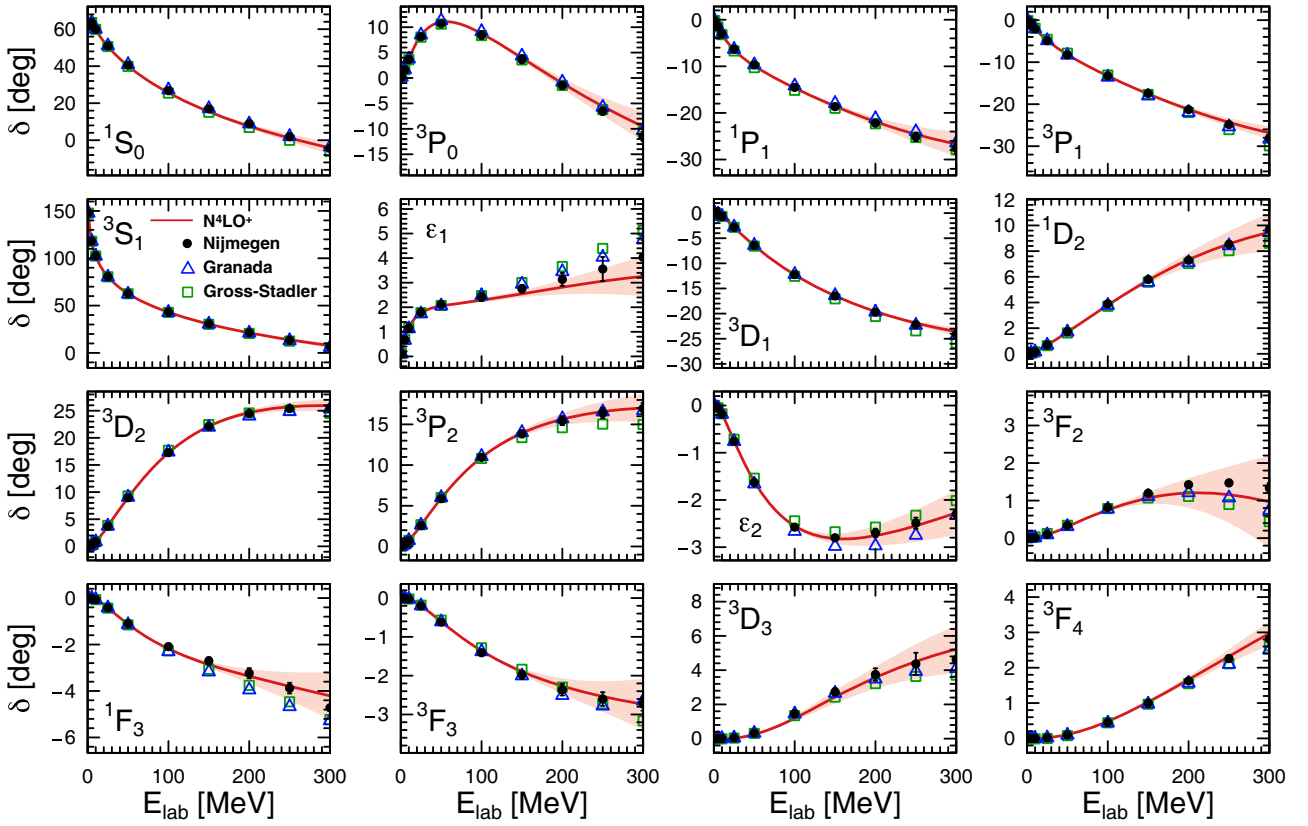


Fig. 16. (Color online) Neutron-proton S-, P-, D- and F-wave phase shifts and the mixing angles ϵ_1 , ϵ_2 and ϵ_3 as obtained at N^4LO^+ using the cutoff $\Lambda = 450$ MeV (red solid lines) in comparison with the Nijmegen [20] (solid dots) the Granada [114] (blue open triangles) and Gross-Stadler [146] (green open squares) PWA. Light shaded bands show the estimated truncation error as explained in appendix D. The shown uncertainties of the Nijmegen PWA correspond to systematic errors estimated from the Nijm I, II and Reid93 potentials [133] as explained in ref. [6].

on the alternative set of contact terms employing the same fitting protocol as described in sect. 6. We then find very similar results for the description of the scattering data. For example, for the intermediate cutoff $\Lambda = 450$ MeV, the χ^2/datum for both the np and pp cases agrees with the corresponding ones listed in table 4 in all considered energy bins to all given figures. The similarity also extends to observables. For example, with the new set of contact interactions, we obtain for the various scattering lengths the values of $a_{1S0}^{\text{np}} = -23.739$ fm, $a_{3S1} = 5.420$ fm and $a_{1S0}^{\text{pp}} = -7.815$ fm, while the corresponding effective ranges are $r_{1S0}^{\text{np}} = 2.697$ fm, $r_{3S1} = 1.754$ fm and $r_{1S0}^{\text{pp}} = 2.770$ fm. Similarly, we obtain $A_S = 0.8847 \text{ fm}^{-1/2}$ and $\eta = 0.0255$ for the asymptotic S state normalization and the asymptotic D/S state ratio, respectively. These values coincide with the ones given in sects. 7.6 and 7.7 for the same cutoff value. Thus, the dependence of our results on the choice of the order- Q^4 contact interactions is negligible at the accuracy level of our calculations. We have verified that this conclusion also holds for the phase shifts. This provides explicit numerical evidence of the redundancy of the corresponding contact interactions.

On the other hand, the off-shell behavior of the potentials does show a dependence on the choice of the contact interactions, which may also significantly affect their

perturbativeness. We found that the choice specified in eqs. (96) and (97) leads to somewhat larger Weinberg eigenvalues and, therefore, to more nonperturbative potentials for the hard cutoff choices as compared with the convention employed in our analysis and given in eqs. (12) and (13). For example, for the cutoff of $\Lambda = 500$ MeV, switching the basis of contact interactions to that given in eqs. (96), (97) increases the maximum values of the largest in magnitude repulsive eigenvalue in the 1S_0 (3S_1 - 3D_1) channel as $0.72 \rightarrow 0.98$ ($1.81 \rightarrow 2.37$) at N^3LO , $0.83 \rightarrow 0.97$ ($0.89 \rightarrow 1.11$) at N^4LO and $0.80 \rightarrow 0.92$ ($0.91 \rightarrow 0.98$) at N^4LO^+ in the considered energy range of $E_{\text{lab}} = 0$ –300 MeV. The effects become even more pronounced for the largest cutoff value of $\Lambda = 550$ MeV.

9 Comparison with other NN potentials

It is instructive to compare our results for the description of NN scattering data with that based on the modern high-precision phenomenological potentials. To this aim we have calculated the values of the χ^2/datum for the reproduction of pp and np data from the 2013 Granada database [109] using the CD Bonn [115] and the Nijm I, II and Reid93 potentials developed by the Nijmegen

Table 10. χ^2/datum for the description of the neutron-proton and proton-proton scattering data at $N^4\text{LO}^+$ for $\Lambda = 450 \text{ MeV}$ in comparison with the high-precision phenomenological potentials. For each potential, the number of adjustable parameters is indicated in the subscript. For the SMS $N^4\text{LO}^+$ potential, 27+1 refer to 27 contact interactions contributing to neutron-proton and proton-proton channels as given in table 2 and the cutoff value.

E_{lab} bin	CD Bonn ₍₄₃₎ [115]	Nijm I ₍₄₁₎ ^(a) [133]	Nijm II ₍₄₇₎ ^(a) [133]	Reid93 ₍₅₀₎ ^(a) [133]	SMS $N^4\text{LO}_{(27+1)}^+$, this work
neutron-proton scattering data					
0–100	1.08	1.07	1.08	1.09	1.08
0–200	1.08	1.07	1.07	1.09	1.07
0–300	1.09	1.08	1.08	1.10	1.06
proton-proton scattering data					
0–100	0.89	0.87	0.88	0.85	0.86
0–200	0.98	0.98	1.00	0.99	0.95
0–300	1.01	1.03	1.05	1.04	1.00

^(a) Since the potentials developed by the Nijmegen group are only available for $j \leq 9$, we have supplemented them by our LO potential for $j > 9$.

group [133]. In table 10, the corresponding values of the χ^2/datum are compared with the ones based on our $N^4\text{LO}^+$ potential for the cutoff $\Lambda = 450 \text{ MeV}$ in three energy bins of $E_{\text{lab}} = 0\text{--}100 \text{ MeV}$, $0\text{--}200 \text{ MeV}$ and $0\text{--}300 \text{ MeV}$. Notice that we found it to be insufficient to only include partial waves with $j \leq 9$ and have, therefore, extended the Nijm I, II and Reid93 potentials by using for $j > 9$ partial waves the results of the OPEP taken from our own LO potentials.

It is difficult to precisely benchmark our results for χ^2/datum against the values quoted in the original publications mainly due to the different selection of experimental data, but also due to possible differences in the treatment of the long-range electromagnetic interactions. The potentials of the Nijmegen group were fitted to their 1993 database with 1787 pp and 2514 np data below $E_{\text{lab}} = 350 \text{ MeV}$ [133]. The CD Bonn potential was fitted to a larger database which included additional data available in the year 2000, featuring 2932 pp and 3058 data [115]. The self-consistent 2013 Granada database includes 2996 pp and 3717 np mutually consistent scattering data (including normalizations)¹⁵. While our χ^2/datum values for the Nijmegen potentials are somewhat higher than the ones quoted in their original publication [133], namely $\chi^2/\text{datum} = 1.05$ (1.00), 1.04 (1.00), 1.04 (1.00) for np (pp) scattering data below 350 MeV for the Nijm I, Nijm II and Reid93 potentials, respectively, we find that these interactions are still doing a remarkably good job in reproducing the 2013 Granada database¹⁶. Our slightly increased χ^2 values presumably just reflect the effect of including additional data in the Granada database. For the CD Bonn potential, our result for the reproduc-

tion of pp data agrees with the corresponding value of $\chi^2/\text{datum} = 1.01$ for energies below 350 MeV given in ref. [115]. This is consistent with the fact that the number of pp data in the Granada database is only slightly larger than the one used in that paper. On the other hand, we do observe a higher value for the description of np data as compared with $\chi^2/\text{datum} = 1.02$ quoted in ref. [115], which probably reflects a considerably larger number of np data included in the Granada database.

As shown in table 10, the reproduction of the np and pp data below 300 MeV by our $N^4\text{LO}^+$ potential with $\Lambda = 450 \text{ MeV}$ is more accurate than by any of the considered high-precision potentials¹⁷. This is a remarkable result, especially if one takes into account that the number of adjustable parameters is $\sim 40\%$ smaller as compared with the one used in these potentials. For the sake of completeness, we also mention that the partial wave analysis by the Granada group obtains $\chi^2/\text{datum} = 1.04$ for both the np and pp data below $E_{\text{lab}} = 350 \text{ MeV}$ using 46 parameters [109]. In ref. [147], this group was also able to describe np and pp data below 350 MeV with $\chi^2/\text{datum} = 1.07$ using a coarse-grained NN potential involving the OPEP and TPEP and featuring 30 short-range parameters, 1 cutoff and 3 parameters corresponding to the πN LECs c_1 , c_3 and c_4 .

Finally, we compare in table 11 the description of the np and pp data using the semilocal $N^4\text{LO}^+$ potential of this work for $\Lambda = 450 \text{ MeV}$ with that based on the non-local $N^3\text{LO}$ potentials of ref. [17] and the recent $N^4\text{LO}^+$ potentials of ref. [8]. Here, our results for the χ^2/datum values show larger deviations from the ones quoted in the original papers. The increased sensitivity to the selection of data as compared with the results based on the high-

¹⁵ The usage of an improved data selection criterium has allowed the authors of ref. [109] to keep some of the data rejected by the Nijmegen group.

¹⁶ Increasing the maximum energy of the included scattering data from $E_{\text{lab}} = 300 \text{ MeV}$ to 350 MeV adds $\sim 0.02\text{--}0.03$ to the corresponding χ^2/datum values for all considered phenomenological potentials.

¹⁷ The description of the data can be further optimized by performing the fits up to $E_{\text{lab}}^{\max} = 300 \text{ MeV}$ rather than up to $E_{\text{lab}}^{\max} = 260 \text{ MeV}$. We then obtain at $N^4\text{LO}^+$ the values of $\chi^2/\text{datum} = 1.08$, 1.03, 1.04 and 1.07 for both np and pp data using the cutoffs of $\Lambda = 400$, 450, 500 and 550 MeV, respectively.

Table 11. χ^2/datum for the description of the np and pp scattering data at $N^4\text{LO}^+$ for $\Lambda = 450 \text{ MeV}$ in comparison with the $N^3\text{LO}$ and $N^4\text{LO}^+$ potentials of refs. [17] and [8], respectively. All cutoff values are given in units of MeV.

E_{lab} bin	EM $N^3\text{LO}$ [17]		EMN $N^4\text{LO}^+$ [8]			SMS $N^4\text{LO}^+$, this work
	$\Lambda = 500$	$\Lambda = 600$	$\Lambda = 450$	$\Lambda = 500$	$\Lambda = 550$	$\Lambda = 450$
neutron-proton scattering data						
0–100	1.17	1.35	1.28	1.11	1.11	1.08
0–200	1.17	1.33	1.33	1.18	1.23	1.07
0–300	1.23	1.37	2.48	1.26	1.35	1.06
proton-proton scattering data						
0–100	1.01	1.35	0.90	1.01	1.17	0.86
0–200	1.32	1.60	1.05	1.16	1.43	0.95
0–300	1.39	2.07	1.46	1.21	1.41	1.00

precision potentials is probably a consequence of their less precise nature. Specifically, our χ^2 values for pp data in the lowest energy bin turn out to be lower than the ones given in refs. [8, 17], but the value of $\chi^2/\text{datum} = 1.21$ for the reproduction of pp data in the range of $E_{\text{lab}} = 0$ –300 MeV using the $N^4\text{LO}^+$ potential of ref. [8] with $\Lambda = 500 \text{ MeV}$ agrees with the one given in that paper for the energy range of $E_{\text{lab}} = 0$ –290 MeV. On the other hand, for np data, we find significantly larger values in all energy bins. One should further keep in mind that the values of the χ^2/datum for the nonlocal potentials of refs. [8, 17] given in table 11 do not provide a very accurate measure for the achievable accuracy of these interactions as they were fitted to a different data set. However, our results for the phenomenological high-precision potentials discussed above indicate that the impact of using different databases should be fairly small.

When looking at the results for the cutoff $\Lambda = 500 \text{ MeV}$ in table 11, one observes that the description of the data with the old $N^3\text{LO}$ potential of ref. [17] is almost comparable in quality with that based on the new $N^4\text{LO}^+$ potential of ref. [8], which, however, involves additional contact interactions in F-waves. This seemingly contradictory result can presumably be traced back to the additional optimization steps performed in ref. [17], which involve fine tuning of the πN LECs c_i and the usage of a partial wave dependent functional form of the regulator, which effectively increase the number of adjustable parameters in that model¹⁸. To allow for a more detailed comparison between the nonlocal and semilocal potentials at $N^4\text{LO}^+$, we show in fig. 17 the χ^2/datum values for the reproduction of np and pp data as a function of the employed cutoff Λ . Notice that the $N^4\text{LO}^+$ potentials of ref. [8] are only available for the cutoff values of $\Lambda = 450$, 500 and 550 MeV. While our semilocal interactions yield, in spite of having less short-range parameters, a significantly better description of the 2013 Granada database than the ones of ref. [8] in all considered cases, the differences become especially pronounced for softer cutoff choices. Indeed, the χ^2/datum for the nonlocal $N^4\text{LO}^+$

potentials increases rapidly for the cutoff $\Lambda = 450 \text{ MeV}$ as compared to $\Lambda = 500 \text{ MeV}$ (except for pp data at low and intermediate energy), while our semilocal potentials show a very small amount of finite regulator artefacts even for $\Lambda = 400 \text{ MeV}$. We attribute the superior performance of the semilocal potentials primarily to the employed local regularization of the pion exchange contributions, which maintains the long-range part of the interaction and reduces the amount of cutoff artefacts.

10 Summary and conclusions

We now summarize the main results of our paper.

- We have shown that three out of fifteen $N^3\text{LO}$ NN contact interactions employed *e.g.* in refs. [6–8, 16, 17], namely the ones which contribute to the 1S_0 and 3S_1 - 3D_1 channels, are redundant as they can be eliminated by performing the short-range unitary transformations specified in eq. (5), see also ref. [61] for a similar conclusion reached by a Bayesian analysis. Such unitary transformations only affect the values of the LECs accompanying short-range operators that need to be determined from the data anyway, but do not change the expressions for the nuclear forces and current operators. This unitary ambiguity can, in particular, be exploited to reshuffle parts of the short-range many-body forces into the off-shell behavior of the NN potential at short distances, see ref. [148] for a general discussion. Furthermore, using the $N^4\text{LO}$ potentials of ref. [7], we have demonstrated that removing the redundant interactions according to eq. (13) leads to a strong suppression of the off-diagonal matrix elements in the 1S_0 and 3S_1 channels at momenta of the order of $p \sim 600 \text{ MeV}$ and results in much softer potentials as compared to the ones of ref. [7]. The increased perturbativeness of the resulting potentials is verified and further quantified by performing a Weinberg eigenvalue analysis.
- We have introduced a simple momentum-space regularization approach for the long-range part of the interaction by an appropriate modification of the pion propagators in the ultraviolet region. Contrary to the

¹⁸ Ref. [8] does not provide the values of the exponent n when regularizing the contact interactions using eq. (2). The rationale behind their actual choice is not clear to us.

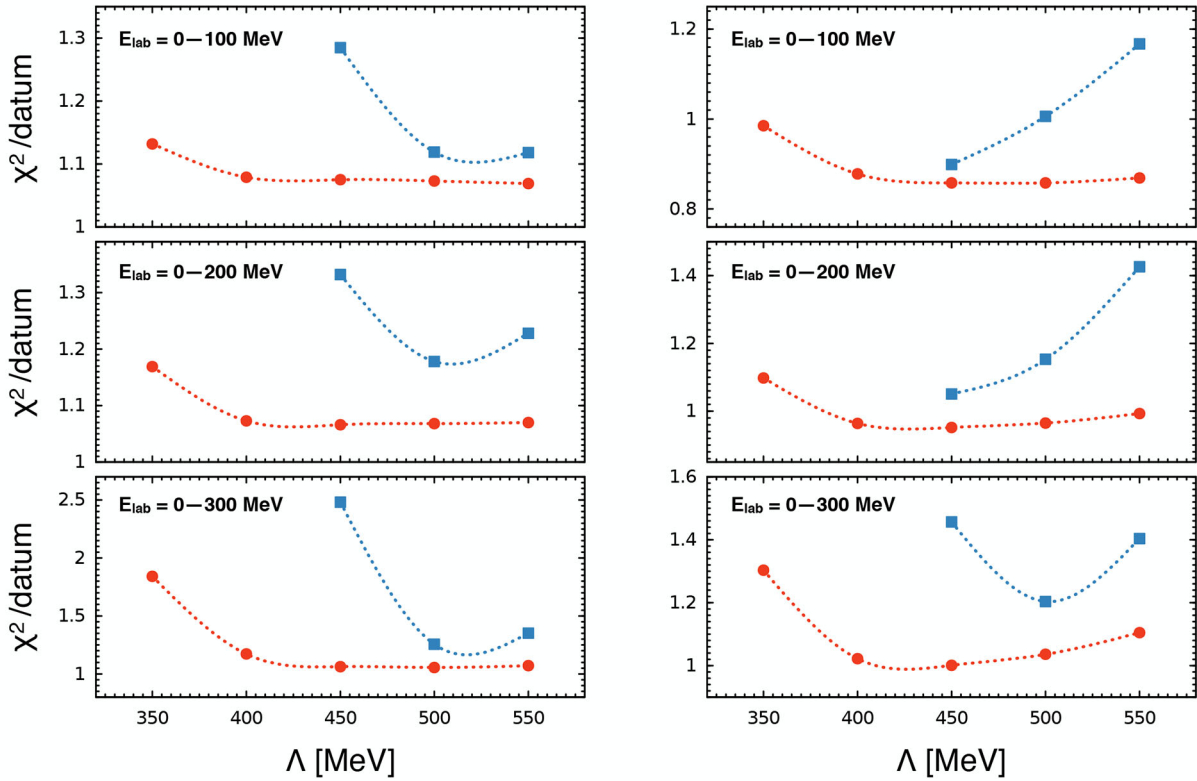


Fig. 17. (Color online) χ^2/datum for the description of the neutron-proton (left panel) and proton-proton (right panel) scattering data in the energy bins of $E_{\text{lab}} = 0 - 100 \text{ MeV}$ (upper row), $E_{\text{lab}} = 0 - 200 \text{ MeV}$ (middle row) and $E_{\text{lab}} = 0 - 300 \text{ MeV}$ (bottom row) for different values of the momentum-space cutoff Λ . Red solid circles give the results of the SMS $N^4\text{LO}^+$ potentials of this work while solid blue squares show the results of the EMN $N^4\text{LO}^+$ potentials of ref. [8]. The lines are drawn to guide the eyes.

frequently used nonlocal regulator of eq. (2), the employed regularization does not affect the left-hand singularity structure of the potential associated with the pion exchange contributions at any order in the $1/\Lambda$ -expansion and thus manifestly maintains the long-range part of the interaction (provided $\Lambda \sim \Lambda_b$). Moreover, in contrast to the coordinate-space regulator used in refs. [6, 7], our new approach can be straightforwardly applied to regularize three-nucleon forces using the machinery developed in refs. [45, 46].

- Using the new momentum-space regularization scheme for the long-range contributions and employing a non-local Gaussian regulator for the minimal set of independent contact interactions chosen according to eq. (13), we have developed a new family of semilocal chiral potentials up to $N^4\text{LO}$ for the cutoff values of $\Lambda = 350, 400, 450, 500$ and 550 MeV . To this aim, we have fitted the LECs of the contact interactions to the pp and np scattering data of the 2013 Granada database [109], the deuteron binding energy and world average value of the np coherent scattering length. The determined LECs are found to be of a natural size. The stability of the fits and convergence towards a minimum of the χ^2 are greatly improved by the removal of the redundant interactions. Using the values of the πN LECs from ref. [88], obtained by matching chiral

perturbation theory to the solution of the Roy-Steiner equations, we find a continuous improvement in the description of the data from LO to $N^4\text{LO}$. In particular, we confirm the earlier findings of refs. [6, 7] concerning the evidence of the TPEP by observing a strong reduction in the χ^2 when going from NLO to $N^2\text{LO}$ and from $N^3\text{LO}$ to $N^4\text{LO}$. Notice that the TPEP is predicted in a parameter-free way by the chiral symmetry of QCD and its breaking pattern in combination with the empirical information on the πN system.

- At $N^4\text{LO}$, the np data and the low-energy pp data are very well described as reflected by the values of χ^2/datum of order ~ 1 . However, the χ^2/datum increases considerably for pp data above $E_{\text{lab}} \sim 150 \text{ MeV}$. This can be traced back to the high precision of some of the experimental pp data such as especially the CO(67) data set [127], which exceeds the accuracy of our calculations at $N^4\text{LO}$. To describe these data with $\chi^2/\text{datum} \sim 1$ one needs to accurately reproduce the F-wave phase shifts, which are still predicted in a parameter-free way at $N^4\text{LO}$. We have shown that the inclusion of the leading (*i.e.* $N^5\text{LO}$) contact interactions in the $^1\text{F}_3$, $^3\text{F}_2$, $^3\text{F}_3$ and $^3\text{F}_4$ channels, which are also taken into account in the potentials of ref. [8], strongly improves the description of pp data above $E_{\text{lab}} \sim 150 \text{ MeV}$. It is, however, important to

emphasize that the corresponding LECs come out of a natural size, thus showing no signs of enhancement beyond naive dimensional analysis. Consequently, there are no indications that these terms need to be promoted to N⁴LO. Except for the lowest considered cut-off value of $\Lambda = 350$ MeV, where significant regulator artefacts are observed, the resulting N⁴LO⁺ potentials lead to excellent description of both the np and pp scattering data up to $E_{\text{lab}} = 300$ MeV with $\chi^2/\text{datum} \sim 1$, which qualifies them to be regarded as partial wave analyses. We expect the N⁴LO⁺ potentials to be particularly useful for estimating and/or verifying the truncation uncertainty at N⁴LO as they allow one to calculate the contributions of some of the sixth-order terms in the potential to an observable of interest.

- We have performed a comprehensive error analysis of our results. In addition to the truncation uncertainties estimated using the algorithm formulated in refs. [6, 7], see refs. [21–24] for examples of similar approaches to error estimation, we have calculated the covariance matrix for all cutoff values and chiral orders. This allows us to quantify the statistical uncertainty of the LECs accompanying the contact interactions and to propagate statistical errors when calculating observables. To estimate the uncertainty associated with the πN LECs, we have redone the fits using the values of LECs c_i , \bar{d}_i and \bar{e}_i employed in refs. [6, 7] and taken from refs. [68, 102, 103]. We found that using these two different sets of πN LECs has, generally, a moderate impact on the calculated two-nucleon observables. Finally, by varying the maximum fitting energy in the range of $E_{\text{lab}}^{\max} = 220 \dots 300$ MeV, we have verified that our N⁴LO⁺ results are largely insensitive to the choice of E_{lab}^{\max} . We found that the theoretical uncertainty is, in most cases, dominated by the truncation error as conjectured in ref. [6]. However, at N⁴LO and at very low energies, other sources of uncertainty such as especially the one from the πN LECs do become comparable to the truncation error or even dominant. Our determination of the S-wave scattering lengths, effective range parameters and the deuteron properties such as the S state normalization A_S and D/S state ratio η provides new reference values for these observables.
- We have performed a Weinberg eigenvalue analysis of the new chiral potentials to assess their perturbativeness in quantitative terms. For $\Lambda = 350 \dots 500$ MeV, the magnitude of the largest repulsive Weinberg eigenvalues at positive energies does not exceed 1 except for the 1S_0 (3S_1 - 3D_1) channel at NLO (N³LO) for $\Lambda = 500$ MeV, indicating that the interactions are perturbative (except for the deuteron channel at low energies). For the highest considered cutoff value of $\Lambda = 550$ MeV, the potentials become nonperturbative, which is especially true for the N³LO version.

To summarize, we have developed a new family of semilocal momentum-space-regularized chiral NN potentials up to N⁴LO⁺. The new regularization approach is intended to simplify and accelerate applications beyond

the two-nucleon system. Thanks to the removal of the redundant contact interactions at order Q^4 , the new potentials are much softer than the ones of ref. [6, 7], which makes them valuable starting points for many-body applications using *ab initio* methods. At the same time, they provide an outstanding description of the NN data. The precision of our N⁴LO⁺ interactions is considerably higher than that of other available chiral EFT interactions including the ones of ref. [8] at the same chiral order. We attribute this feature primarily to the improved regularization approach which, per construction, maintains the long-range part of the interaction. In fact, the description of the 2013 Granada database below $E_{\text{lab}} = 300$ MeV at N⁴LO⁺ for $\Lambda = 400 \dots 550$ MeV is comparable to that based on the modern high-precision phenomenological potentials including CD-Bonn, Nijm I, II and Reid 93, while our N⁴LO⁺ potential with $\Lambda = 450$ MeV is, actually, more precise than any NN interaction we are aware of. At the same time, the number of adjustable parameters is reduced by $\sim 40\%$ as compared with the high-precision phenomenological potentials, which provides yet another clear evidence of the (parameter-free) chiral 2π exchange. Our results leave little room for a possible improvement of the description of NN scattering data in a complete N⁵LO analysis as proposed in ref. [5], especially given a large number of new contact interactions at this chiral order.

In the future, we plan to apply the new chiral NN interactions, supplemented with the consistently regularized three-body forces and current operators, to study nucleon-deuteron scattering, properties of light and medium-mass nuclei and selected electroweak reactions. Work along these lines is in progress by the LENPIC Collaboration. It would also be interesting to perform a comprehensive analysis of isospin-breaking contributions to the nuclear force and to study the role of the $\Delta(1232)$ resonance, see refs. [9, 12, 90–93] for first steps along this line.

We would like to thank David Entem for providing us with the code to generate matrix elements of the nonlocal potentials of ref. [8] as well as Andreas Ekström, Christian Forssén, Dick Furnstahl, Ashot Gasparian, Dean Lee, Ulf-G. Meißner, Witold Nazarewicz and Enrique Ruiz Arriola for sharing their insights into the considered topics and useful discussions. We also thank Dick Furnstahl, Jambul Gegelia, Heiko Hergert, Ulf-G. Meißner and Igor Strakovsky for helpful comments on the manuscript. This work was supported by BMBF (contract No. 05P2015 - NUSTAR R&D) and by DFG through funds provided to the Sino-German CRC 110 “Symmetries and the Emergence of Structure in QCD” (Grant No. TRR110).

Appendix A. Relations between the different sets of LECs for the contact interactions

As described in sect. 2, we employ the contact-interaction potential $V_{\text{cont}}^{(0)} + V_{\text{cont}}^{(2)} + V_{\text{cont}}^{(4)}$, where $V_{\text{cont}}^{(0)}$ and $V_{\text{cont}}^{(2)}$ are given in eq. (3) while the adopted form of $V_{\text{cont}}^{(4)}$ without redundant terms is specified in eq. (15). After performing partial wave decomposition, the matrix elements can be

written as

$$\begin{aligned} \langle i_S, p' | V_{\text{cont}} | i_S, p \rangle &= \tilde{C}_{i_S} + C_{i_S}(p^2 + p'^2) + D_{i_S}p^2p'^2, \\ \langle i_P, p' | V_{\text{cont}} | i_P, p \rangle &= C_{i_P}pp' + D_{i_P}pp'(p^2 + p'^2), \\ \langle i_D, p' | V_{\text{cont}} | i_D, p \rangle &= D_{i_D}p^2p'^2, \\ \langle {}^3S_1, p' | V_{\text{cont}} | {}^3D_1, p \rangle &= C_{\epsilon 1}p^2 + D_{\epsilon 1}p^2p'^2, \\ \langle {}^3P_2, p' | V_{\text{cont}} | {}^3F_2, p \rangle &= D_{\epsilon 2}p^3p', \end{aligned} \quad (\text{A.1})$$

where $i_S = \{1S0, 3S1\}$, $i_P = \{1P1, 3P0, 3P1, 3P2\}$, $i_D = \{1D2, 3D1, 3D2, 3D3\}$ and

$$\begin{aligned} \tilde{C}_{1S0} &= 4\pi(C_S - 3C_T), \\ \tilde{C}_{3S1} &= 4\pi(C_S + C_T), \\ C_{1S0} &= \pi(4C_1 + C_2 - 12C_3 - 3C_4 - 4C_6 - C_7), \\ C_{3S1} &= \frac{\pi}{3}(12C_1 + 3C_2 + 12C_3 + 3C_4 + 4C_6 + C_7), \\ C_{3P0} &= -\frac{2\pi}{3}(4C_1 - C_2 + 4C_3 - C_4 + 4C_5 - 12C_6 + 3C_7), \\ C_{1P1} &= -\frac{2\pi}{3}(4C_1 - C_2 - 12C_3 + 3C_4 - 4C_6 + C_7), \\ C_{3P1} &= -\frac{2\pi}{3}(4C_1 - C_2 + 4C_3 - C_4 + 2C_5 + 8C_6 - 2C_7), \\ C_{3P2} &= -\frac{2\pi}{3}(4C_1 - C_2 + 4C_3 - C_4 - 2C_5), \\ C_{\epsilon 1} &= \frac{2\sqrt{2}\pi}{3}(4C_6 + C_7), \\ D_{1S0} &= \frac{4\pi}{3}(16D'_1 + D'_2 + 2D'_3 - 3(16D'_4 + D'_5 + 2D'_6) \\ &\quad + 2D'_10 + 2D'_11 - 2D'_12), \\ D_{3S1} &= \frac{4\pi}{9}(48D'_1 + 3(D'_2 + 2D'_3 + 16D'_4 + D'_5 + 2D'_6) \\ &\quad - 2D'_10 - 2D'_11 + 2D'_12), \\ D_{3P0} &= -\frac{\pi}{3}(16D'_1 - D'_2 + 16D'_4 - D'_5 + 8D'_7 + 2D'_8 \\ &\quad + 16D'_9 - 12D'_10 - 4D'_11), \\ D_{1P1} &= -\frac{\pi}{3}(16D'_1 - D'_2 - 48D'_4 + 3D'_5 + 8D'_9 \\ &\quad - 4D'_10 - 4D'_11), \\ D_{3P1} &= -\frac{\pi}{3}(16D'_1 - D'_2 + 16D'_4 - D'_5 + 4D'_7 + D'_8 \\ &\quad - 12D'_9 + 8D'_10 + 4D'_11), \\ D_{3P2} &= -\frac{\pi}{15}(80D'_1 - 5(D'_2 - 16D'_4 + D'_5 + 4D'_7 + D'_8) \\ &\quad - 4D'_9 + 4D'_11), \\ D_{3D1} &= \frac{2\pi}{45}(48D'_1 + 3(D'_2 - 4D'_3 + 16D'_4 + D'_5 - 4D'_6 \\ &\quad + 12D'_7 - 3D'_8) + 20D'_10 + 20D'_11 - 32D'_12), \\ D_{1D2} &= \frac{2\pi}{15}(16D'_1 + D'_2 - 4D'_3 - 48D'_4 - 3D'_5 + 12D'_6 \\ &\quad + 8D'_10 + 8D'_11 + 4D'_12), \\ D_{3D2} &= \frac{2\pi}{15}(16D'_1 + D'_2 - 4D'_3 + 16D'_4 + D'_5 - 4D'_6 \\ &\quad + 4D'_7 - D'_8 - 12D'_10 - 12D'_11 + 8D'_12), \end{aligned}$$

$$\begin{aligned} D_{3D3} &= \frac{2\pi}{15}(16D'_1 + D'_2 - 4D'_3 + 16D'_4 + D'_5 - 4D'_6 \\ &\quad - 8D'_7 + 2D'_8 - 4D'_12), \\ D_{\epsilon 1} &= -\frac{8\sqrt{2}\pi}{9}(2(D'_{10} + D'_{11}) + D'_{12}), \\ D_{\epsilon 2} &= \frac{8\pi}{5}\sqrt{\frac{2}{3}}(D'_9 - D'_{11}). \end{aligned} \quad (\text{A.2})$$

Appendix B. Subtraction constants in the long-range part of the two-pion exchange potential

In this appendix we give the various functions $C_i(\mu)$ which enter the spectral integrals for the TPEP and ensure its regular behavior at short-distances as discussed in sect. 4. To determine $C_i(\mu)$, we make use of the relations between the coordinate- and momentum-space potentials utilizing the conventions of eqs. (23), (24), see e.g. ref. [149]

$$\begin{aligned} X_{C, \Lambda}(r) &= \frac{1}{2\pi^2} \int q^2 dq j_0(qr) X_{C, \Lambda}(q), \\ X_{T, \Lambda}(r) &= -\frac{1}{2\pi^2} \int q^4 dq j_2(qr) X_{T, \Lambda}(q), \\ X_{S, \Lambda}(r) &= \frac{1}{2\pi^2} \int q^2 dq j_0(qr) X_{S, \Lambda}(q) \\ &\quad + \frac{1}{6\pi^2} \int q^4 dq j_0(qr) X_{T, \Lambda}(q), \\ X_{LS, \Lambda}(r) &= -\frac{1}{\pi^2 r} \int q^3 dq j_1(qr) X_{LS, \Lambda}(q), \end{aligned} \quad (\text{B.1})$$

where $X = \{V, W\}$ and $j_i(x)$ are the spherical Bessel functions of the first kind. For the functions $C_i^1(\mu)$ entering the single-subtracted spectral integrals, we obtain the expressions

$$\begin{aligned} C_T^1(\mu) &= -\frac{2\Lambda(15\Lambda^6 - 3\Lambda^4\mu^2 + \Lambda^2\mu^4 - \mu^6) + \sqrt{2\pi}\mu^7 e^{\frac{\mu^2}{2\Lambda^2}} \operatorname{erfc}(\frac{\mu}{\sqrt{2\Lambda}})}{30\Lambda^7}, \\ C_{LS}^1(\mu) &= -\frac{2\Lambda(3\Lambda^4 - \Lambda^2\mu^2 + \mu^4) - \sqrt{2\pi}\mu^5 e^{\frac{\mu^2}{2\Lambda^2}} \operatorname{erfc}(\frac{\mu}{\sqrt{2\Lambda}})}{6\Lambda^5}. \end{aligned} \quad (\text{B.2})$$

Next, the functions $C_i^2(\mu)$ appearing in double-subtracted spectral integrals have the form

see eq. (B.3) on the next page

The functions $C_i^3(\mu)$ entering the triple-subtracted spectral integrals are given by

see eq. (B.4) on the next page

$$\begin{aligned}
C_{C,1}^2(\mu) &= \frac{2\Lambda\mu^2(2\Lambda^4 - 4\Lambda^2\mu^2 - \mu^4) + \sqrt{2\pi}\mu^5 e^{\frac{\mu^2}{2\Lambda^2}} (5\Lambda^2 + \mu^2) \operatorname{erfc}(\frac{\mu}{\sqrt{2\Lambda}})}{4\Lambda^5}, \\
C_{C,2}^2(\mu) &= -\frac{2\Lambda(6\Lambda^6 - 2\Lambda^2\mu^4 - \mu^6) + \sqrt{2\pi}\mu^5 e^{\frac{\mu^2}{2\Lambda^2}} (3\Lambda^2 + \mu^2) \operatorname{erfc}(\frac{\mu}{\sqrt{2\Lambda}})}{12\Lambda^7}, \\
C_{S,1}^2(\mu) &= \frac{2\Lambda\mu^2(2\Lambda^4 - 4\Lambda^2\mu^2 - \mu^4) + \sqrt{2\pi}\mu^5 e^{\frac{\mu^2}{2\Lambda^2}} (5\Lambda^2 + \mu^2) \operatorname{erfc}(\frac{\mu}{\sqrt{2\Lambda}})}{6\Lambda^5}, \\
C_{S,2}^2(\mu) &= -\frac{2\Lambda(15\Lambda^6 - \Lambda^4\mu^2 - 3\Lambda^2\mu^4 - 2\mu^6) + \sqrt{2\pi}\mu^5 e^{\frac{\mu^2}{2\Lambda^2}} (5\Lambda^2 + 2\mu^2) \operatorname{erfc}(\frac{\mu}{\sqrt{2\Lambda}})}{30\Lambda^7}, \\
C_{T,1}^2(\mu) &= -\frac{2\Lambda\mu^2(-30\Lambda^8 + 12\Lambda^6\mu^2 - 6\Lambda^4\mu^4 + 8\Lambda^2\mu^6 + \mu^8) - \sqrt{2\pi}\mu^9 e^{\frac{\mu^2}{2\Lambda^2}} (9\Lambda^2 + \mu^2) \operatorname{erfc}(\frac{\mu}{\sqrt{2\Lambda}})}{60\Lambda^9}, \\
C_{T,2}^2(\mu) &= \frac{2\Lambda(-210\Lambda^{10} + 6\Lambda^6\mu^4 - 4\Lambda^4\mu^6 + 6\Lambda^2\mu^8 + \mu^{10}) - \sqrt{2\pi}\mu^9 e^{\frac{\mu^2}{2\Lambda^2}} (7\Lambda^2 + \mu^2) \operatorname{erfc}(\frac{\mu}{\sqrt{2\Lambda}})}{420\Lambda^{11}}, \\
C_{LS,1}^2(\mu) &= \frac{2\Lambda\mu^2(6\Lambda^6 - 4\Lambda^4\mu^2 + 6\Lambda^2\mu^4 + \mu^6) - \sqrt{2\pi}\mu^7 e^{\frac{\mu^2}{2\Lambda^2}} (7\Lambda^2 + \mu^2) \operatorname{erfc}(\frac{\mu}{\sqrt{2\Lambda}})}{12\Lambda^7}, \\
C_{LS,2}^2(\mu) &= -\frac{2\Lambda(30\Lambda^8 - 2\Lambda^4\mu^4 + 4\Lambda^2\mu^6 + \mu^8) - \sqrt{2\pi}\mu^7 e^{\frac{\mu^2}{2\Lambda^2}} (5\Lambda^2 + \mu^2) \operatorname{erfc}(\frac{\mu}{\sqrt{2\Lambda}})}{60\Lambda^9}. \tag{B.3}
\end{aligned}$$

$$\begin{aligned}
C_{C,1}^3(\mu) &= \frac{2\Lambda\mu^4(-8\Lambda^6 + 24\Lambda^4\mu^2 + 13\Lambda^2\mu^4 + \mu^6) - \sqrt{2\pi}\mu^7 e^{\frac{\mu^2}{2\Lambda^2}} (35\Lambda^4 + 14\Lambda^2\mu^2 + \mu^4) \operatorname{erfc}(\frac{\mu}{\sqrt{2\Lambda}})}{16\Lambda^7}, \\
C_{C,2}^3(\mu) &= -\frac{2\Lambda\mu^2(-12\Lambda^8 + 12\Lambda^4\mu^4 + 11\Lambda^2\mu^6 + \mu^8) - \sqrt{2\pi}\mu^7 e^{\frac{\mu^2}{2\Lambda^2}} (21\Lambda^4 + 12\Lambda^2\mu^2 + \mu^4) \operatorname{erfc}(\frac{\mu}{\sqrt{2\Lambda}})}{24\Lambda^9}, \\
C_{C,3}^3(\mu) &= \frac{2\Lambda(-120\Lambda^{10} + 8\Lambda^4\mu^6 + 9\Lambda^2\mu^8 + \mu^{10}) - \sqrt{2\pi}\mu^7 e^{\frac{\mu^2}{2\Lambda^2}} (15\Lambda^4 + 10\Lambda^2\mu^2 + \mu^4) \operatorname{erfc}(\frac{\mu}{\sqrt{2\Lambda}})}{240\Lambda^{11}}, \\
C_{S,1}^3(\mu) &= \frac{2\Lambda\mu^4(-8\Lambda^6 + 24\Lambda^4\mu^2 + 13\Lambda^2\mu^4 + \mu^6) - \sqrt{2\pi}\mu^7 e^{\frac{\mu^2}{2\Lambda^2}} (35\Lambda^4 + 14\Lambda^2\mu^2 + \mu^4) \operatorname{erfc}(\frac{\mu}{\sqrt{2\Lambda}})}{24\Lambda^7}, \\
C_{S,2}^3(\mu) &= \frac{2\Lambda\mu^2(30\Lambda^8 - 4\Lambda^6\mu^2 - 18\Lambda^4\mu^4 - 21\Lambda^2\mu^6 - 2\mu^8) + \sqrt{2\pi}\mu^7 e^{\frac{\mu^2}{2\Lambda^2}} (35\Lambda^4 + 23\Lambda^2\mu^2 + 2\mu^4) \operatorname{erfc}(\frac{\mu}{\sqrt{2\Lambda}})}{60\Lambda^9}, \\
C_{S,3}^3(\mu) &= \frac{2\Lambda(-420\Lambda^{10} + 4\Lambda^6\mu^4 + 16\Lambda^4\mu^6 + 25\Lambda^2\mu^8 + 3\mu^{10}) - \sqrt{2\pi}\mu^7 e^{\frac{\mu^2}{2\Lambda^2}} (35\Lambda^4 + 28\Lambda^2\mu^2 + 3\mu^4) \operatorname{erfc}(\frac{\mu}{\sqrt{2\Lambda}})}{840\Lambda^{11}}. \tag{B.4}
\end{aligned}$$

Finally, the constants C_1^2 and C_2^2 entering eq. (50) are given by:

$$\begin{aligned}
C_1^2 &= \\
&\quad -\frac{4\Lambda(\Lambda^2 + M_\pi^2) - \sqrt{2\pi}M_\pi e^{\frac{2M_\pi^2}{\Lambda^2}} (5\Lambda^2 + 4M_\pi^2) \operatorname{erfc}(\frac{\sqrt{2}M_\pi}{\Lambda})}{2\Lambda^5}, \\
C_2^2 &= \\
&\quad \frac{2\Lambda(\Lambda^2 + 2M_\pi^2) - \sqrt{2\pi}M_\pi e^{\frac{2M_\pi^2}{\Lambda^2}} (3\Lambda^2 + 4M_\pi^2) \operatorname{erfc}(\frac{\sqrt{2}M_\pi}{\Lambda})}{6\Lambda^7}. \tag{B.5}
\end{aligned}$$

Appendix C. Calculation of scattering observables

In order to perform fits to experimental scattering data, we have to calculate observables from the nuclear potential. We do this by first solving the Lippmann-Schwinger equation for the partial-wave projected T-matrix for the total angular momentum j , total spin s and orbital angular momenta l, l'

$$\begin{aligned}
T_{l'l}^{sj}(p', p; k^2) &= V_{l'l}^{sj}(p', p) + m_N \sum_{l''} \int_0^\infty dq q^2 \\
&\quad \times \frac{V_{l'l''}^{sj}(p', q) T_{l'l''}^{sj}(q, p; k^2)}{k^2 - q^2 + i\epsilon}, \tag{C.1}
\end{aligned}$$

which corresponds to the relativistic Schrödinger equation cast in the nonrelativistic form, see *e.g.* eq. (20) of ref. [6].

Further, $V_{l'l}^{sj}(p', p)$ is the corresponding partial-wave projected NN potential, whose contact-interaction part is explicitly given in sect. 2, while the long-range part is described in detail in sect. 4. The average nucleon mass m_N corresponds to $m_N = 2m_p m_n / (m_n + m_p)$, $m_N = m_p$ or $m_N = m_n$ in the case of np, pp or nn scattering, respectively. Finally, $k \equiv |\vec{k}|$ denotes the relative momentum of the two nucleons in the cms frame, which is related to the kinetic energy of the particles in the laboratory frame via

$$k^2 = \frac{m_p^2 E_{\text{lab}}(E_{\text{lab}} + 2m_n)}{(m_n + m_p)^2 + 2E_{\text{lab}}m_p}, \quad (\text{C.2})$$

for np scattering and via

$$k^2 = \frac{1}{2} m_N E_{\text{lab}} \quad (\text{C.3})$$

for pp (nn) scattering. The on-shell partial-wave S-Matrix can then be obtained as

$$S_{l'l}^{sj}(k) = \delta_{l'l} - i\pi k m_N T_{l'l}^{sj}(k, k, k^2). \quad (\text{C.4})$$

The partial-wave S-matrix needs to be modified to account for e.m. interactions as explained in sect. 5. In particular, for pp scattering, we first calculate $S_{l'l}^{sj}$ with respect to Coulomb functions. The resulting S-matrix elements are then corrected in the 1S_0 channel according to eq. (77) and finally multiplied with the appropriate e.m. interaction partial wave S-matrices as given in eq. (76). After the adjustment for the e.m. interactions, all partial-wave S-matrices with total angular momentum $j \leq 20$ are summed up in the singlet-triplet representation of the scattering amplitude according to

$$\begin{aligned} M_{m'_s, m_s}^s &= \frac{1}{iq} \sum_{j l' l} C(l', s, j; m_s - m'_s, m'_s, m_s) \\ &\times Y_{l'(m'_s - m_s)}(\hat{q}) i^{l-l'} \left(S_{l'l}^{js} - \delta_{l'l} \right) \\ &\times C(l, s, j; 0, m_s, m_s) \sqrt{\pi(2l+1)} \\ &\times [1 - (-1)^{l+s+t}]. \end{aligned} \quad (\text{C.5})$$

Here, t denotes the total isospin, $C(j_1, j_2, j_3; m_1, m_2, m_3)$ are Clebsch-Gordan coefficients while $Y_{lm}(\hat{q})$ are the spherical harmonics. The nuclear scattering amplitude is then combined with the amplitudes of the long-range electromagnetic interactions given in sect. 5. We express the full scattering amplitude M in terms of the Wolfenstein-like amplitudes a, \dots, f , often called Saclay amplitudes, whose definition and relation to the Singlet-Triplet amplitude are given *e.g.* in ref. [97]. Expressions for observables in terms of the Saclay amplitudes can be found in table III of [97], where we make use of those expressions with the rotation angles $\alpha = 0$ and $\beta = \pi/2$, corresponding to the non-relativistic limit and thereby neglecting Wigner spin rotations.

Appendix D. Results for np and pp phase shifts and mixing angles

In this appendix we collect the results for the pp and np phase shifts and mixing angles from our partial wave anal-

ysis, which are given in tables 12–14 and 15–19, respectively. We restrict ourselves to the highest considered order (N^4LO^+) and to the intermediate cutoff $\Lambda = 450$ MeV which yields the best description of the scattering data from the 2013 Granada database below $E_{\text{lab}} = 300$ MeV. Furthermore, we only show the results for the channels involving contact interactions that have been fitted to the data. Except for F-waves, the truncation uncertainties correspond to N^4LO and have been estimated using the algorithm described in sect. 7.5.2 without relying on the explicit knowledge of the N^4LO^+ contributions. Motivated by the findings of ref. [124], see also [131] for a related discussion, we have assumed a slightly higher value for the breakdown scale of $\Lambda_b = 650$ MeV as compared with $\Lambda_b = 600$ MeV adopted in refs. [6, 7]. Since our results for F-waves take into account the order- Q^6 contact interactions, we show the N^5LO truncation error for the F-wave phase shifts.

In order to verify the consistency of our approach to uncertainty quantifications, we have performed several tests. Specifically, by regarding our predicted values for the phase shifts and mixing angles from tables 15–19 along with the corresponding statistical and truncation uncertainties as “synthetic data”, we have followed the approach similar to that of ref. [6] and calculated the $\tilde{\chi}^2/\text{datum}$ for their reproduction using some of our potentials. The statistical and truncation errors listed in tables 15–19 were then added in quadrature to define the corresponding “synthetic error bars”¹⁹. To avoid a possible confusion with the χ^2 for the description of experimental data considered in the main part of the manuscript, we use a symbol $\tilde{\chi}^2$ for such an approach. Further, we restrict ourselves to np phase shifts and mixing angles and to the energies of $E_{\text{lab}} = 1, 5, 10, 25, 50, 100, 150, 200, 250$ and 300 MeV.

To test our estimated N^4LO truncation errors in the S-, P- and D-waves and the mixing angles $\epsilon_{1,2,3}$, we have calculated the corresponding $\tilde{\chi}^2/\text{datum}$ for the reproduction of the “synthetic data” using the N^4LO potential with the same cutoff value of $\Lambda = 450$ MeV, which turns out to be $\tilde{\chi}^2/\text{datum} = 1.04$. Notice that the number of data is determined by the number of channels and energies. To also verify the consistency of the estimated N^5LO truncation uncertainties in F-waves, we have used our N^4LO^+ potentials for different cutoff choices. We find $\tilde{\chi}^2/\text{datum} = 0.70$ ($\tilde{\chi}^2/\text{datum} = 0.50$) for the cutoff choice of $\Lambda = 400$ MeV ($\Lambda = 500$ MeV) for the reproduction of our “synthetic data” in the S-, P-, D and F-waves and the mixing angles $\epsilon_{1,2,3}$. Notice that we do not include the theoretical uncertainty corresponding to these potentials when calculating the $\tilde{\chi}^2$. For $\Lambda = 550$ MeV, we find a larger value of $\tilde{\chi}^2/\text{datum} = 2.29$, which is consistent with the larger truncation errors for this cutoff choice.

We believe that the estimated errors provide a realistic account of the theoretical uncertainty of our calculations.

¹⁹ Notice, however, that the truncation errors at different energies are expected to be correlated with each other, so that the interpretation of the corresponding $\tilde{\chi}^2/\text{datum}$ values should be taken with care.

Table 12. Proton-proton S- and P-wave phase shifts in degrees as obtained at N^4LO^+ for the cutoff $\Lambda = 450$ MeV as a function of the laboratory energy E_{lab} (in MeV). The phase shifts are calculated with respect to Coulomb functions. The first uncertainty is statistical, the second one corresponds to the truncation error at N^4LO , the third one estimates the sensitivity to the πN LECs while the last uncertainty reflects the sensitivity to the choice of the maximum energy in the fits as explained in the text. The truncation errors are estimated assuming the breakdown scale of $\Lambda_b = 650$ MeV. Errors smaller than 0.005° are not shown.

E_{lab}	1S_0	3P_0	3P_1	3P_2
1	$32.79 {}^{(+1)}_{(-0)}(0)(0)(0)$	0.14	-0.08	0.01
5	$54.88 {}^{(+1)}_{(-1)}(2)(4)(0)$	1.61	-0.89	$0.22 {}^{(+0)}_{(-0)}(0)(1)(0)$
10	$55.26 {}^{(+2)}_{(-2)}(2)(6)(1)$	$3.81 {}^{(+1)}_{(-1)}(1)(1)(1)$	$-2.04 {}^{(+0)}_{(-0)}(0)(1)(0)$	$0.67 {}^{(+0)}_{(-0)}(0)(2)(0)$
25	$48.75 {}^{(+4)}_{(-3)}(2)(6)(1)$	$8.77 {}^{(+3)}_{(-3)}(2)(1)(2)$	$-4.88 {}^{(+1)}_{(-1)}(0)(2)(1)$	$2.51 {}^{(+0)}_{(-0)}(1)(5)(0)$
50	$39.05 {}^{(+5)}_{(-5)}(4)(1)(2)$	$11.74 {}^{(+5)}_{(-5)}(2)(4)(3)$	$-8.27 {}^{(+2)}_{(-2)}(1)(1)(3)$	$5.82 {}^{(+1)}_{(-1)}(1)(3)(0)$
100	$25.18 {}^{(+6)}_{(-6)}(23)(12)(4)$	$9.61 {}^{(+7)}_{(-7)}(14)(11)(1)$	$-13.32 {}^{(+3)}_{(-3)}(8)(4)(4)$	$10.88 {}^{(+2)}_{(-2)}(12)(10)(1)$
150	$15.11 {}^{(+8)}_{(-8)}(62)(20)(6)$	$4.80 {}^{(+8)}_{(-8)}(45)(9)(8)$	$-17.54 {}^{(+5)}_{(-4)}(27)(5)(1)$	$13.90 {}^{(+3)}_{(-3)}(37)(13)(2)$
200	$7.19 {}^{(+12)}_{(-12)}(1.30)(23)(8)$	$-0.20 {}^{(+11)}_{(-10)}(1.00)(3)(17)$	$-21.18 {}^{(+8)}_{(-8)}(58)(5)(4)$	$15.63 {}^{(+5)}_{(-5)}(75)(1)(4)$
250	$0.72 {}^{(+18)}_{(-18)}(2.10)(21)(11)$	$-4.79 {}^{(+16)}_{(-16)}(1.80)(22)(29)$	$-24.26 {}^{(+15)}_{(-14)}(99)(25)(12)$	$16.58 {}^{(+7)}_{(-7)}(1.20)(22)(5)$
300	$-4.64 {}^{(+26)}_{(-25)}(3.20)(13)(13)$	$-8.79 {}^{(+23)}_{(-22)}(2.80)(48)(42)$	$-26.74 {}^{(+23)}_{(-22)}(1.50)(57)(22)$	$17.03 {}^{(+8)}_{(-8)}(1.70)(49)(6)$

Table 13. Proton-proton 1D_2 phase shifts and the mixing angle ϵ_2 in degrees as obtained at N^4LO^+ for the cutoff $\Lambda = 450$ MeV as function of the laboratory energy E_{lab} (in MeV). For the notation see table 12.

E_{lab}	1D_2	ϵ_2
1	0.00	0.00
5	0.04	-0.05
10	0.17	-0.20
25	$0.70 {}^{(+0)}_{(-0)}(0)(1)(0)$	-0.81
50	$1.69 {}^{(+0)}_{(-0)}(1)(3)(0)$	-1.70
100	$3.72 {}^{(+1)}_{(-1)}(7)(4)(1)$	$-2.64 {}^{(+1)}_{(-1)}(3)(1)(0)$
150	$5.61 {}^{(+2)}_{(-2)}(24)(3)(2)$	$-2.89 {}^{(+2)}_{(-2)}(10)(3)(0)$
200	$7.19 {}^{(+4)}_{(-4)}(55)(16)(3)$	$-2.81 {}^{(+3)}_{(-3)}(21)(4)(1)$
250	$8.42 {}^{(+5)}_{(-5)}(97)(30)(4)$	$-2.58 {}^{(+4)}_{(-4)}(34)(3)(1)$
300	$9.33 {}^{(+6)}_{(-6)}(1.50)(42)(5)$	$-2.29 {}^{(+4)}_{(-4)}(47)(2)(1)$

Table 14. Proton-proton F-wave phase shifts in degrees as obtained at N^4LO^+ for the cutoff $\Lambda = 450$ MeV as function of the laboratory energy E_{lab} (in MeV). The second uncertainty corresponds to the N^5LO truncation error. For the remaining notation see table 12.

E_{lab}	3F_2	3F_3	3F_4
1	0.00	0.00	0.00
5	0.00	-0.01	0.00
10	0.01	-0.03	0.00
25	0.11	-0.23	0.02
50	0.34 $(^{+0})_{(-0)}$ (0)(1)(0)	-0.68	0.12 $(^{+0})_{(-0)}$ (0)(1)(0)
100	0.81 $(^{+1})_{(-1)}$ (4)(2)(1)	-1.47 $(^{+1})_{(-1)}$ (2)(2)(0)	0.51 $(^{+0})_{(-0)}$ (1)(2)(1)
150	1.14 $(^{+2})_{(-2)}$ (15)(3)(3)	-2.03 $(^{+2})_{(-2)}$ (8)(2)(1)	1.06 $(^{+1})_{(-1)}$ (4)(3)(3)
200	1.29 $(^{+4})_{(-4)}$ (39)(2)(6)	-2.41 $(^{+5})_{(-5)}$ (19)(1)(2)	1.70 $(^{+3})_{(-3)}$ (10)(1)(7)
250	1.26 $(^{+7})_{(-7)}$ (74)(1)(10)	-2.68 $(^{+9})_{(-9)}$ (38)(6)(3)	2.37 $(^{+5})_{(-4)}$ (20)(4)(12)
300	1.08 $(^{+11})_{(-11)}$ (1.20)(6)(14)	-2.87 $(^{+14})_{(-14)}$ (64)(14)(5)	3.02 $(^{+7})_{(-7)}$ (33)(11)(18)

Table 15. Neutron-proton S-wave phase shifts in degrees as obtained at N^4LO^+ for the cutoff $\Lambda = 450$ MeV as function of the laboratory energy E_{lab} (in MeV). For the notation see table 12.

E_{lab}	1S_0	3S_1
1	62.02 $(^{+5})_{(-1)}$ (2)(5)(4)	147.74 $(^{+2})_{(-1)}$ (1)(1)(0)
5	63.51 $(^{+6})_{(-4)}$ (4)(13)(11)	118.17 $(^{+3})_{(-2)}$ (1)(2)(1)
10	59.78 $(^{+8})_{(-6)}$ (6)(19)(17)	102.59 $(^{+4})_{(-2)}$ (1)(2)(1)
25	50.58 $(^{+13})_{(-12)}$ (9)(28)(29)	80.57 $(^{+5})_{(-4)}$ (1)(1)(2)
50	39.95 $(^{+19})_{(-18)}$ (11)(36)(45)	62.64 $(^{+6})_{(-6)}$ (3)(8)(2)
100	25.67 $(^{+29})_{(-28)}$ (23)(43)(70)	42.99 $(^{+8})_{(-8)}$ (14)(15)(3)
150	15.52 $(^{+36})_{(-35)}$ (62)(51)(91)	30.50 $(^{+12})_{(-11)}$ (40)(10)(6)
200	7.59 $(^{+43})_{(-42)}$ (1.20)(63)(1.10)	21.20 $(^{+17})_{(-16)}$ (86)(7)(8)
250	1.14 $(^{+50})_{(-49)}$ (2.10)(78)(1.20)	13.83 $(^{+24})_{(-23)}$ (1.60)(35)(13)
300	-4.19 $(^{+57})_{(-56)}$ (3.20)(97)(1.40)	7.80 $(^{+31})_{(-30)}$ (2.50)(70)(19)

Table 16. Neutron-proton P-wave phase shifts in degrees as obtained at N^4LO^+ for the cutoff $\Lambda = 450$ MeV as function of the laboratory energy E_{lab} (in MeV). For the notation see table 15.

E_{lab}	3P_0	1P_1	3P_1	3P_2
1	0.18	-0.19	-0.11	0.02
5	1.65 $(^{+0})_{(-0)}(0)(1)(0)$	-1.52 $(^{+0})_{(-0)}(0)(2)(1)$	-0.92	0.26 $(^{+0})_{(-0)}(0)(1)(0)$
10	3.72 $(^{+1})_{(-1)}(1)(1)(1)$	-3.11 $(^{+1})_{(-1)}(1)(4)(2)$	-2.03 $(^{+0})_{(-0)}(0)(1)(0)$	0.73 $(^{+0})_{(-0)}(1)(2)(0)$
25	8.33 $(^{+3})_{(-3)}(2)(1)(2)$	-6.48 $(^{+3})_{(-3)}(2)(12)(8)$	-4.81 $(^{+1})_{(-1)}(0)(2)(1)$	2.60 $(^{+1})_{(-1)}(1)(5)(0)$
50	11.02 $(^{+5})_{(-5)}(2)(4)(3)$	-9.92 $(^{+7})_{(-7)}(4)(21)(16)$	-8.19 $(^{+2})_{(-2)}(1)(1)(3)$	5.90 $(^{+1})_{(-1)}(1)(3)(0)$
100	8.76 $(^{+7})_{(-7)}(14)(11)(1)$	-14.66 $(^{+14})_{(-13)}(16)(15)(26)$	-13.30 $(^{+3})_{(-3)}(8)(5)(4)$	10.94 $(^{+2})_{(-2)}(12)(11)(1)$
150	3.95 $(^{+8})_{(-8)}(46)(9)(8)$	-18.56 $(^{+19})_{(-18)}(45)(14)(19)$	-17.56 $(^{+5})_{(-5)}(28)(5)(1)$	13.92 $(^{+3})_{(-3)}(37)(13)(2)$
200	-1.02 $(^{+11})_{(-11)}(1.00)(3)(18)$	-21.88 $(^{+25})_{(-24)}(94)(56)(26)$	-21.24 $(^{+9})_{(-8)}(59)(6)(4)$	15.63 $(^{+5})_{(-5)}(75)(0)(4)$
250	-5.57 $(^{+16})_{(-16)}(1.80)(23)(29)$	-24.60 $(^{+36})_{(-34)}(1.70)(1.10)(43)$	-24.33 $(^{+15})_{(-15)}(1.00)(27)(12)$	16.57 $(^{+7})_{(-7)}(1.20)(23)(5)$
300	-9.53 $(^{+23})_{(-23)}(2.90)(49)(42)$	-26.66 $(^{+54})_{(-50)}(2.60)(1.60)(82)$	-26.81 $(^{+24})_{(-23)}(1.50)(60)(23)$	17.01 $(^{+8})_{(-8)}(1.70)(51)(6)$

Table 17. Neutron-proton D-wave phase shifts in degrees at N^4LO^+ for the cutoff $\Lambda = 450$ MeV as function of the laboratory energy E_{lab} (in MeV). For the notation see table 15.

E_{lab}	3D_1	1D_2	3D_2	3D_3
1	-0.01	0.00	0.01	0.00
5	-0.18	0.04	0.22	0.00
10	-0.68 $(^{+0})_{(-0)}(0)(1)(0)$	0.16	0.85	0.00
25	-2.82 $(^{+1})_{(-1)}(0)(2)(1)$	0.68 $(^{+0})_{(-0)}(0)(1)(0)$	3.72 $(^{+0})_{(-0)}(0)(3)(0)$	0.03 $(^{+0})_{(-0)}(1)(2)(1)$
50	-6.47 $(^{+2})_{(-2)}(1)(2)(1)$	1.69 $(^{+0})_{(-0)}(1)(3)(0)$	8.97 $(^{+1})_{(-1)}(1)(12)(1)$	0.24 $(^{+1})_{(-1)}(3)(7)(3)$
100	-12.28 $(^{+4})_{(-4)}(4)(3)(2)$	3.79 $(^{+1})_{(-1)}(7)(4)(1)$	17.23 $(^{+6})_{(-6)}(8)(25)(4)$	1.20 $(^{+4})_{(-4)}(16)(13)(14)$
150	-16.47 $(^{+8})_{(-8)}(10)(8)(10)$	5.73 $(^{+2})_{(-2)}(25)(3)(2)$	22.12 $(^{+10})_{(-10)}(25)(20)(8)$	2.42 $(^{+8})_{(-8)}(37)(7)(31)$
200	-19.57 $(^{+16})_{(-15)}(20)(13)(22)$	7.33 $(^{+4})_{(-4)}(56)(16)(3)$	24.65 $(^{+14})_{(-14)}(50)(3)(11)$	3.56 $(^{+13})_{(-13)}(64)(11)(51)$
250	-21.88 $(^{+25})_{(-24)}(43)(16)(37)$	8.56 $(^{+5})_{(-5)}(98)(31)(4)$	25.72 $(^{+17})_{(-17)}(81)(16)(13)$	4.51 $(^{+18})_{(-17)}(1.00)(36)(69)$
300	-23.57 $(^{+38})_{(-35)}(82)(18)(55)$	9.47 $(^{+6})_{(-6)}(1.50)(43)(5)$	25.94 $(^{+19})_{(-19)}(1.20)(32)(15)$	5.22 $(^{+22})_{(-21)}(1.40)(61)(85)$

Table 18. Neutron-proton F-wave phase shifts in degrees as obtained at N^4LO^+ for the cutoff $\Lambda = 450$ MeV as function of the laboratory energy E_{lab} (in MeV). The second uncertainty corresponds to the N^5LO truncation error. For the remaining notation see table 15.

E_{lab}	3F_2	1F_3	3F_3	3F_4
1	0.00	0.00	0.00	0.00
5	0.00	-0.01	0.00	0.00
10	0.01	-0.07	-0.03	0.00
25	0.09	-0.42	-0.20	0.02
50	0.31 $(^{+0})_{(-0)}(0)(1)(0)$	-1.12 $(^{+0})_{(-0)}(0)(1)(1)$	-0.61	0.11 $(^{+0})_{(-0)}(0)(1)(0)$
100	0.75 $(^{+1})_{(-1)}(4)(2)(1)$	-2.18 $(^{+1})_{(-1)}(3)(3)(5)$	-1.36 $(^{+1})_{(-1)}(2)(2)(0)$	0.48 $(^{+0})_{(-0)}(1)(2)(1)$
150	1.07 $(^{+2})_{(-2)}(16)(3)(3)$	-2.86 $(^{+4})_{(-4)}(12)(5)(17)$	-1.89 $(^{+2})_{(-2)}(8)(2)(1)$	1.03 $(^{+1})_{(-1)}(4)(3)(3)$
200	1.20 $(^{+4})_{(-4)}(39)(2)(6)$	-3.36 $(^{+8})_{(-8)}(31)(5)(38)$	-2.27 $(^{+5})_{(-5)}(20)(1)(2)$	1.66 $(^{+3})_{(-3)}(10)(1)(7)$
250	1.16 $(^{+7})_{(-7)}(75)(1)(10)$	-3.80 $(^{+14})_{(-14)}(61)(3)(66)$	-2.54 $(^{+9})_{(-9)}(39)(7)(3)$	2.32 $(^{+5})_{(-5)}(20)(4)(12)$
300	0.96 $(^{+11})_{(-11)}(1.20)(6)(15)$	-4.21 $(^{+21})_{(-20)}(1.00)(2)(1.00)$	-2.73 $(^{+14})_{(-14)}(65)(15)(5)$	2.97 $(^{+7})_{(-7)}(34)(12)(18)$

Table 19. Neutron-proton mixing angles ϵ_1 , ϵ_2 and ϵ_3 as obtained at N^4LO^+ for the cutoff $\Lambda = 450$ MeV as function of the laboratory energy E_{lab} (in MeV). For the notation see table 15.

E_{lab}	ϵ_1	ϵ_2	ϵ_3
1	0.11	0.00	0.00
5	0.67 $(^{+1})_{(-1)}(0)(2)(0)$	-0.05	0.01
10	1.16 $(^{+1})_{(-1)}(1)(6)(1)$	-0.18	0.08
25	1.77 $(^{+3})_{(-3)}(1)(14)(3)$	-0.75	0.55
50	2.05 $(^{+5})_{(-5)}(3)(24)(5)$	-1.61	1.61
100	2.29 $(^{+7})_{(-7)}(8)(31)(9)$	-2.55 $(^{+1})_{(-1)}(3)(1)(0)$	3.46 $(^{+0})_{(-0)}(1)(1)(0)$
150	2.54 $(^{+10})_{(-10)}(14)(24)(11)$	-2.82 $(^{+2})_{(-2)}(11)(3)(0)$	4.71 $(^{+0})_{(-0)}(2)(2)(0)$
200	2.81 $(^{+15})_{(-15)}(29)(6)(11)$	-2.76 $(^{+3})_{(-3)}(21)(4)(1)$	5.47 $(^{+0})_{(-0)}(6)(2)(1)$
250	3.06 $(^{+24})_{(-24)}(52)(21)(14)$	-2.55 $(^{+4})_{(-4)}(34)(3)(1)$	5.84 $(^{+1})_{(-1)}(13)(1)(3)$
300	3.26 $(^{+35})_{(-36)}(82)(53)(23)$	-2.27 $(^{+4})_{(-4)}(47)(2)(1)$	5.93 $(^{+2})_{(-2)}(24)(1)(6)$

It should, however, be emphasized that we do not estimate errors from the uncertainty in the πN coupling constant and its possible charge dependence. Also our incomplete treatment of isospin-breaking corrections may potentially affect the results for the phase shifts and mixing angles at low energy.

References

1. E. Epelbaum, H.W. Hammer, U.-G. Meißner, Rev. Mod. Phys. **81**, 1773 (2009).
2. R. Machleidt, D.R. Entem, Phys. Rep. **503**, 1 (2011).
3. E. Epelbaum, U.-G. Meißner, Annu. Rev. Nucl. Part. Sci. **62**, 159 (2012).
4. D.R. Entem, N. Kaiser, R. Machleidt, Y. Nosyk, Phys. Rev. C **91**, 014002 (2015).
5. D.R. Entem, N. Kaiser, R. Machleidt, Y. Nosyk, Phys. Rev. C **92**, 064001 (2015).
6. E. Epelbaum, H. Krebs, U.-G. Meißner, Eur. Phys. J. A **51**, 53 (2015).
7. E. Epelbaum, H. Krebs, U.-G. Meißner, Phys. Rev. Lett. **115**, 122301 (2015).
8. D.R. Entem, R. Machleidt, Y. Nosyk, Phys. Rev. C **96**, 024004 (2017).
9. M. Piarulli, L. Girlanda, R. Schiavilla, R. Navarro Perez, J.E. Amaro, E. Ruiz Arriola, Phys. Rev. C **91**, 024003 (2015).
10. B.D. Carlsson *et al.*, Phys. Rev. X **6**, 011019 (2016).
11. M. Piarulli *et al.*, Phys. Rev. C **94**, 054007 (2016).

12. A. Ekström, G. Hagen, T.D. Morris, T. Papenbrock, P.D. Schwartz, arXiv:1707.09028 [nucl-th].
13. V. Baru, E. Epelbaum, C. Hanhart, M. Hoferichter, A.E. Kudryavtsev, D.R. Phillips, Eur. Phys. J. A **48**, 69 (2012).
14. A. Gezerlis, I. Tews, E. Epelbaum, S. Gandolfi, K. Hebeler, A. Nogga, A. Schwenk, Phys. Rev. Lett. **111**, 032501 (2013).
15. A. Gezerlis, I. Tews, E. Epelbaum, M. Freunek, S. Gandolfi, K. Hebeler, A. Nogga, A. Schwenk, Phys. Rev. C **90**, 054323 (2014).
16. E. Epelbaum, W. Glöckle, U.G. Meißner, Nucl. Phys. A **747**, 362 (2005).
17. D.R. Entem, R. Machleidt, Phys. Rev. C **68**, 041001 (2003).
18. E. Epelbaum, W. Glöckle, U.-G. Meißner, Eur. Phys. J. A **19**, 125 (2004).
19. E. Epelbaum, W. Glöckle, U.-G. Meißner, Eur. Phys. J. A **19**, 401 (2004).
20. V.G.J. Stoks, R.A.M. Klomp, M.C.M. Rentmeester, J.J. de Swart, Phys. Rev. C **48**, 792 (1993).
21. D.R. Phillips, G. Rupak, M.J. Savage, Phys. Lett. B **473**, 209 (2000).
22. P.F. Bedaque, H.W. Giesshammer, Nucl. Phys. A **671**, 357 (2000).
23. H.W. Giesshammer, J.A. McGovern, D.R. Phillips, G. Feldman, Prog. Part. Nucl. Phys. **67**, 841 (2012).
24. J.A. McGovern, D.R. Phillips, H.W. Giesshammer, Eur. Phys. J. A **49**, 12 (2013).
25. LENPIC Collaboration (S. Binder *et al.*), Phys. Rev. C **93**, 044002 (2016).
26. P. Maris *et al.*, EPJ Web of Conferences **113**, 04015 (2016).
27. R. Skibiski *et al.*, Phys. Rev. C **93**, 064002 (2016).
28. R. Skibiski *et al.*, Few Body Syst. **58**, 28 (2017).
29. J. Hu, Y. Zhang, E. Epelbaum, U.-G. Meißner, J. Meng, Phys. Rev. C **96**, 034307 (2017).
30. M. Vorabbi, P. Finelli, C. Giusti, Phys. Rev. C **96**, 044001 (2017).
31. S. Weinberg, Nucl. Phys. B **363**, 3 (1991).
32. U. van Kolck, Phys. Rev. C **49**, 2932 (1994).
33. E. Epelbaum, A. Nogga, W. Glöckle, H. Kamada, U.-G. Meißner, H. Witala, Phys. Rev. C **66**, 064001 (2002).
34. V. Bernard, E. Epelbaum, H. Krebs, U.G. Meißner, Phys. Rev. C **77**, 064004 (2008).
35. S. Ishikawa, M.R. Robilotta, Phys. Rev. C **76**, 014006 (2007).
36. V. Bernard, E. Epelbaum, H. Krebs, U.-G. Meißner, Phys. Rev. C **84**, 054001 (2011).
37. S. Kölling, E. Epelbaum, H. Krebs, U.-G. Meißner, Phys. Rev. C **80**, 045502 (2009).
38. S. Kölling, E. Epelbaum, H. Krebs, U.-G. Meißner, Phys. Rev. C **84**, 054008 (2011).
39. H. Krebs, E. Epelbaum, U.-G. Meißner, Ann. Phys. **378**, 317 (2017).
40. S. Pastore, L. Girlanda, R. Schiavilla, M. Viviani, R.B. Wiringa, Phys. Rev. C **80**, 034004 (2009).
41. M. Piarulli, L. Girlanda, L.E. Marcucci, S. Pastore, R. Schiavilla, M. Viviani, Phys. Rev. C **87**, 014006 (2013).
42. A. Baroni, L. Girlanda, S. Pastore, R. Schiavilla, M. Viviani, Phys. Rev. C **93**, 015501 (2016) **93**, 049902(E) (2016) **95**, 059901(E) (2017).
43. J. Golak, R. Skibinski, arXiv:1705.01530 [nucl-th].
44. A. Ekström, B.D. Carlsson, K.A. Wendt, C. Forssn, M. Hjorth-Jensen, R. Machleidt, S.M. Wild, J. Phys. G **42**, 034003 (2015).
45. J. Golak *et al.*, Eur. Phys. J. A **43**, 241 (2010).
46. K. Hebeler, H. Krebs, E. Epelbaum, J. Golak, R. Skibinski, Phys. Rev. C **91**, 044001 (2015).
47. K. Hebeler, H. Krebs, A. Nogga, E. Epelbaum, in preparation.
48. A.A. Slavnov, Nucl. Phys. B **31**, 301 (1971).
49. D. Djukanovic, M.R. Schindler, J. Gegelia, S. Scherer, Phys. Rev. D **72**, 045002 (2005).
50. D. Djukanovic, J. Gegelia, S. Scherer, M.R. Schindler, Few Body Syst. **41**, 141 (2007).
51. J. Behrendt, E. Epelbaum, J. Gegelia, U.-G. Meißner, A. Nogga, Eur. Phys. J. A **52**, 296 (2016).
52. M. Pavon Valderrama, Phys. Rev. C **84**, 064002 (2011) arXiv:1108.0872 [nucl-th].
53. B. Long, C.J. Yang, Phys. Rev. C **85**, 034002 (2012).
54. M. Pavon Valderrama, M. Snchez Snchez, C.J. Yang, B. Long, J. Carbonell, U. van Kolck, Phys. Rev. C **95**, 054001 (2017).
55. E. Epelbaum, J. Gegelia, Eur. Phys. J. A **41**, 341 (2009).
56. E. Epelbaum, J. Gegelia, Phys. Lett. B **716**, 338 (2012).
57. V.G. Kadyshevsky, Nucl. Phys. B **6**, 125 (1968).
58. E. Epelbaum, A.M. Gasparyan, J. Gegelia, M.R. Schindler, Eur. Phys. J. A **50**, 51 (2014).
59. E. Epelbaum, A.M. Gasparyan, J. Gegelia, H. Krebs, Eur. Phys. J. A **51**, 71 (2015).
60. K.W. Li, X.L. Ren, L.S. Geng, B. Long, Phys. Rev. D **94**, 014029 (2016).
61. S. Wesolowski, *Bayesian methods for effective field theories*, talk at the INT Program INT-16-2a on Bayesian Methods in Nuclear Physics, INT Seattle, USA, June 13 - July 8, 2016.
62. H.W. Hammer, R.J. Furnstahl, Nucl. Phys. A **678**, 277 (2000).
63. S.R. Beane, M.J. Savage, Nucl. Phys. A **694**, 511 (2001).
64. R.J. Furnstahl, H.W. Hammer, N. Tifessa, Nucl. Phys. A **689**, 846 (2001).
65. E. Epelbaum, W. Glöckle, U.G. Meißner, Nucl. Phys. A **637**, 107 (1998).
66. E. Epelbaum, W. Glöckle, U.G. Meißner, Nucl. Phys. A **671**, 295 (2000).
67. E. Epelbaum, Eur. Phys. J. A **34**, 197 (2007).
68. H. Krebs, A. Gasparyan, E. Epelbaum, Phys. Rev. C **85**, 054006 (2012).
69. H. Krebs, A. Gasparyan, E. Epelbaum, Phys. Rev. C **87**, 054007 (2013).
70. R. Roth, H. Hergert, P. Papakonstantinou, T. Neff, H. Feldmeier, Phys. Rev. C **72**, 034002 (2005).
71. H. Hergert, R. Roth, Phys. Rev. C **75**, 051001 (2007).
72. S. Weinberg, Phys. Rev. **130**, 776 (1963).
73. S. Weinberg, Phys. Rev. **131**, 440 (1963).
74. J. Hoppe, C. Drischler, R.J. Furnstahl, K. Hebeler, A. Schwenk, Phys. Rev. C **96**, 054002 (2017).
75. T.A. Rijken, Ann. Phys. **208**, 253 (1991).
76. U. van Kolck, M.C.M. Rentmeester, J.L. Friar, J.T. Goldman, J.J. de Swart, Phys. Rev. Lett. **80**, 4386 (1998).
77. J.L. Friar, U. van Kolck, Phys. Rev. C **60**, 034006 (1999).
78. M. Walzl, U.G. Meißner, E. Epelbaum, Nucl. Phys. A **693**, 663 (2001).
79. J.L. Friar, U. van Kolck, G.L. Payne, S.A. Coon, Phys. Rev. C **68**, 024003 (2003).

80. E. Epelbaum, U.G. Meißner, Phys. Rev. C **72**, 044001 (2005).
81. N. Kaiser, Phys. Rev. C **73**, 064003 (2006).
82. J.J. de Swart, M.C.M. Rentmeester, R.G.E. Timmermans, PiN Newslett. **13**, 96 (1997).
83. S. Weinberg, Phys. Lett. B **251**, 288 (1990).
84. C. Ordóñez, L. Ray, U. van Kolck, Phys. Rev. C **53**, 2086 (1996).
85. N. Kaiser, R. Brockmann, W. Weise, Nucl. Phys. A **625**, 758 (1997).
86. N. Kaiser, Phys. Rev. C **64**, 057001 (2001).
87. J.L. Friar, Phys. Rev. C **60**, 034002 (1999).
88. M. Hoferichter, J. Ruiz de Elvira, B. Kubis, U.-G. Meißner, Phys. Rev. Lett. **115**, 192301 (2015).
89. D.B. Kaplan, A.V. Manohar, Phys. Rev. C **56**, 76 (1997).
90. N. Kaiser, S. Gerstendorfer, W. Weise, Nucl. Phys. A **637**, 395 (1998).
91. H. Krebs, E. Epelbaum, U.-G. Meißner, Eur. Phys. J. A **32**, 127 (2007).
92. E. Epelbaum, H. Krebs, U.-G. Meißner, Nucl. Phys. A **806**, 65 (2008).
93. H. Krebs, A.M. Gasparyan, E. Epelbaum, arXiv:1803.09613 [nucl-th].
94. G.J.M. Austen, J.J. de Swart, Phys. Rev. Lett. **50**, 2039 (1983).
95. J.R. Bergervoet, P.C. van Campen, W.A. van der Sanden, J.J. de Swart, Phys. Rev. C **38**, 15 (1988).
96. V.G.J. Stoks, J.J. De Swart, Phys. Rev. C **42**, 1235 (1990).
97. P. La France, P. Winternitz, J. Phys. (Paris) **41**, 1391 (1980).
98. L. Durand, Phys. Rev. **108**, 1597 (1957).
99. C.M. Vincent, S.C. Phatak, Phys. Rev. C **10**, 391 (1974).
100. V. Baru, C. Hanhart, M. Hoferichter, B. Kubis, A. Nogga, D.R. Phillips, Phys. Lett. B **694**, 473 (2011).
101. V. Baru, C. Hanhart, M. Hoferichter, B. Kubis, A. Nogga, D.R. Phillips, Nucl. Phys. A **872**, 69 (2011).
102. P. Buettiker, U.-G. Meißner, Nucl. Phys. A **668**, 97 (2000).
103. N. Fettes, U.-G. Meißner, S. Steininger, Nucl. Phys. A **640**, 199 (1998).
104. R. Koch, Nucl. Phys. A **448**, 707 (1986).
105. V. Bernard, N. Kaiser, U.-G. Meißner, Int. J. Mod. Phys. E **4**, 193 (1995).
106. V. Bernard, Prog. Part. Nucl. Phys. **60**, 82 (2008).
107. M. Hoferichter, J. Ruiz de Elvira, B. Kubis, U.-G. Meißner, Phys. Rep. **625**, 1 (2016).
108. F. Gross, A. Stadler, private communication (based on data originally supplied by R. Arndt for use with the SAID program).
109. R. Navarro Perez, J.E. Amaro, E. Ruiz Arriola, Phys. Rev. C **88**, 064002 (2013) **91**, 029901(E) (2015).
110. B.H. Daub, V. Henzl, M.A. Kovash, J.L. Matthews, Z.W. Miller, K. Shoniyozov, H. Yang, Phys. Rev. C **87**, 014005 (2013).
111. June L. Matthews, private communication.
112. R. Navarro Perez, J.E. Amaro, E. Ruiz Arriola, Phys. Rev. C **89**, 064006 (2014).
113. F. Gross, A. Stadler, Phys. Rev. C **82**, 034004 (2010).
114. R. Navarro Perez, J.E. Amaro, E. Ruiz Arriola, Phys. Rev. C **88**, 024002 (2013) **88**, 069902(E) (2013).
115. R. Machleidt, Phys. Rev. C **63**, 024001 (2001).
116. A. Ahmidouch *et al.*, Eur. Phys. J. C **2**, 627 (1998).
117. J. Arnold *et al.*, Eur. Phys. J. C **17**, 67 (2000).
118. J. Arnold *et al.*, Eur. Phys. J. C **17**, 83 (2000).
119. C. van der Leun, C. Alderliesten, Nucl. Phys. A **380**, 261 (1982).
120. K. Schoen *et al.*, Phys. Rev. C **67**, 044005 (2003).
121. A. Wächter, L.T. Biegler, Math. Program. **106**, 25 (2006).
122. R.A. Arndt, I.I. Strakovsky, R.L. Workman, Phys. Rev. C **50**, 2731 (1994) SAID partial wave analysis online service, <http://gwdac.phys.gwu.edu/>.
123. R.L. Workman, W.J. Briscoe, I.I. Strakovsky, Phys. Rev. C **94**, 065203 (2016).
124. R.J. Furnstahl, N. Klco, D.R. Phillips, S. Wesolowski, Phys. Rev. C **92**, 024005 (2015).
125. M.C.M. Rentmeester, R.G.E. Timmermans, J.L. Friar, J.J. de Swart, Phys. Rev. Lett. **82**, 4992 (1999).
126. M.C. Birse, J.A. McGovern, Phys. Rev. C **70**, 054002 (2004).
127. G.F. Cox, G.H. Eaton, C.P. Van Zyl, O.N. Jarvis, B. Rose, Nucl. Phys. B **4**, 353 (1968).
128. A. Ekström *et al.*, Phys. Rev. Lett. **110**, 192502 (2013).
129. R.T. Birge, Phys. Rev. **40**, 207 (1932).
130. B.D. Carlsson, Phys. Rev. C **95**, 034002 (2017).
131. J.A. Melendez, S. Wesolowski, R.J. Furnstahl, Phys. Rev. C **96**, 024003 (2017).
132. E. Epelbaum, PoS **CD15**, 014 (2016).
133. V.G.J. Stoks, R.A.M. Klomp, C.P.F. Terheggen, J.J. de Swart, Phys. Rev. C **49**, 2950 (1994).
134. P.W. Lisowski, R.E. Shamu, G.F. Auchampaugh, N.S.P. King, M.S. Moore, G.L. Morgan, T.S. Singleton, Phys. Rev. Lett. **49**, 255 (1982).
135. W.P. Abfalterer, F.B. Bateman, F.S. Dietrich, R.W. Finlay, R.C. Haight, G.L. Morgan, Phys. Rev. C **63**, 044608 (2001).
136. O. Dumbrajs, R. Koch, H. Pilkuhn, G.C. Oades, H. Behrens, J.J. De Swart, P. Kroll, Nucl. Phys. B **216**, 277 (1983).
137. J.J. de Swart, C.P.F. Terheggen, V.G.J. Stoks, arXiv:nucl-th/9509032.
138. H. van Haeringen, L.P. Kok, Phys. Rev. A **26**, 1218 (1982).
139. V.A. Babenko, N.M. Petrov, Phys. At. Nucl. **70**, 669 (2007).
140. T.E.O. Ericson, M. Rosa-Clot, Nucl. Phys. A **405**, 497 (1983).
141. N.L. Rodning, L.D. Knutson, Phys. Rev. C **41**, 898 (1990).
142. A. Huber, T. Udem, B. Gross, J. Reichert, M. Kourogi, K. Pachucki, M. Weitz, T.W. Hansch, Phys. Rev. Lett. **80**, 468 (1998).
143. D.M. Bishop, L.M. Cheung, Phys. Rev. A **20**, 381 (1979).
144. J.L. Friar, J. Martorell, D.W.L. Sprung, Phys. Rev. A **56**, 4579 (1997).
145. D.R. Phillips, J. Phys. G **34**, 365 (2007).
146. F. Gross, A. Stadler, Phys. Rev. C **78**, 014005 (2008).
147. R. Navarro Perez, J.E. Amaro, E. Ruiz Arriola, Phys. Rev. C **89**, 024004 (2014).
148. W. Polyzou, W. Glöckle, Few Body Phys. **9**, 97 (1990).
149. S. Veerasamy, W.N. Polyzou, Phys. Rev. C **84**, 034003 (2011).